



THE UNIVERSITY OF LEEDS

School of Physics and Astronomy

PH.D. THESIS

Construction, Theory and Simulation of Cavity QED Systems

Mark Stanley Everitt

September 2009

Submitted in accordance with the requirements for the degree of Doctor of Philosophy.

The candidate confirms that the work submitted is his own, except where work which has formed part of jointly-authored publications has been included. The candidate confirms that appropriate credit has been given within the thesis where reference has been made to the work of others.

This copy has been supplied on the understanding that it is copyright material and that no quotation from the thesis may be published without proper acknowledgement.

In loving memory of Sid, Edward, Cefur and Fluffy.

Acknowledgements

This research has been carried out by a team which has included Prof. Benjamin Varcoe, Martin Jones, Gary Wilkes, Bruno Sanguinetti, Hawri Majeed, Nicolas Lewty and Dr. Barry Garraway. My contribution in the laboratory was the routing of high voltage, low voltage and microwave cables within the cryostat, mounts for components in the cryostat and constructing cavity testing experiments. The theoretical research presented in this thesis is my own.

First of all, thanks to my supervisor Ben Varcoe for offering me this studentship. Thanks to Martin Jones and Melody Blackman, who gave me a place to stay when I was in need, for their friendship and many interesting chats in the lab and the office. Thanks to Matthew Hill and Sarah Robinson for putting up with me for so many years! Thanks to everyone else in the lab, past and present; Gary Wilkes, Joseph Cotter, Bruno Sanguinetti, Hawri Majeed, Nick Lewty, Luke Johnson and many project students. Thanks for all of the emotional support from all of my friends in Brighton, Leeds and elsewhere, especially Madeline Kruger, Michael Macedo, Matthew Philips, Alison Pellatt, Marc Churchill, Nicola Roberts and Simon Dickie. Thanks to Mum and Allen for their support and helping me move so often. Thanks to Dad, Sam and Charlotte for not minding when I'm too busy to get in contact as often as I should. Thanks to Barry Garraway for his support and helping to keep our collaboration going. A special thanks to Viv Kendon for keeping my work on track, convincing me not to quit and putting me in contact with the right people, which ultimately led to my first postdoctoral fellowship. Thank you to Katherine Brown for the good times. Finally, thank you to all those people who I may have missed out!

Abstract

Mark Stanley Everitt, “Construction, Theory and Simulation of Cavity QED Systems”, Ph.D. thesis, University of Leeds, September 2009.

The microscopically pumped maser, or micromaser is a cavity QED experiment intended to be a physical realisation of the Jaynes-Cummings model of a single two-level atom interacting with a single mode electromagnetic field. This is the simplest model that describes the interaction between light and matter, yet it predicts behaviour unexpected from semiclassical models, such as the revival of Rabi oscillations of an atom interacting with an initially coherent field and non-monotonic linewidth as a function of pumping.

The micromaser at the University of Leeds consists of a high quality superconducting microwave cavity designed to be resonant with the transition between two specific Rydberg states of rubidium. These two states behave like an ideal two level atom, and couple strongly to the cavity field due to a large dipole moment. These Rydberg atoms are passed through the cavity in a rarified beam such that in most instances when there is an atom in the cavity, there will only be one, closely approximating the Jaynes-Cummings model. I present experimental work on the build phase of the micromaser. Specifically I routed all of the wiring and microwave lines in the cryostat that contains the micromaser, and designed mounts for various components. I also designed several testing methods for probing high quality microwave cavity resonances and quality factors which are presented.

Using the Jaynes-Cummings model as a prototype, I demonstrate how extensions to the model can be used to construct universal quantum logic gates that operate on photonic qubits in a multi-mode cavity. This could be realised in a micromaser with a multi-mode cavity. Conversely, I demonstrate that by using atoms as qubits, detuned cavities can be used to generate entangled resources such as the Greenberger-Horne-Zeilinger state, the W state, and graph states of atoms. I show that single qubit rotations on Rydberg atom qubits have already been experimentally demonstrated so that in combination these entangled resources are useful for quantum metrology, quantum computation and even tests of quantum gravity.

Contents

Acknowledgements	iii
Abstract	iv
Introduction	2
I Background	4
1 Micromaser Theory	5
1.1 The Jaynes-Cummings Model	5
1.1.1 The Atom	6
1.1.2 The Electromagnetic Field	6
1.1.3 The Electric Dipole Hamiltonian	7
1.1.4 The Jaynes-Cummings Hamiltonian	7
1.1.5 The Jaynes-Cummings Model	9
1.2 The Master Equation	11
1.2.1 The Liouville Superoperator	13
1.3 Steady States of the Field	15
1.3.1 The Unpumped State	15
1.3.2 The Steady State	17
1.4 Phase Diffusion and Linewidth	18
1.4.1 Measuring Phase Diffusion	20
1.5 Summary	22
II Theory	24
2 Multi-mode Quantum Optical Logic	25

2.1	Theory of Effective Hamiltonians	26
2.2	Single Qubit Rotations	28
2.2.1	Rotations about the z -axis	28
2.2.2	Rotations about the x -axis	29
2.3	Entangling Multi-Qubit Gates	35
2.3.1	The Fredkin Gate	35
2.3.2	Controlled Phase Gate	43
2.4	Implementation	46
2.4.1	Atoms on Demand	46
2.4.2	Cavities	47
2.5	Summary	47
3	Atom-Atom Entanglement	48
3.1	Controlled Phase Gates for Atoms	49
3.1.1	The Tavis-Cummings Hamiltonian	49
3.2	Making Greenberger-Horne-Zeilinger States	53
3.3	Making W States	54
3.4	Graph State Quantum Computation	57
3.4.1	Graph States	57
3.4.2	Rotations on the Bloch Sphere for Atomic Qubits	58
3.5	Probing Quantum Gravity	61
3.5.1	Quantum Gravity and Conformal Fluctuations	62
3.5.2	The Background Parameter	63
3.5.3	GHZ Measurements of Dephasing	64
3.5.4	Augmented Tests with GHZ States	65
3.5.5	Discussion	66
3.5.6	Alternatives	66
III	Experiment	68
4	Experimental Set Up	69
4.1	The Cryostat	69
4.2	Rydberg Atoms	71
4.2.1	Rubidium Dispensers	72
4.2.2	Exciting Rubidium up to Rydberg states	73
4.3	Microwave Transmission	74
4.3.1	Coaxial Cable	74

4.3.2	Goubau Lines	75
4.4	High Quality Microwave Resonators	76
4.4.1	Geometry	76
4.4.2	Material	77
4.4.3	Mount and Cables	78
4.5	State-selective Detection	79
4.6	The Experimental Region	81
4.7	Software	82
5	Microwave Cavity Resonance Scans	86
5.1	Quality Factor	86
5.2	Transmission or Reflection?	87
5.3	Simple scans with a Schottky diode	88
5.4	Simple scans using a power meter	89
5.5	Ring-Down Spectroscopy	90
5.6	Using a Lock-In Amplifier for High Quality Resonators	93
5.6.1	Discussion	96
5.7	Using a Lock-In Amplifier with Ring-Down Measurements.	97
5.8	Summary	98
Conclusion		101
IV	Appendix	103
A	Extended Derivations	104
A.1	Zheng and Guo's Controlled Phase Gate	104
B	Code	106
B.1	Log File Converter	106
B.2	Power Meter Cavity Resonance Sweep	107
C	Revised Cryostat Operation	109
C.1	Preparation	109
C.2	Pulse Tube Cooling	110
C.3	Pre-cooling	110
C.4	Mixing Cycle	111
C.5	Stopping the Cryostat	112

C.6 Cleaning the Helium Lines	113
D Performing Transformations	114
D.1 Derivation	114
D.2 A Simple Example	116
Bibliography	118

List of Figures

1.1	A two level atom in a single mode field.	9
1.2	Detuning affects rabi frequency.	11
1.3	Detuning affects transition probability.	12
1.4	Conceptual Micromaser	13
1.5	Plot of a thermal field.	17
1.6	Plot of three steady states of the field.	18
1.7	The pump parameter affects photon number distribution at 30 mK.	19
1.8	The pump parameter affects photon number distribution at 500 mK.	20
1.9	Q plots of a phase diffusion experiment.	22
1.10	Conceptual phase sensitive micromaser.	23
2.1	z -axis rotations.	28
2.2	x -rotation of a photonic qubit.	29
2.3	Alternative diagram for the x -rotation of a photonic qubit.	31
2.4	Numerical and Effective Hamiltonian solutions for an x -rotation gate.	34
2.5	Conditioned and Unconditioned fidelity of the x -rotation gate.	35
2.6	Level diagram for the Fredkin Gate.	36
2.7	Fidelity and gate-time for the effective three state Fredkin gate.	44
2.8	Controlled Phase gate with a ladder of states	45
3.1	Level diagram for atom-atom interactions.	50
3.2	The collisional phase gate	53
3.3	Apparatus for building EPR states of atoms.	54
3.4	Graph representation of an $N = 6$ GHZ state.	55
3.5	Apparatus for building $N = 5$ GHZ states of atoms.	56
3.6	Quantum circuit to build a five atom GHZ state	57
3.7	Graphical representation of the hexagonal lattice graph state	58
3.8	Apparatus for constructing hexagonal graph states.	59

3.9	Apparatus for constructing cluster states.	60
4.1	Simplified cryostat cross-section.	70
4.2	Cryostat cool-down plotted on a log temperature scale.	71
4.3	Rubidium dispenser.	73
4.4	The candlestick oven.	74
4.5	Astro-Cobra-Flex cable for microwave transmission.	75
4.6	Goubau Line.	76
4.7	Photographs of cavities.	77
4.8	Cavity Mount and Squeezer	79
4.9	Wiring between the 77 K and 4 K stages.	80
4.10	Interior of the detector box.	81
4.11	Experiment Cross-Section	82
4.12	A view of the core of the micromaser.	83
4.13	The cryostat and support equipment.	84
4.14	The cryostat.	85
5.1	Simple cavity resonance sweep.	89
5.2	Low Q copper cavity resonances found using a Schottky diode.	90
5.3	Aluminium cavity resonances found using a Schottky diode.	91
5.4	Aluminium cavity resonances found using a power meter.	92
5.5	Aluminium cavity ring-down measurement.	93
5.6	Two modes ringing down at differing frequencies produce a beat.	94
5.7	Frequency of modulation affects the locking signal.	95
5.8	Lock-in amplifier enhanced scan of an aluminium cavity.	96
5.9	Lock-in amplifier enhanced scan of an aluminium cavity using second harmonic.	97
5.10	Lock-in amplifier enhanced ring-down scan of an aluminium cavity.	98
B.1	Sample LabVIEW code for detecting cavity resonances using a lock-in amplifier.	108

List of Tables

2.1	A qubit embedded in two cavity field modes.	25
2.2	A qudit embedded in two cavity field modes.	26
2.3	Truth table for the Fredkin gate.	36
2.4	Encoding of three qubits	38
2.5	The states of the Fredkin system initially in state $ 1, 0, 1\rangle a\rangle$	39
2.6	The states accessible to the effective three-state Fredkin gate	41
2.7	Truth table for the Controlled Phase gate.	43
3.1	The collisional phase gate.	52

Acronyms

- Q* quality factor.
- CEM channel electron multiplier.
- EPR Einstein-Podolsky-Rosen.
- GHZ Greenberger-Horne-Zeilinger.
- GPIB general purpose interface bus.
- JCM Jaynes-Cummings model.
- PTFE polytetrafluoroethylene.
- QED quantum electrodynamics.
- TE transverse electric.
- TM transverse magnetic.
- USB universal serial bus.

Introduction

Introduction

In 1963 Edwin Jaynes and Frederick Cummings wrote a paper titled *Comparison of Quantum and Semiclassical Radiation Theory with Application to the Beam Maser* [1]. This paper contained what became known as the Jaynes-Cummings model (JCM) of a single two level atom in a single mode (frequency) field [2]. The model used this idealised atom and field to construct an exactly solvable evolution of the joint atom-field system, and hence model a beam maser in a fully quantum mechanical framework. This JCM largely inherited from the Dicke model, a predecessor that modelled the collective effects of a gas of atoms in a field [3]. A successor to the JCM, the Tavis-Cummings model, generalised the JCM to many atoms, refining the Dicke model [4].

The micromaser, a portmanteau of the first and last words of the phrase *microscopically pumped maser*, also known as the one-atom maser, is an experimental attempt to construct a maser which is as closely modelled as possible by the JCM. A micromaser is thus a testbed for the predictions made by the JCM [5]. Example predictions are vacuum Rabi oscillations [6], the Purcell effect [7] and the revival of Rabi oscillations of an atom in a field initially in a coherent state [8]. Beyond the Jaynes-Cummings model, predictions made by a master equation with the Jaynes-Cummings Hamiltonian as a component can be compared with a laboratory micromaser to test our understanding of dissipative systems and decoherence as well as maser linewidth [9–18].

Laboratory micromasers have been used to observe entanglement between atoms leaving a cavity [19], and number states of the cavity field [20–26]. Micromaser technology can be adapted to manufacture large entangled resources for quantum metrology, tests of non-locality and quantum gravity, and quantum computation [27–57], which has been the focus of my research.

Practical advancements made by the micromaser at the University of Leeds include a novel approach to producing Rydberg states of $^{85}_{37}\text{Rb}$ [58–61] using a three step infrared laser excitation system locked to vapour cells [62, 63], oven design refinements for producing atomic beams [64] and squeezing cavities in cryogenic conditions [62, 63, 65]. Current research in the laboratory is concentrated on microwave transmission within a cryostat [66–69], the construction and characterisation of superconducting microwave resonators [70–74] and the enhancement of state-selective field ionisation detectors for determining the state of a Rydberg atom [75].

This thesis covers a range of topics with the micromaser in common. My mandate was to assist

INTRODUCTION

in building the new micromaser system, and to study the micromaser as a source of entangled atoms. In the laboratory my responsibilities were to select and route the wiring for components in the cryostat, route microwave lines in the cryostat and tend to vacuum systems in general. I was also responsible for running the cryostat, most of the programming and developing cavity testing experiments. Outside the laboratory I worked on the micromaser and related technology for entangling Rydberg atoms, quantum computation and even in experimental tests of quantum gravity.

This thesis is split into three parts. Part I, Background, contains background micromaser theory. It is intended as a foundation for new graduate students and to unify the notation and conventions used in micromaser literature. Parts II and III are on theory and experimental work that I have done. These two parts form the majority of this thesis, and contain my own work. All material is my own unless otherwise stated.

Chapter 2 explores an option for performing universal quantum logic using multi-mode fields [76] and multi-level atoms [28]. The aim of this was to encode qubits on pairs of field modes and use the interaction with an atom to shuffle photons around between modes, whilst returning the atom to its original state to avoid loss of quantum information. This is being considered for publication in a paper written in collaboration with Dr. Barry Garraway at the University of Sussex.

Chapter 3 begins with a controlled phase gate for atoms in crossed atomic beams. I based my work in this chapter on a controlled phase gate that uses two atoms interacting with a detuned field [35]. I show how to produce N -atom Greenberger-Horne-Zeilinger (GHZ) states of atoms using these controlled phase gates, and more complex graph states. I also show how to produce W states [77] using a generalised form of the controlled phase gate, and that it can produce up to four atom W states. I produced a paper on detecting the decoherence due to quantum gravity of entangled states, and this work is presented in this chapter.

Chapter 4 has some details on the components of the micromaser experiment at Leeds University. For completeness I include a little detail on all parts of the experiment. My contribution was the majority of the mounting assembly in the cryostat, cables to send and return microwaves from the cryostat and wiring for the detector box and cavity squeezer. Most of the purpose coded software used by the experiment was written by me.

Chapter 5 presents my work on a variety of tests I produced to measure the resonant frequencies and quality factor of pillbox electromagnetic cavities. These tests were designed to be portable and simple to use with software I coded to automate the bulk of the task. The testing equipment can be transported to a chemistry lab and a non-specialist can test a cavity between etches to see if the resonance is correct. The equipment is also suitable for testing a cavity in the cryostat.

Part I

Background

Chapter 1

Micromaser Theory

... we never experiment with just one electron or atom or (small) molecule. In thought-experiments we sometimes assume that we do; this invariably entails ridiculous consequences...

Are There Quantum Jumps? Part II [78]
Erwin Schrödinger

This chapter was written to serve as a foundation for the formalism used in later chapters, and I hope that it is a useful text for my successors when they start learning the theory behind the micromaser. There is a large leap from undergraduate quantum mechanics to an understanding of micromaser theory, and there are a few conventions by different key researchers that clash and lead to confusion. There is considerable freedom to choose interaction pictures, which are of course completely correct provided that one is consistent. The notation is also ambiguous in the literature. For example, the “Rabi frequency” is used to mean the frequency of the oscillations of population inversion, and the oscillations in probability amplitude. For the sake of simplicity I define things in this chapter, and avoid ambiguous terms when possible. To clear up the issue of Rabi frequency I refer to a term g as simply a dipole coupling constant whenever possible. This chapter culminates in the theory behind micromaser phase diffusion, which is the process our micromaser is designed to test.

1.1 The Jaynes-Cummings Model

The micromaser is designed to be the closest possible approximation to the JCM. The JCM deals with the evolution of a system consisting of a single two state atom in a single mode field in a fully quantum mechanical way [1]. A recent summary of the JCM may be found in the review article by Shore and Knight [2].

1.1.1 The Atom

The atom considered is idealised as a two state system, ground $|g\rangle$ and excited $|e\rangle$. To model its interaction with a field, we first need the dipole operator

$$\hat{\mu} = \mu^* \hat{\sigma}^+ + \mu \hat{\sigma}^- , \quad (1.1)$$

where $\hat{\sigma}^+ = |e\rangle \langle g|$ and $\hat{\sigma}^- = |g\rangle \langle e|$. This simply moves $|g\rangle$ to $|e\rangle$ and vice versa. This requires a parity change, as implied by the name of the operator. The Hamiltonian for a free atom is

$$H_{\text{atom}} = \frac{\hbar\omega_a}{2} \hat{\sigma}_3 , \quad (1.2)$$

where $\hbar\omega_a$ is the transition energy of the atom from state $|g\rangle$ to state $|e\rangle$. The energy is referenced from half way between the levels and $\hat{\sigma}_3 = |e\rangle \langle e| - |g\rangle \langle g|$.

A two state atom may seem like an absurdity, but with a careful choice of atomic levels so that there is a single pair of states with an energy gap close to resonance with the single-mode field then other transitions are suppressed. This is simply a statement of the Purcell effect [7].

1.1.2 The Electromagnetic Field

A field can be decomposed into superposition of modes of different frequencies. In a cavity, we assume that only a single mode is present, and all others destructively interfere. A mode of the field is a quantum harmonic oscillator, and so the creation and annihilation (ladder) operators apply.

$$\begin{aligned} \hat{a} |n\rangle &= \sqrt{n} |n-1\rangle \\ \hat{a}^\dagger |n\rangle &= \sqrt{n+1} |n+1\rangle \\ \hat{a}^\dagger \hat{a} |n\rangle &= \hat{N} |n\rangle = n |n\rangle \\ [\hat{a}, \hat{a}^\dagger] &= \mathbb{1} , \end{aligned} \quad (1.3)$$

where n is the number of photons present in the mode. The free Hamiltonian for a mode of the electromagnetic field is

$$H_{\text{field}} = \hbar\omega \left(\hat{a}^\dagger \hat{a} + \frac{1}{2} \right) . \quad (1.4)$$

Using the Heisenberg equation of motion

$$\frac{d}{dt} \hat{A}(t) = \frac{i}{\hbar} [H, \hat{A}(t)] + \frac{\partial}{\partial t} \hat{A}(t) , \quad (1.5)$$

where \hat{A} is an arbitrary operator, the solutions for the time dependent creation and annihilation operators in the Heisenberg picture are

$$\begin{aligned}\hat{a}(t) &= \hat{a}e^{-i\omega t} \\ \hat{a}^\dagger(t) &= \hat{a}^\dagger e^{i\omega t}.\end{aligned}\tag{1.6}$$

The electric field operator at position \mathbf{r} for a plane wave mode in a mode volume V with wavevector \mathbf{k} and frequency ω and with linear polarization ϵ is

$$\hat{\mathbf{E}}(\mathbf{r}, t) = i \left(\frac{\hbar\omega}{2\epsilon_0 V} \right)^{\frac{1}{2}} \epsilon \left[\hat{a}e^{-i\omega t + i\mathbf{k} \cdot \mathbf{r}} - \hat{a}^\dagger e^{i\omega t - i\mathbf{k} \cdot \mathbf{r}} \right].\tag{1.7}$$

The single mode assumption requires that the micromaser must use a cavity with a very high *quality factor*, or Q . This high quality factor reduces the linewidth of the cavity so that for an extremely good microwave cavity the linewidth may be as small as 1 Hz at a resonant frequency of 21 GHz.

1.1.3 The Electric Dipole Hamiltonian

The electric dipole Hamiltonian describes an atom in an electromagnetic field,

$$H = \frac{\hbar\omega_a}{2} \hat{\sigma}_3 - \hat{\mu} \cdot \hat{\mathbf{E}}(\mathbf{r}, t).\tag{1.8}$$

If the dipole moment is much smaller than the wavelength of the mode of the field, then the dipole approximation can be made and spatial dependence can be dropped,

$$H = \frac{\hbar\omega_a}{2} \hat{\sigma}_3 - \hat{\mu} \cdot \hat{\mathbf{E}}(t).\tag{1.9}$$

1.1.4 The Jaynes-Cummings Hamiltonian

If $\hat{\mathbf{E}}$ from Equation (1.9) is substituted with the electric field operator in the dipole approximation, then the fully quantum mechanical atom-light Hamiltonian is

$$H_{\text{atom-light}} = \frac{\hbar\omega_a}{2} \hat{\sigma}_3 - i\hbar g \left(\hat{a}e^{-i\omega t} - \hat{a}^\dagger e^{i\omega t} \right) (\hat{\sigma}^+ + \hat{\sigma}^-),\tag{1.10}$$

where $g = \mu \cdot \epsilon \left(\frac{\omega}{2\hbar\epsilon_0 V} \right)^{\frac{1}{2}}$ can be interpreted later as a coupling constant and μ is assumed to be real without loss of generality. Transforming into the Schrödinger picture, the Hamiltonian becomes

$$H_{\text{atom-light}} = \underbrace{\frac{\hbar\omega_a}{2}\hat{\sigma}_3}_{\text{atom}} + \underbrace{\hbar\omega \left(\hat{a}^\dagger \hat{a} + \frac{1}{2} \right)}_{\text{field}} - i\hbar g \left(\hat{a} - \hat{a}^\dagger \right) \left(\hat{\sigma}^+ + \hat{\sigma}^- \right), \quad (1.11)$$

recovering the free field term. The vacuum term in the free field part that has emerged can be neglected as a global phase. Expanding out the interaction term yields four new terms:

- $\hat{a}\hat{\sigma}^+$ The atom absorbs a photon from the field.
- $\hat{a}^\dagger\hat{\sigma}^-$ The atom loses its excitation to the field.
- $\hat{a}\hat{\sigma}^-$ The atom decays and the field loses a photon.
- $\hat{a}^\dagger\hat{\sigma}^+$ The atom becomes excited and the field gains a photon.

The second two terms are not energy conserving and are thus heavily suppressed. A more mathematically complete explanation takes us via another transformation into an interaction picture with a time-dependent Hamiltonian.

$$H_I = \frac{\hbar\Delta}{2}\hat{\sigma}_3 - i\hbar g \left(\hat{\sigma}^+ e^{i\omega t} + \hat{\sigma}^- e^{-i\omega t} \right) \left(\hat{a} e^{-i\omega t} - \hat{a}^\dagger e^{i\omega t} \right) \quad (1.12)$$

This transformation is shown in Appendix D as a demonstration. Expanding the brackets, two terms have no time dependence and two do. The latter are considered to be fast rotating and are substituted for zero. This is called the rotating wave approximation [5]. Finally we have the Jaynes-Cummings Hamiltonian

$$H_{JC} = \frac{\hbar\Delta}{2}\hat{\sigma}_3 - i\hbar g \left(\hat{\sigma}^+ \hat{a} - \hat{\sigma}^- \hat{a}^\dagger \right), \quad (1.13)$$

where Δ is the detuning between the energy of a photon in the mode and the transition energy of the atom, $\Delta = \omega_a - \omega$. This is useful for showing the dependence of the dynamics of the interaction on detuning, but not as instructive for showing how photon number affects the dynamics. The reverse transformation back to the frame of (1.11) and disregarding a vacuum field term (which only contributes a global phase) gives

$$H_{JC} = \underbrace{\frac{\hbar\omega_a}{2}\hat{\sigma}_3}_{\text{atom}} + \underbrace{\hbar\omega \hat{a}^\dagger \hat{a}}_{\text{field}} - i\hbar g \left(\hat{\sigma}^+ \hat{a} - \hat{\sigma}^- \hat{a}^\dagger \right). \quad (1.14)$$

Strangely, a version of the Hamiltonian that I think is more intuitive has been rarely (if ever) noted. Another transformation can give the following alternative Hamiltonian

$$H_{JC} = -\hbar\Delta \hat{a}^\dagger \hat{a} - i\hbar g \left(\hat{\sigma}^+ \hat{a} - \hat{\sigma}^- \hat{a}^\dagger \right). \quad (1.15)$$

This version does not track the energy dependent rotation of the field as (1.14) does. This may be particularly useful when considering a system with multiple interactions with the field where phase may be interesting. I make extensive use of this form in Chapter 2. I conclude that the reason that this form of the Hamiltonian is not seen is that its analytic solution is more difficult to derive.

1.1.5 The Jaynes-Cummings Model



Figure 1.1: The JCM can be visualised with this energy level diagram. The difference between the transition energy between the two atomic states and the frequency of the field is the detuning Δ . By convention in this thesis $\omega + \Delta = \omega_a$.

The Hamiltonian in Equation (1.13) conserves energy¹, i.e. $\hat{a}^\dagger \hat{a} + \hat{\sigma}^+ \hat{\sigma}^-$ commutes with H_{JC} . This means that for an atom and field initialized to particular states, only one other state of the system is accessible, corresponding to an excitation (decay) of the atom and the loss (gain) of a photon.

$$\begin{aligned} |e\rangle|n\rangle &\leftrightarrow |g\rangle|n+1\rangle \\ |g\rangle|n\rangle &\leftrightarrow |e\rangle|n-1\rangle \end{aligned} \tag{1.16}$$

From this point I will refer to the state of the system in the composite form $|\text{atom}\rangle|\text{field}\rangle = |\text{atom, field}\rangle$ so

$$\begin{aligned} |e,n\rangle &\leftrightarrow |g,n+1\rangle \\ |g,n\rangle &\leftrightarrow |e,n-1\rangle . \end{aligned} \tag{1.17}$$

This highlights the entanglement produced between the atom and the field during interaction. The JCM is analytically soluble, allowing for intricate study of its dynamics. Solving the Schrödinger equation in the form

$$\frac{d}{dt}|\Psi\rangle = -\frac{iH}{\hbar}|\Psi\rangle , \tag{1.18}$$

is as simple as solving a second order ordinary differential equation with constant coefficients. If

¹As do those in Equation (1.14) and Equation (1.15) since these are the Hamiltonian in Equation (1.13) after unitary transformations.

the initial state of the system is

$$|\Psi_0\rangle = \alpha_0 |e, n\rangle + \beta_0 |g, n+1\rangle , \quad (1.19)$$

then the state of the system after interaction time t is

$$\begin{aligned} \alpha(t) &= \left[\alpha_0 \cos\left(\frac{\Omega t}{2}\right) - \frac{i\alpha_0\Delta + 2\beta_0 g\sqrt{n+1}}{\Omega} \sin\left(\frac{\Omega t}{2}\right) \right] \\ \beta(t) &= \left[\beta_0 \cos\left(\frac{\Omega t}{2}\right) + \frac{i\beta_0\Delta + 2\alpha_0 g\sqrt{n+1}}{\Omega} \sin\left(\frac{\Omega t}{2}\right) \right]. \end{aligned} \quad (1.20)$$

Ω is called the Rabi frequency, and is a function of the number of photons in the field mode,

$$\Omega = \sqrt{\Delta^2 + 4g^2(n+1)}. \quad (1.21)$$

Some important behaviour can be derived from Equation (1.20) and Equation (1.21). If the field is in a number state (also known as a Fock state) then an excited atom will oscillate between the ground and excited levels, and a corresponding photon is created and annihilated in the field, preserving energy. Even if the field is in the vacuum state these oscillations are still expected. This particular phenomenon is referred to as *vacuum Rabi oscillations* [6]. If the system is resonant, then the probability of finding the atom in the ground or excited state oscillates between zero and one. If the field is detuned, then the probability of finding that an atom that was initially in the excited state has decayed never reaches one. Equation 1.21 leads to an increase in the oscillations between the states of the system if the detuning is increased. These characteristics are shown in Figure 1.2 for the $n = 10$ Fock state. Figure 1.3 shows that detuning leads to a Lorentzian profile for the maximum transition probability.

When the atomic transition is resonant with the field mode, the interaction reduces to

$$\begin{aligned} \alpha(t) &\mapsto \alpha_0 \cos(gt\sqrt{n+1}) - \beta_0 \sin(gt\sqrt{n+1}) \\ \beta(t) &\mapsto \beta_0 \cos(gt\sqrt{n+1}) + \alpha_0 \sin(gt\sqrt{n+1}). \end{aligned} \quad (1.22)$$

Using these, the evolution operator for resonance can be constructed.

$$\begin{aligned} \hat{U}(t_{\text{int}}) &= \cos\left(gt_{\text{int}}\sqrt{\hat{N}+1}\right) \hat{\sigma}^+ \hat{\sigma}^- + \cos\left(gt_{\text{int}}\sqrt{\hat{N}}\right) \hat{\sigma}^- \hat{\sigma}^+ \\ &- \frac{\sin\left(gt_{\text{int}}\sqrt{\hat{N}+1}\right)}{\sqrt{\hat{N}+1}} \hat{a} \hat{\sigma}^+ + \frac{\sin\left(gt_{\text{int}}\sqrt{\hat{N}}\right)}{\sqrt{\hat{N}}} \hat{a}^\dagger \hat{\sigma}^- \end{aligned} \quad (1.23)$$

These are useful if the atom is incoming in a superposition state and the system can have two possible numbers of excitations, whereas the resonant interaction equations (1.22) describe a system

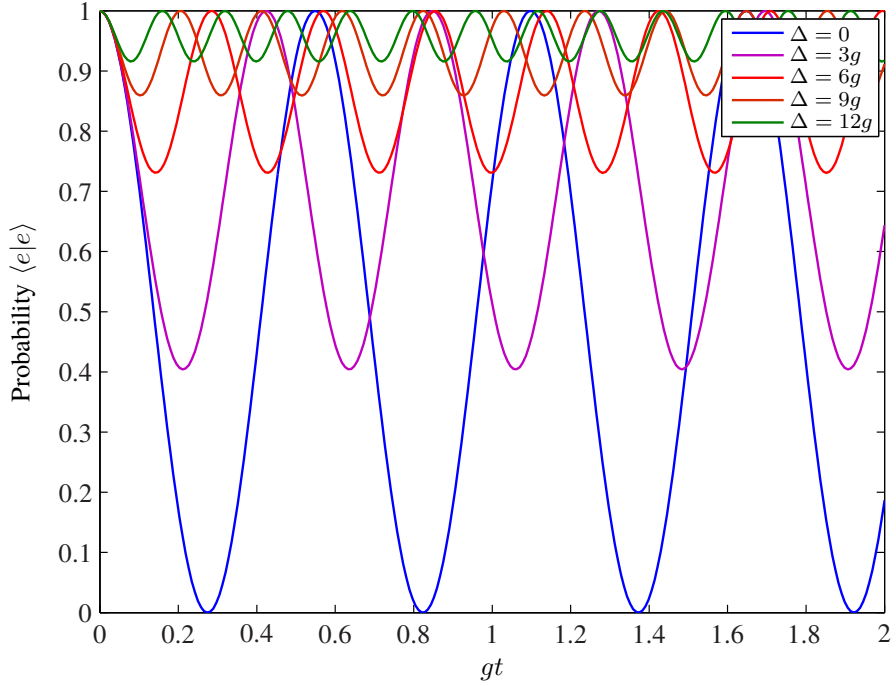


Figure 1.2: As detuning is raised, the probability of measuring the atom in the excited (initial) state has a increasing minimum. As the detuning is increased the frequency of the oscillations in state increases as shown in Equation (1.21). gt is the atom-cavity coupling constant multiplied by the interaction time. In the resonant case g is twice the Rabi frequency Ω . In this plot I have set $n = 10$.

with a single number of excitations.

1.2 The Master Equation

The Jaynes-Cummings model describes the evolution of a system composed of a single two state atom and a single mode field. The micromaser is slightly more complex. The cavity sits at the centre of the experiment, and atoms are sent through in a beam, as shown in Figure 1.4. The beam is Poisson distributed so that when an atom is present in the cavity, only one is present in most events. In fact this is so diffuse that for the majority of the time no atom is present. In addition, no cavity is perfect. Some radiation may leak into or out of the cavity. This arrangement is a type of beam maser, with an extremely high quality factor cavity, and an extremely low pump rate. The intention is to use this limit to see if the Jaynes-Cummings model predicts what we see in masers. This is best modelled by a master equation. A master equation can handle the situation of a quantum harmonic oscillator damped by a thermal bath. This situation may lead to systems that are neither completely quantum mechanical nor classical, leading to the need for the density operator ρ (sometimes called the statistical operator).

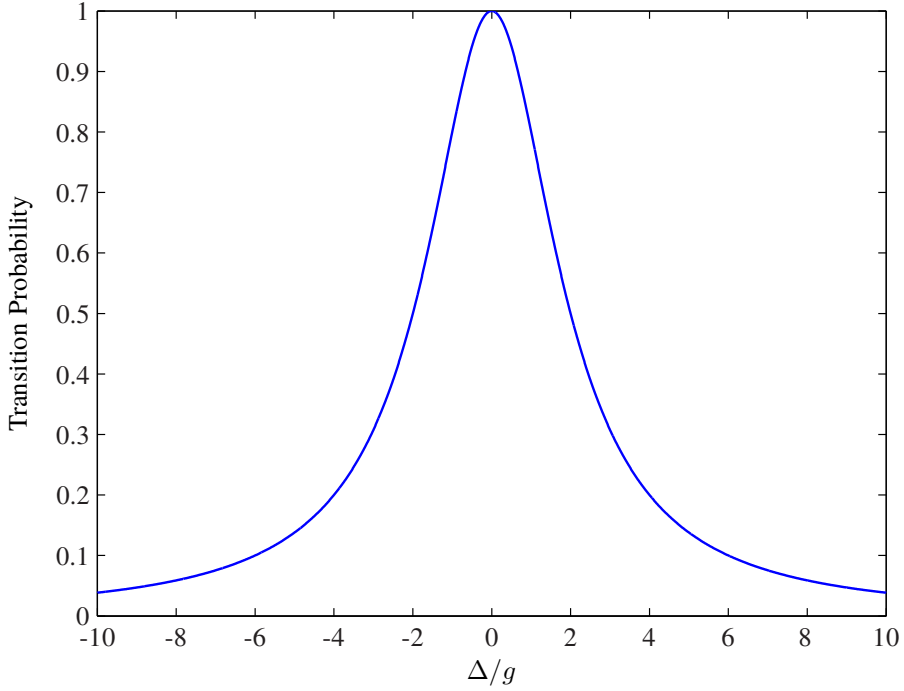


Figure 1.3: As detuning is raised, the maximum probability of transition is reduced. This results in a Lorentzian resonance shape as would be expected. In this plot I set $n = 0$, demonstrating that vacuum Rabi oscillations are responsible for the transition.

The Markovian master equation can be stated as below [9, 10],

$$\dot{\rho}(t) = \hat{\mathcal{L}}[\rho(t)] + R\hat{F}(t_{\text{int}})[\rho(t)], \quad (1.24)$$

where R is the average rate of atomic injection in a particular state, $\hat{\mathcal{L}}$ is the Liouville superoperator for cavity damping (see Section 1.2.1) and \hat{F} is the Jaynes-Cummings superoperator. Using Equation (1.23) the Jaynes-Cummings superoperator is

$$\hat{F}[\rho] = \hat{U}(t_{\text{int}})\rho\hat{U}^\dagger(t_{\text{int}}) - \rho. \quad (1.25)$$

In order to be modelled as a Markovian process the atomic arrivals must be uncorrelated, i.e. the atomic beam must be Poisson distributed. In the general non-Markovian case the last term in Equation (1.24) is more complex, reflecting the non-random arrival statistics. Recent advances in the mathematics of master equations may allow for the analytic handling of non-Markovian master equations describing more general micromasers [11, 12]. We know that the type of rubidium dispenser we use as a source of atoms [79] does not have Poisson statistics, and cannot strictly be modelled as a Markovian process.

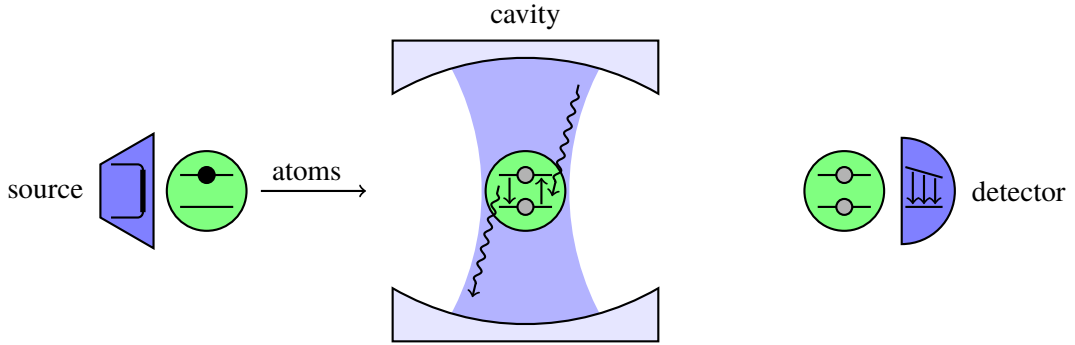


Figure 1.4: The conceptual micromaser. A source provides two state atoms in the excited state. The cavity field is close to resonance with the atomic transition, so that the excitation of the atom can be transferred to the field and back again. A detector detects the atom in the ground or excited state.

1.2.1 The Liouville Superoperator

On its own, the Liouville superoperator describes a system in thermal equilibrium with the environment, and may describe an unpumped micromaser cavity, as shown in Section 1.3. A superoperator is an operator that acts on operators. The simplest way to grasp this is to think about a time evolution operator. When state vectors are used, the evolution of a system goes as

$$|\Psi(t)\rangle = \hat{U} |\Psi_0\rangle . \quad (1.26)$$

Consider the extension of this to the density operator. The density operator of a pure state is just the outer product of that state with itself, so it is simple to see that the density operator will need the evolution operator to act on both sides of a density operator. The same is true of other operators. To apply the creation operator, it must be applied on the left and the annihilation operator on the right of the density operator which can seem counterintuitive.

$$\rho(t) = \hat{U} \rho_0 \hat{U}^\dagger . \quad (1.27)$$

It can be cumbersome writing operators out on both sides of a density operator, and it can even obfuscate a calculation, so it is common to invent a superoperator to replace them. In this case I can define the evolution superoperator \hat{S} , such that

$$\hat{S}[A] = \hat{U} A \hat{U}^\dagger . \quad (1.28)$$

The Liouville superoperator simulates a damped field mode as a field mode with successive weakly coupled atoms interacting with it [13]. In the interaction picture

$$\frac{\partial}{\partial t} \rho_t^{\text{field}} = r_{\text{ex}} \Delta_{\text{ex}} \rho_t^{\text{field}} + r_{\text{gr}} \Delta_{\text{gr}} \rho_t^{\text{field}}, \quad (1.29)$$

where r_{ex} and r_{gr} are the rates of the incoming ground and excited states, and the subscripted t denotes the density operator at some time. For an atom arriving in the excited state the change in the field part of the density operator is:

$$\begin{aligned} \Delta_{\text{ex}} \rho_t^{\text{field}} &= \cos \left(g t_{\text{int}} \sqrt{\hat{N} + 1} \right) \rho_t^{\text{field}} \cos \left(g t_{\text{int}} \sqrt{\hat{N} + 1} \right) \\ &+ \frac{\sin \left(g t_{\text{int}} \sqrt{\hat{N}} \right)}{\sqrt{\hat{N}}} \hat{a}^\dagger \rho_t^{\text{field}} \hat{a} - \frac{\sin \left(g t_{\text{int}} \sqrt{\hat{N}} \right)}{\sqrt{\hat{N}}} - \rho_t^{\text{field}} \end{aligned} \quad (1.30)$$

Assuming that the coupling is very weak, a small angle approximation can be made².

$$\Delta_{\text{ex}} \rho_t^{\text{field}} \approx g^2 t_{\text{int}}^2 \left(\hat{a}^\dagger \rho_t^{\text{field}} \hat{a} - \frac{1}{2} \hat{a} \hat{a}^\dagger \rho_t^{\text{field}} - \frac{1}{2} \rho_t^{\text{field}} \hat{a} \hat{a}^\dagger \right). \quad (1.31)$$

Exactly the same procedure can be applied to an incoming atom in the ground state.

$$\Delta_{\text{gr}} \rho_t^{\text{field}} \approx g^2 t_{\text{int}}^2 \left(\hat{a} \rho_t^{\text{field}} \hat{a}^\dagger - \frac{1}{2} \hat{a}^\dagger \hat{a} \rho_t^{\text{field}} - \frac{1}{2} \rho_t^{\text{field}} \hat{a}^\dagger \hat{a} \right) \quad (1.32)$$

The rate of change of ρ_t^{field} due to damping is now

$$\begin{aligned} \frac{\partial}{\partial t} \rho_t^{\text{field}} &= -r_{\text{ex}} g^2 t_{\text{int}}^2 \left(\frac{1}{2} \hat{a} \hat{a}^\dagger \rho_t^{\text{field}} + \frac{1}{2} \rho_t^{\text{field}} \hat{a} \hat{a}^\dagger - \hat{a}^\dagger \rho_t^{\text{field}} \hat{a} \right) \\ &- r_{\text{gr}} g^2 t_{\text{int}}^2 \left(\frac{1}{2} \hat{a}^\dagger \hat{a} \rho_t^{\text{field}} + \frac{1}{2} \rho_t^{\text{field}} \hat{a}^\dagger \hat{a} - \hat{a} \rho_t^{\text{field}} \hat{a}^\dagger \right). \end{aligned} \quad (1.33)$$

As these weakly coupled atoms are used to simulate the damping of the cavity field, the rates must be related via Maxwell-Boltzmann statistics [13]

$$\frac{r_{\text{ex}}}{r_{\text{gr}}} = \exp \left(-\frac{\hbar \omega}{k_B T} \right) = \frac{\nu}{\nu + 1}, \quad (1.34)$$

where ν is shown in Section 1.3.1 to be the mean thermal photon number. The factor of $g^2 t_{\text{int}}^2$ can be hidden inside a rate parameter A which gives the Liouville superoperator for the interaction

²The first order cosines taken together cancel with ρ . Only one second order cosine term at a time is considered which is valid for the approximation. The sine terms are considered only in the first order.

picture.

$$\begin{aligned}\hat{\mathcal{L}}[\rho] = & -\frac{1}{2}A\nu\left(\hat{a}\hat{a}^\dagger\rho + \rho\hat{a}\hat{a}^\dagger - 2\hat{a}^\dagger\rho\hat{a}\right) \\ & -\frac{1}{2}A(\nu+1)\left(\hat{a}^\dagger\hat{a}\rho + \rho\hat{a}^\dagger\hat{a} - 2\hat{a}\rho\hat{a}^\dagger\right)\end{aligned}\quad (1.35)$$

A is related to cavity quality factor (Q) by

$$A = \frac{\omega}{2\pi Q} \quad (1.36)$$

1.3 Steady States of the Field

1.3.1 The Unpumped State

The Liouville superoperator (1.35) alone is enough to describe an unpumped, high Q cavity in a thermal bath. When the cavity is in the steady state, $\dot{\rho} = \hat{\mathcal{L}}[\rho] = 0$. It is easy to show using cyclic relations of the trace and its linear mapping properties that

$$\frac{d}{dt}\langle\hat{a}^\dagger\rangle_t = \text{Tr}\left(\hat{a}^\dagger\hat{\mathcal{L}}[\rho_t]\right) = -\frac{1}{2}A \cdot \text{Tr}\left(\hat{a}^\dagger\rho_t\right) = -\frac{1}{2}A\langle\hat{a}^\dagger\rangle_t \quad (1.37)$$

and similarly

$$\frac{d}{dt}\langle\hat{a}\rangle_t = -\frac{1}{2}A\langle\hat{a}\rangle_t \quad (1.38a)$$

$$\frac{d}{dt}\langle\hat{N}\rangle_t = -A\left(\langle\hat{N}\rangle_t - \nu\right) \quad (1.38b)$$

The solutions to which are

$$\langle\hat{a}^\dagger\rangle_t = \langle\hat{a}^\dagger\rangle_0 e^{-At/2} \quad (1.39a)$$

$$\langle\hat{a}\rangle_t = \langle\hat{a}\rangle_0 e^{-At/2} \quad (1.39b)$$

$$\langle\hat{N}\rangle_t = \nu + (\langle\hat{N}\rangle_0 - \nu)e^{-At} \quad (1.39c)$$

The constant A is thus a decay constant, as expected. At long times these solutions lead to

$$\langle\hat{a}^\dagger\rangle_{t \rightarrow \infty} \rightarrow 0 \quad (1.40a)$$

$$\langle\hat{a}\rangle_{t \rightarrow \infty} \rightarrow 0 \quad (1.40b)$$

$$\langle\hat{N}\rangle_{t \rightarrow \infty} \rightarrow \nu \quad (1.40c)$$

As the ladder operators have no effect in the long time limit so that the expectation of the number operator reaches a constant, the system reaches a *steady state*. The steady state implies that $\rho_{t \rightarrow \infty}$ commutes with the number operator \hat{N} and therefore can be expressed as a function of \hat{N} [13]. Functions of \hat{N} also have the following property:

$$\hat{a}f_{\hat{a}^\dagger \hat{a}} = f_{\hat{a}\hat{a}^\dagger} \hat{a} \quad (1.41a)$$

$$\hat{a}^\dagger f_{\hat{a}\hat{a}^\dagger} = f_{\hat{a}^\dagger \hat{a}} \hat{a}^\dagger \quad (1.41b)$$

Combining these facts

$$\begin{aligned} \hat{\mathcal{L}}[f_{\hat{a}^\dagger \hat{a}}] &= 0 = -\frac{1}{2}A\nu \left(\hat{a}\hat{a}^\dagger f_{\hat{a}^\dagger \hat{a}} + f_{\hat{a}^\dagger \hat{a}} \hat{a}\hat{a}^\dagger - 2\hat{a}^\dagger f_{\hat{a}^\dagger \hat{a}} \hat{a} \right) \\ &\quad - \frac{1}{2}A(\nu+1) \left(\hat{a}^\dagger \hat{a} f_{\hat{a}^\dagger \hat{a}} + f_{\hat{a}^\dagger \hat{a}} \hat{a}^\dagger \hat{a} - 2\hat{a} f_{\hat{a}^\dagger \hat{a}} \hat{a}^\dagger \right) \end{aligned} \quad (1.42)$$

Using (1.41a) terms cancel to leave [14]

$$(\hat{N} + 1) \left[(\nu + 1)f_{\hat{N}+1} - \nu f_{\hat{N}} \right] = \hat{N} \left[(\nu + 1)f_{\hat{N}} - \nu f_{\hat{N}-1} \right] \quad (1.43)$$

By picking a particular eigenvalue of \hat{N}^3 then this reduces further to

$$(\nu + 1)f_{\hat{N}} = \nu f_{\hat{N}-1} \quad (1.44)$$

and this can be solved to give

$$f_{\hat{N}} = f_0 \left(\frac{\nu}{\nu + 1} \right)^{\hat{N}} \quad (1.45)$$

Finally, as the sum over all eigenvalues must be normalised

$$1 = f_0 \sum_{n=0}^{\infty} \left(\frac{\nu}{\nu + 1} \right)^n \Rightarrow f_0 = \frac{1}{\nu + 1} \quad (1.46)$$

$$\rho_{t \rightarrow \infty} = \frac{1}{\nu + 1} \left(\frac{\nu}{\nu + 1} \right)^{\hat{N}} \quad (1.47)$$

By referring back to (1.34), the interpretation of ν is now as the mean thermal photon number in the thermal bath, as the unpumped state takes the form of a thermal state. This is a special case of the steady state, which in general includes pumping with excited atoms. An example of a thermal state at 2 K for a 21.456 GHz field is shown in Figure 1.5.

³ $\hat{N} = 0$ is simplest, and then using Equation (1.44) it can be shown that any value of \hat{N} will give the same result.

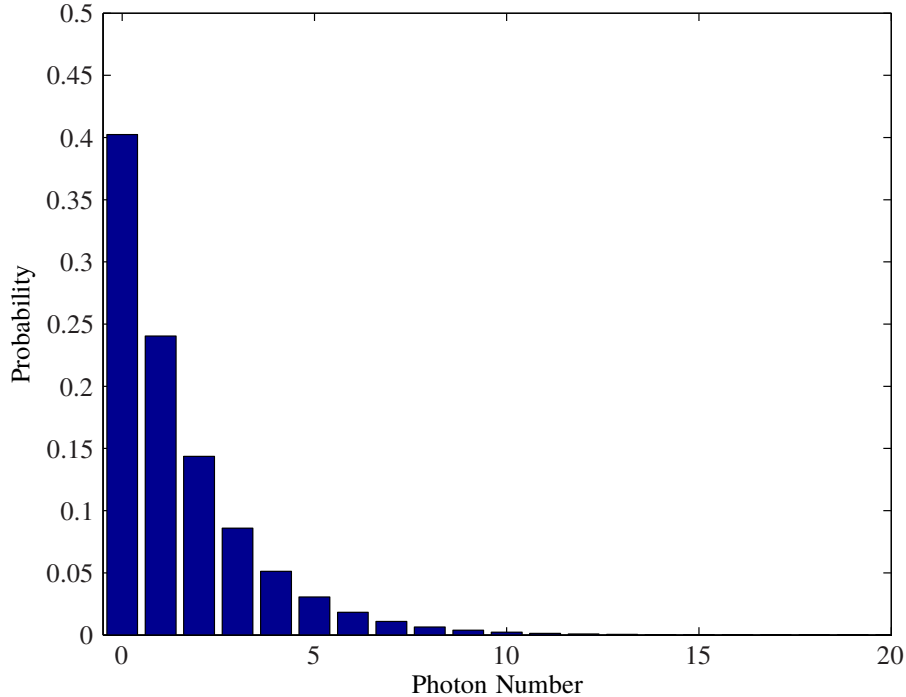


Figure 1.5: This plot shows a thermal field with an average of five photons. This corresponds to a temperature of approximately 2 K for a 21.456 GHz field. As the thermal state is completely classical only the diagonal elements of the density matrix for the field are non-zero, i.e. the probability of a particular number of photons, so this plot fully describes this thermal state.

1.3.2 The Steady State

The steady state of a micromaser pumped with an atomic beam with Poisson statistics is the generalisation of the unpumped state. This is only a steady state on average. The field is pumped in the relatively very short time of the interaction with an atom, and then decays in the time it takes for the next atom to arrive. Like the unpumped state, the steady state when the system is pumped with atoms only in the excited state is also fully mixed. The steady state is thus diagonal in the number state basis [14]

$$\lim_{t \rightarrow \infty} P(n) = C \left(\frac{\nu}{1 + \nu} \right)^n \prod_{k=1}^n \left(1 + \frac{R}{\gamma \nu} \frac{\sin^2(\Theta \sqrt{k \gamma / R})}{k} \right), \quad (1.48)$$

where C normalises the probability distribution, γ^{-1} is the cavity lifetime and $\Theta = g t_{\text{int}} \sqrt{R/\gamma}$ is the micromaser pump parameter. This equation comes from a generalised form of the recursion relation for the unpumped state, and reduces to the unpumped state in the limit of no atomic injection. When $R = 0$ the field is unpumped, and Equation (1.48) reduces to Equation (1.47). Figure 1.6 is

an example probability distribution of a micromaser unpumped and pumped with atoms. Figure 1.7 shows a plot of how the pump parameter affects the number distribution, revealing some important characteristics of the micromaser. Unusual blips appearing at low photon numbers are *trapping states*.

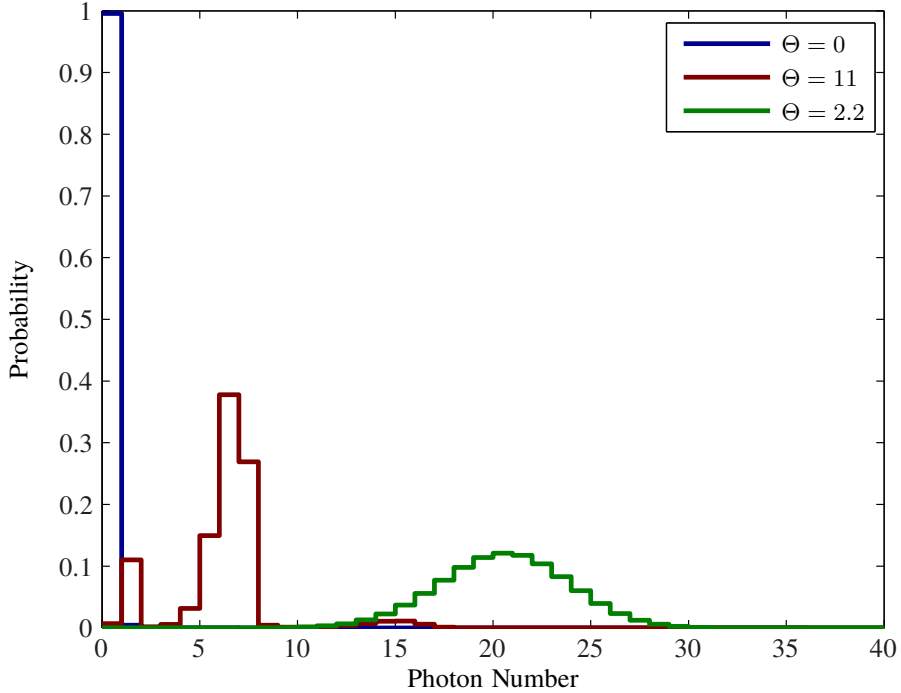


Figure 1.6: This plot shows three steady states of the field. Each distribution corresponds to a different pump rate at 30 mK with a field resonant at 21.456 GHz to simulate our micromaser. The blue is for a thermal distribution, which is mainly in the zero photon state for this temperature. The green is a field pumped close to threshold. The red is a field pumped above threshold. These are all vertical slices of Figure 1.7.

states. These are states for which the field has built up until it has hit a particular number state for which that pump parameter prohibits the emission of a photon, halting the gain in photon number. The distribution of these trapping states is close to a number state, which is how number states were achieved in a micromaser [20–24].

1.4 Phase Diffusion and Linewidth

Phase diffusion of the field in an cavity is the term used to describe the loss of coherence due to interactions between the field and the environment [15]. Figure 1.9 shows this behaviour for the extreme of a coherent state that has fully dephased into a mixed state. Measuring the phase diffusion and linewidth of a micromaser field is yet to be done. The ultimate purpose of the micromaser at Leeds (initially at Sussex University) is to measure these quantities. Previous generations of micromaser were incapable of this measurement due to heating issues. This new micromaser

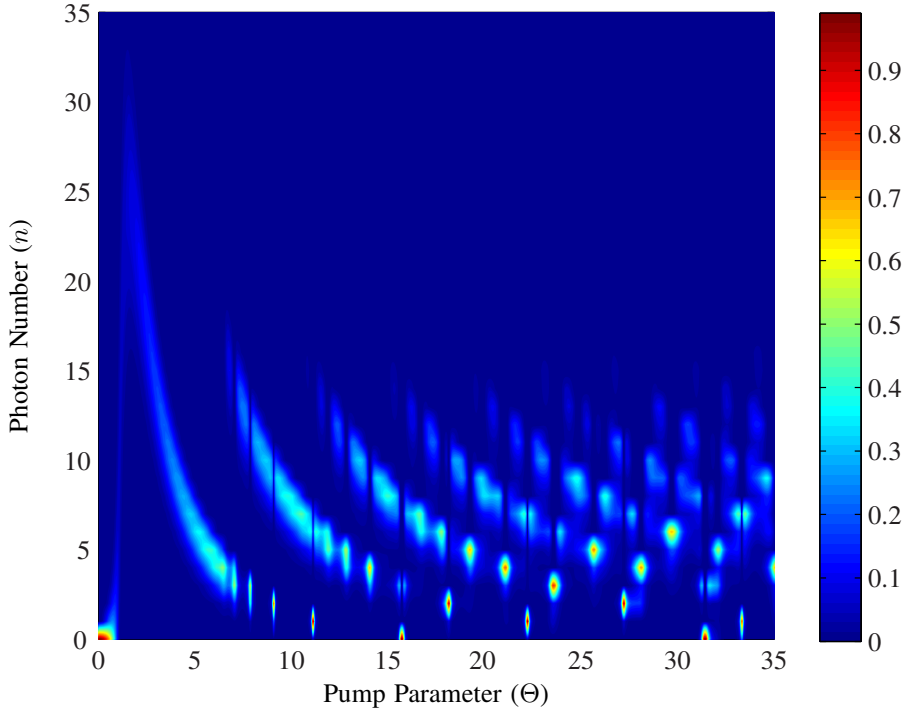


Figure 1.7: This plot shows the effect that increasing the pump parameter has on the photon number distribution. The colour bar corresponds to probability. For this plot $R/\gamma = 25$ and the temperature is 30 mK. Contrast this with Figure 1.8 which is at 500 mK. Much of the interesting character becomes washed out. Vertical slices taken at $\Theta = 0, 2.2, 11$ correspond to the distributions shown in Figure 1.6.

is designed to run in a prototype VeriCold helium dilution cryostat, which can achieve lower temperatures (down to 30 mK) than any other micromaser to date. As the new micromaser is designed with phase diffusion measurements in mind, this section occasionally digresses into experimental details of our system.

The linewidth of the maser field happens to be proportional to the phase diffusion constant (like a decay constant) [15]. The scaled linewidth of the micromaser is given as

$$\frac{D}{\gamma} = \frac{4R}{\gamma} \sin^2 \left(\frac{gt_{\text{int}}}{4\sqrt{\langle n \rangle}} \right) + \frac{(2\nu + 1)}{4\langle n \rangle}. \quad (1.49)$$

For a cavity with large average photon number, or if the interaction time between the field and atoms passing through is small, this reduces to the Schawlow-Townes linewidth of a maser (or laser) due to purely quantum noise [15],

$$\frac{D}{\gamma} = \frac{\Theta^2 + 2\nu + 1}{4\langle n \rangle}. \quad (1.50)$$

The linewidth D is also the the decay constant associated with phase diffusion, thus producing a

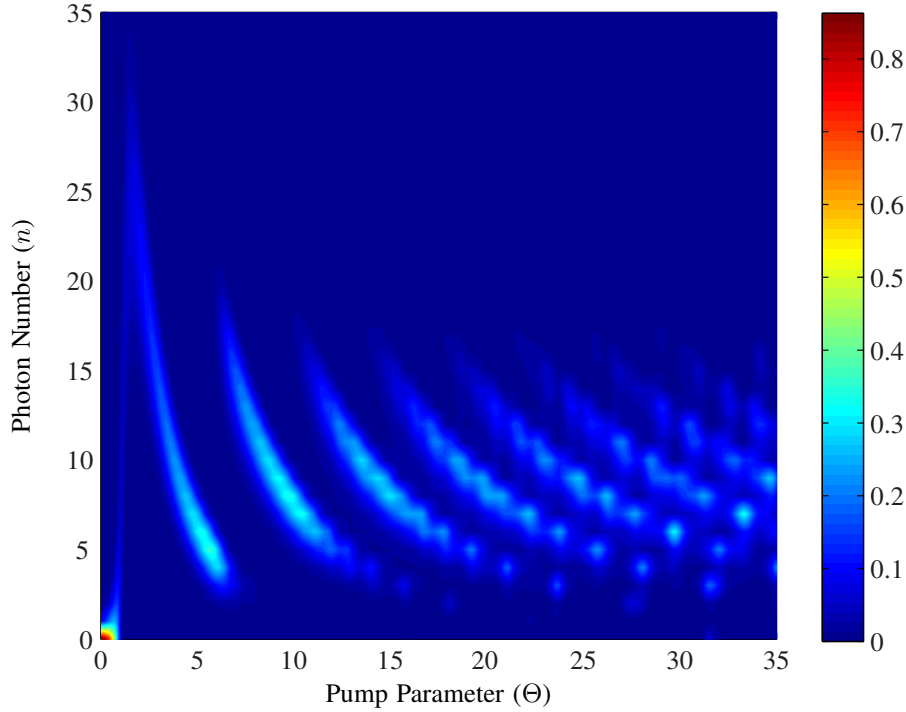


Figure 1.8: This plot is identical to 1.7, except that the temperature is now 500 mK, washing out some of the character of the previous plot. Trapping states in particular are no longer visible.

link between the linewidth of an ideal laser and the decoherence of a cavity field [16, 17].

1.4.1 Measuring Phase Diffusion

Measuring the linewidth of a micromaser is particularly challenging. The quality of the cavity is so high that no direct measurement of the linewidth can be made. The procedure to measure this has been published [16], but the experiment is so difficult that it remains to be performed. The off diagonal elements of the density operator in the number basis decay with a decay rate proportional to the linewidth of the micromaser. The steady state of the field is completely mixed. If a steady state is found that has identical photon number expectations to a coherent field as in Equation (1.51), then this can be exploited [15, 16].

$$p_n^\alpha = p_n^{\text{SS}} \quad (1.51)$$

A possible procedure is as follows

- A cavity is initially pumped from the unpumped state close to 0 K with a coherent field. In the laboratory this is done by firing resonant microwaves from a microwave synthesiser (a coherent source) at one of the openings into the cavity. The use of an external field in this manner is explored in a paper by Agarwal *et al.* [18]

- Atoms are sent through the cavity so that the pump parameter corresponds to a steady state with diagonal elements of the density operator in the number basis identical to the prepared coherent state, as in (1.51). The lifetime of the cavity is long enough that many atoms can interact before the coherences in the field decay. The constant measurement of atoms after leaving the field and the energy decay from the cavity leads to the decay of off-diagonal elements (mixing) as the field loses its coherence.
- After some time, the field can be displaced back by altering the amplitude and detuning of the original external field and applying it again [18], and measurements of the atoms exiting the system can be used to reveal some information about how diffuse the field state became. In the case of no diffusing, the coherent state is simply returned to the vacuum and atoms sent through in the ground state will all exit in the ground state. If some diffusion has occurred then the reverse displacement will not return the field to the vacuum state, and some atoms will be detected in the excited state.

Figure 1.9 shows plots of the Husimi quasi-probability distributions of the cavity field at each stage of such an experiment. The Husimi distribution is

$$Q(\alpha) = \frac{1}{\pi} \langle \alpha | \rho | \alpha \rangle , \quad (1.52)$$

where $|\alpha\rangle$ is a coherent state defined by the equation [26],

$$|\alpha\rangle = e^{-|\alpha|^2/2} \sum_{n=0}^{\infty} \frac{\alpha^n}{\sqrt{n!}} |n\rangle . \quad (1.53)$$

The Husimi distribution at a point α is like the overlap between a density operator and a coherent state $|\alpha\rangle$. In the case of these plots the field has become fully dephased, but in a real experiment the time between the second and third plot would be varied to measure the process of dephasing.

An alternative, and potentially more easily performed, experiment for measuring the phase diffusion is with a modified Ramsey type experiment [15]. In this set up incoming atoms are exposed to resonant microwave radiation to place them in a superposition of the ground and excited states. This in turn introduces coherence to a cavity field. Atoms emerging are rotated by a second field prior to measurement. This is a modified phase sensitive micromaser. After some time the resonant microwave radiation is switched off, and the statistics of outgoing atoms used to infer the decay of the off diagonal elements of the cavity field. From Scully *et al.* [15] the probability of detecting atoms in the excited state is

$$P_e = \frac{1}{2} + e^{-Dt/2} \sum_n \cos(\phi - \beta) \cos(gt\sqrt{n+2}) \sin(gt\sqrt{n+1}) \rho_{n,n+1} , \quad (1.54)$$

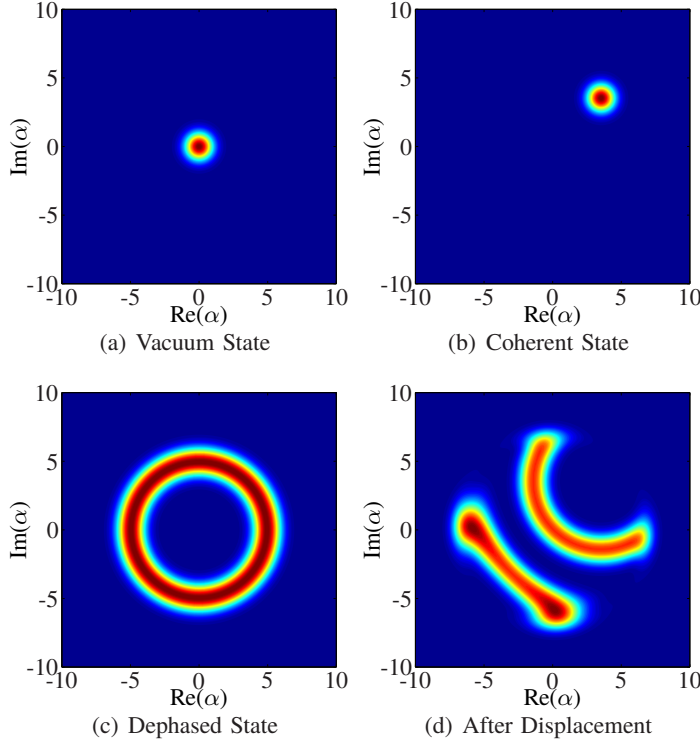


Figure 1.9: These four Husimi ($Q(\alpha)$) distributions of the simulated cavity field demonstrate the various stages of an experiment to measure phase diffusion. (a) The cavity is cooled to the zero photon state. (b) The field is displaced using a coherent source [18]. (c) The atomic beam of excited atoms is switched on to maintain the average photon number. (d) The reverse displacement is performed [18]. The photon number expectation depends on how mixed the state of the field has become. The initial displacement in these plots is to $\langle n \rangle = 25$. The final state is $\langle n \rangle \approx 24$.

where ϕ is the phase of the second rotation field, and β is the initial phase of the micromaser field. Both experiments would require many repetitions to develop the probability against time to calculate D . In a micromaser such as the one at Leeds this kind of repetition is simply a programming problem that is easily solved to automate the entire process. A diagram of the *phase-sensitive* micromaser concept [19] is given in Figure 1.10.

1.5 Summary

Current work on the micromaser is towards building a phase sensitive micromaser as shown in Figure 1.10, in order to measure phase diffusion. This figure belies the difficulty in manufacturing such an experiment. The most extreme constraint is the low temperatures required. The micromaser we are building is designed to operate at a constant 30 mK, which requires a recently acquired helium dilution cryostat, which is expensive to acquire and requires skilled operators. Another

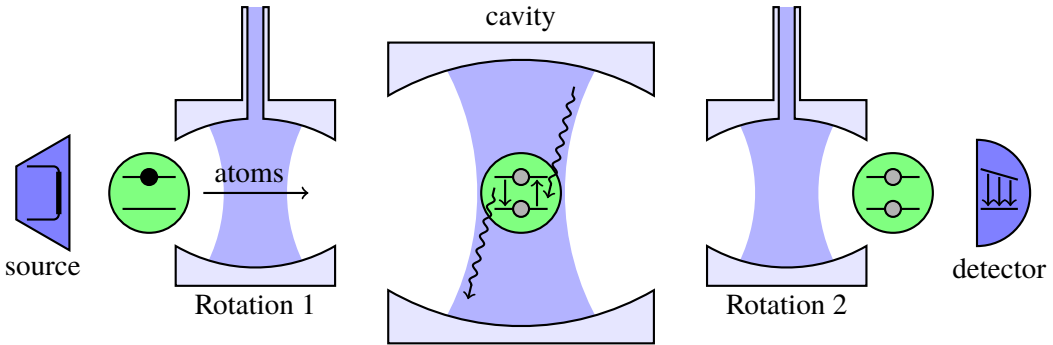


Figure 1.10: The phase sensitive micromaser. This arrangement allows for Ramsey spectroscopy of the cavity field to measure coherences. The two smaller cavities are pumped externally, and simply rotate the state of the atom between $|e\rangle$ and $|g\rangle$. In a laboratory these may be pumped cavities, or waveguide with holes in to allow atoms to pass. The rotations performed by these cavities can be adjusted to measure phase diffusion by injecting coherence initially, and later adjusting again to measure coherence remaining.

major constraint is the cavity. High quality factor cavities in the microwave regime are typically machined out of niobium, which requires specialist knowledge and equipment. In addition, the cavity must be etched and baked, and there are no set methods for doing this. Producing atoms that approximate a two state system is also very difficult. These are pumped using a set of three lasers which are elaborately locked. Measuring the atoms has also proven to be a difficult problem [75]. These issues are explored in greater depth in Part III of this thesis.

Part II

Theory

Chapter 2

Multi-mode Quantum Optical Logic

In collaboration with Dr. Barry Garraway at the University of Sussex I did some work on a cavity quantum electrodynamics (QED) based implementation of a universal quantum gate set. Our motivation was to use the relatively long life time of a cavity field to store all information in the system. The interaction with an atom should simply allow quantum logic gates [31] to be applied to the photonic register, and the atom should exit the cavity in a state separable from the photonic register. Preliminary work was published in conference proceedings [28], and the full architecture has been submitted for publication.

This approach enjoys several advantages. Qubits are stored as a single photon in two modes like the dual-rail qubits developed by Knill, Laflamme and Milburn [76]. If the photon is in the first mode, then the qubit is a $|1\rangle$ and if the photon is in the second then the qubit is in a $|0\rangle$. Table 2.1 shows these two mode qubits. If the photon escapes from the system then the resulting state of the

Modes	Qubit
$ 1, 0\rangle$	$ 1\rangle$
$ 0, 1\rangle$	$ 0\rangle$

Table 2.1: A qubit is encoded as a single excitation shared between two modes of the field, $|n_1, n_2\rangle$. A logical one maps to the excitation being in the first mode, and the logical zero maps to the excitation being in the second mode.

field does not encode a qubit and the error may be detected. This sort of encoding may be extended to the qudit case which encodes information in a system with d orthogonal states, as shown in table 2.2. In order to process quantum information you have to be able to initialise the qubits to the right values, process the qubits, and read out the result. As the qubit consists of two fields in number states, we can use a standard Jaynes-Cummings interaction to initialise the system. Readout can be done in a similar fashion. The challenge here was constructing gates to operate on these qubits.

Modes	Qubit
$ n, 0\rangle$	$ n\rangle$
$ n - 1, 1\rangle$	$ n - 1\rangle$
\vdots	\vdots
$ 1, n - 1\rangle$	$ 1\rangle$
$ 0, n\rangle$	$ 0\rangle$

Table 2.2: Similarly to Table 2.1, qudits can be encoded on a pair of field modes. In this generalisation the number of photons remains constant.

In this chapter I have used the convention for atomic operators given by the equation

$$\hat{\sigma}_{\alpha\beta} = |\alpha\rangle \langle\beta| . \quad (2.1)$$

I made this choice to keep the equations more compact and readable. Sometimes I will use a comma to separate the two states i.e. $\hat{\sigma}_{01,10} = |01\rangle \langle 10|$. Throughout this thesis I use $\hat{\sigma}_3 = \hat{\sigma}_{ee} - \hat{\sigma}_{gg}$ for two level atoms.

2.1 Theory of Effective Hamiltonians

This work relies heavily on the theory of constructing an effective Hamiltonian and specifically the work of Bruce Shore [29]. To a lesser extent the work of Cook and Shore [30] was also useful for working with N -level Hamiltonians. The phrase *adiabatic elimination* is also commonly used.

The theory in [29] is shown only for an effective two level system, but the method also works for an effective multi-level system. If the Hamiltonian is formulated as a matrix with the states of interest in the top left, and those that should be eliminated by special conditions of the system in the bottom right, then the matrix may be divided into parts,

$$H = \begin{pmatrix} H_0 & B \\ B^\dagger & A \end{pmatrix} , \quad (2.2)$$

where part H_0 contains those states that should dominate. In practice this occurs when other states are detuned from resonance, or the couplings to states that are important are relatively large. Mathematically both cases occur when the eigenvalues of A are much larger than the eigenvalues of H_0 . The Schrödinger equation is (in natural units)

$$i \frac{d}{dt} |\Psi\rangle = H |\Psi\rangle . \quad (2.3)$$

A solution can be expressed as

$$|\Psi(t)\rangle = \frac{1}{2\pi i} \int e^{izt} (z - H)^{-1} dz |\Psi(0)\rangle . \quad (2.4)$$

Projection operators can be defined to select out the components of the Hamiltonian of interest.

$$\begin{aligned} P + Q &= \mathbb{1} \\ PP &= P \\ QQ &= Q \\ PQ &= QP = 0 . \end{aligned} \quad (2.5)$$

I choose P to simply be a matrix with ones on the diagonal corresponding to H_0 , and Q to be a matrix with ones on the remaining diagonals, trivially satisfying the above relations. As P selects out the states of interest it can be placed either side of the kernel of Equation (2.4). The blockwise nature of the kernel allows its inversion in terms of these blocks, and as the only block of interest is the one describing the motion of the relevant states, the projection operator P is used to select out the top left element of the resultant blockwise matrix. It is anticipated that other states of the system are so far from resonance that the block couplings between the top left and the lower right blocks of the resultant Hamiltonian will be weak and can be approximated to zero

$$P(z - H)^{-1}P = \begin{pmatrix} (z - H_0 - B(z - A)^{-1}B^\dagger)^{-1} & 0 \\ 0 & 0 \end{pmatrix} . \quad (2.6)$$

The top left element can be substituted back into Equation (2.4),

$$|\psi(t)\rangle = \frac{1}{2\pi i} \int e^{izt} \left(z - H_0 - B \frac{1}{z - A} B^\dagger \right)^{-1} dz |\psi(0)\rangle , \quad (2.7)$$

where $|\psi(t)\rangle$ contains only the states of interest. In the limit of large eigenvalues of A compared with those of H_0 , i.e. these states are detuned, the approximation $z - A \approx -A$ is valid [29]. Comparing Equation (2.7) with (2.4) in this approximation leads to the effective Hamiltonian,

$$H_{\text{eff}} = H_0 - BA^{-1}B^\dagger . \quad (2.8)$$

In this chapter I use this matrix formalism because the systems I have developed all have closed Hilbert spaces, and inverting a matrix is relatively simple. For the case of large or infinite Hilbert spaces using operator formalism is often most efficient. An example of this is in Chapter 3, where the evolution operator for a system is designed to produce generalised W states.

2.2 Single Qubit Rotations

For a universal gate set I needed a multi-qubit entangling gate and two rotations on the Bloch sphere of each single qubit [31]. For the two rotations on the Bloch sphere, I chose rotations about the x and z axes.

2.2.1 Rotations about the z -axis

Rotations about the z -axis are very simple. If a ground state atom passing through the cavity has a transition closer to the frequency of one mode of the qubit than the second (but still detuned from both), then this mode undergoes faster phase evolution than the second effectively forming a rotation about z .



Figure 2.1: The detuned Jaynes-Cummings model is used to produce z -axis rotations. If no photon is present, then no interaction occurs. If a photon is present then (in the detuned case) the phase of the system evolves due to virtual exchange of the excitation between the atom and the field.

In [19] the phase evolution of a detuned Jaynes-Cummings model is given by two formulae

$$|g, n\rangle \mapsto e^{-i\Phi(n)} |g, n\rangle , \quad (2.9)$$

where $\Phi(n)$ is given by

$$\Phi(n) = \frac{\Delta}{2v} \int_0^L \left[\sqrt{1 + n \left(\frac{2g(x)}{\Delta} \right)^2} - 1 \right] dx , \quad (2.10)$$

where v is the velocity of atoms passing though. I am only interested in the states of the field with zero or one photon. In the case of zero photons Φ reduces to zero, and for one photon a non-zero quantity dependent on the profile of the field mode. This is an exact solution, so there is no need to use adiabatic elimination.

For the phase gate we use an atom detuned from one mode of the qubit, and very far detuned from the other. If the photon is in one mode i.e. qubit state $|0\rangle$ the atom sees the closer tuned field

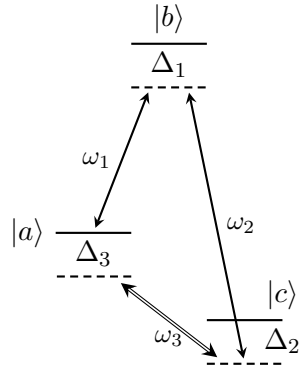


Figure 2.2: The lambda atom has two transitions which couple to the two cavity modes that make up a qubit. $\Delta_1, \Delta_2 \gg g_1, g_2, \Gamma$ to adiabatically eliminate levels $|b\rangle$ and $|c\rangle$ from the interaction and Δ_3 is chosen to ensure resonance. As noted at the end of Section 2.2.2 the external pump ignores selection rules, which will be remedied in the future by adding a further transition or pumping with a two photon transition.

with zero photons and the system undergoes no accelerated evolution because $\Phi(0) = 0$. In the case of the photon in the other mode, i.e. qubit basis state $|1\rangle$ then the added photon in the closer mode causes faster evolution given by the non-zero $\Phi(1)$.

2.2.2 Rotations about the x -axis

Rotations about the x -axis happened to be far more difficult, and require the atom to couple to both transitions in a lambda configuration, and the ground states to be coupled by a classical field. Chronologically this gate was the final step in developing the universal gate set.

The idea for this system was to introduce an atom in the state $|a\rangle$, see Figure 2.2. If the field is in the configuration $|1, 0\rangle$, which is a $|1\rangle$ qubit state, then the atom may make a transition up to state $|b\rangle$ by absorbing the photon, decay to state $|c\rangle$, emitting a photon into mode two, $|0, 1\rrangle$ and a classical field drives the atom back into state $|a\rangle$, acting as a bit flip with the atom returned to the initial state. For a $|0\rangle$ to $|1\rangle$ the reverse process applies. To realise a rotation about x it must be possible to form a superposition of bit flipped and unflipped states. To do this the atom may be only virtually excited, demanding that states $|b\rangle$ and $|c\rangle$ are detuned from resonance with the modes and classical field, but that the overall resonance is not detuned, leaving only two states of the system $|1, 0, a\rangle$ and $|0, 1, a\rangle$. This satisfies the requirement that the atom is not entangled with the system and that measurement of the atom does not affect the gate.

The level diagram in Figure 2.2 is a lambda scheme with two transitions detuned from the two modes that comprise a qubit. By coupling the ground states together with a classical field, and choosing Δ_3 to allow a multi-photon resonance so that the atom is returned to $|a\rangle$, the system will oscillate between the $|0\rangle$ and $|1\rangle$ qubit states without changing the state of the atom. The choice for

Δ_3 is not clear, as level shifts may cause it to deviate from zero. Once again the theory of effective Hamiltonians is employed [29]. From the level diagram in 2.2 the Hamiltonian is

$$H = \sum_{\alpha=a,b,c} E_\alpha \hat{\sigma}_{\alpha\alpha} + \sum_{i=1}^3 \omega_i \hat{a}_i^\dagger \hat{a}_i + \left[g_1 \hat{a}_1^\dagger \hat{\sigma}_{ab} + g_2 \hat{a}_2^\dagger \hat{\sigma}_{cb} + g_3 \hat{a}_3^\dagger \hat{\sigma}_{ca} + \text{h.c.} \right], \quad (2.11)$$

where h.c. stands for ‘Hermitian conjugate’. I am assuming a classical field for the transition between $|a\rangle$ and $|c\rangle$, so I extract the part of the Hamiltonian describing this quantum field

$$H_{\text{part}} = \omega_3 \hat{a}_3^\dagger \hat{a}_3 + g_3 \left(\hat{a}_3 \hat{\sigma}_{ac} + \hat{a}_3^\dagger \hat{\sigma}_{ca} \right). \quad (2.12)$$

Since the remaining parts of the Hamiltonian commute with \hat{a}_3 I can perform transformations that are a function of \hat{a}_3 and \hat{a}_3^\dagger without the need to consider those parts. A transformation is defined by

$$H' = \hat{T} H \hat{T}^\dagger - i \hat{T} \frac{\delta}{\delta t} \hat{T}^\dagger \quad (2.13)$$

A complete description of unitary transformations is provided in appendix D. For the transformation I choose $\hat{T} = \exp(i\omega_3 \hat{a}_3^\dagger \hat{a}_3 t)$. This yields

$$H'_{\text{part}} = g_3 \left(e^{-i\omega_3 t} \hat{a}_3 \hat{\sigma}_{ac} + e^{i\omega_3 t} \hat{a}_3^\dagger \hat{\sigma}_{ca} \right). \quad (2.14)$$

The result of the transformation is to remove the explicit reference to the energy of the field and replace it with a time dependence. As this field is going to be classical and not quantum, I model it as a coherent state $|\alpha\rangle$. The coherent state is the right-eigenstate of the annihilation operator, which allows me to remove the creation and annihilation operators.

$$H_{\text{class}} = \Gamma \left(e^{-i\omega_3 t} \hat{\sigma}_{ac} + e^{i\omega_3 t} \hat{\sigma}_{ca} \right), \quad (2.15)$$

where $\Gamma = g_3 \alpha$, assuming that α is real without loss of generality. All states of the system will have the same coherent state for the classical field, so it can be factored out and omitted from the wavefunction. This equation can now be substituted back into the full Hamiltonian of the system

$$H = \sum_{\alpha=a,b,c} E_\alpha \hat{\sigma}_{\alpha\alpha} + \sum_{i=1,2} \omega_i \hat{a}_i^\dagger \hat{a}_i + \left[g_1 \hat{a}_1^\dagger \hat{\sigma}_{ab} + g_2 \hat{a}_2^\dagger \hat{\sigma}_{cb} + \Gamma e^{i\omega_3 t} \hat{\sigma}_{ca} + \text{h.c.} \right]. \quad (2.16)$$

The explicit dependence on the absolute energy of the atom is ugly, so I want to transform the Hamiltonian into a form without the first term. In order to do this, it is worth redrawing the level diagram. Figure 2.2 shows cumulative detunings, useful for dealing with multi-photon resonances, but at this stage I need to know the detuning between particular transitions and field modes as

shown in Figure 2.3. These detunings are labelled with lower case δ to distinguish them from the

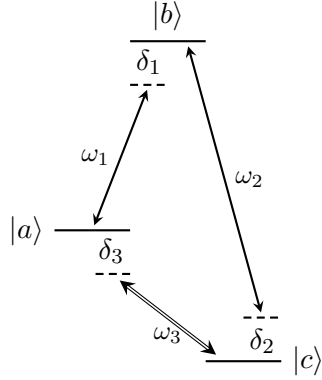


Figure 2.3: This is an alternate representation of the level system depicted in Figure 2.2. The detunings shown in this diagram are between particular transitions and field modes, rather than cumulative multi-transition detunings in the previous diagram.

cumulative detunings which are in upper case. The two labellings are related by the equations

$$\begin{aligned}\Delta_1 &= \delta_1 \\ \Delta_2 &= \delta_1 - \delta_2 \\ \Delta_3 &= \delta_1 - \delta_2 + \delta_3.\end{aligned}\tag{2.17}$$

Using these detunings there is a simple relationship between the transition energies and the mode frequencies,

$$\begin{aligned}E_b - E_a &= \omega_1 + \delta_1 \\ E_b - E_c &= \omega_2 + \delta_2 \\ E_a - E_c &= \omega_3 + \delta_3.\end{aligned}\tag{2.18}$$

Creating a whole new diagram may at first glance seem like wasted effort, but it makes handling the Hamiltonian much neater and less prone to error, especially when calculating transformations. The transformation I used on the Hamiltonian used $\hat{T} = \exp(i\Theta t)$ where Θ was

$$\Theta = \sum_{\alpha=a,b,c} E_\alpha \hat{\sigma}_{\alpha\alpha} + \sum_{i=1,2} \hat{a}_i^\dagger \hat{a}_i (\omega_i + \delta_i)\tag{2.19}$$

Using Θ helps to produce useful operators because the equation for a transformed Hamiltonian reduces to

$$H' = e^{i\Theta t} H e^{-i\Theta t} - \Theta.\tag{2.20}$$

I found that the subtraction of Θ in this equation can give clues about useful forms of Θ to subtract

undesirable parts of the Hamiltonian. Care must be taken with time dependence however, so that if the initial Hamiltonian has no time dependence then the only way to avoid introducing time dependence is if Θ commutes with the initial Hamiltonian, i.e. $\hat{T}H\hat{T}^\dagger = H$.

My choice of Θ leaves a residue in the Hamiltonian, in the form of detunings. I will show that this leads to a very natural way of viewing the Hamiltonian which is useful when working with effective Hamiltonians. In Chapter 1 Equation (1.15) I noted the same form for the Jaynes-Cummings Hamiltonian which is strikingly absent from the literature.

After the transformation the Hamiltonian is

$$H' = - \sum \delta_i \hat{a}_i^\dagger \hat{a}_i + \left[g_1 \hat{a}_1^\dagger \hat{\sigma}_{ab} + g_2 \hat{a}_2^\dagger \hat{\sigma}_{cb} + \Gamma e^{-i\delta_3 t} \hat{\sigma}_{ca} + \text{h.c.} \right]. \quad (2.21)$$

The final stage of preparing the Hamiltonian is removing the remaining time dependence. This requires another transformation. The two transformations could have been done in a single step, but the stepwise approach is more manageable. The next transformation is defined by

$$\Theta' = \frac{1}{2} \left(\hat{a}_1^\dagger \hat{a}_1 - \hat{a}_2^\dagger \hat{a}_2 + \hat{\sigma}_{cc} - \hat{\sigma}_{aa} \right) \delta_3 - \delta_1. \quad (2.22)$$

This transformation removes time dependence in the resultant Hamiltonian. The δ_1 may seem out of place, but this leads to a zero in the upper left corner of the matrix describing the system. This often avoids A becoming singular, which stops an effective Hamiltonian being constructed. In addition it also tends to lead to more physically appealing Hamiltonian matrices in which the detunings appear in sequence when the states are ordered in the state vector, i.e. adjacent states are coupled. The Hamiltonian is now

$$H'' = \delta_1 - \frac{1}{2} \left(\hat{a}_1^\dagger \hat{a}_1 - \hat{a}_2^\dagger \hat{a}_2 + \hat{\sigma}_{cc} - \hat{\sigma}_{aa} \right) \delta_3 - \sum \delta_i \hat{a}_i^\dagger \hat{a}_i + \left[g_1 \hat{a}_1^\dagger \hat{\sigma}_{ab} + g_2 \hat{a}_2^\dagger \hat{\sigma}_{cb} + \Gamma \hat{\sigma}_{ca} + \text{h.c.} \right]. \quad (2.23)$$

I chose the initial state of the atom to be $|a\rangle$, so with the computational basis in mind, the two possible starting states of the system are $|1, 0, a\rangle$ and $|0, 1, a\rangle$, in the order |mode 1, mode 2, atom>. There are two other possible states that may evolve from these two; $|0, 0, b\rangle$ and $|0, 1, c\rangle$. Arranging these in the order $|\Psi\rangle = c_1 |1, 0, a\rangle + c_2 |0, 0, b\rangle + c_3 |0, 1, c\rangle + c_4 |0, 1, a\rangle$ and substituting in Equations (2.17) the Hamiltonian matrix is given as

$$H'' = \begin{pmatrix} 0 & g_1 & 0 & 0 \\ g_1 & \Delta_1 & g_2 & 0 \\ 0 & g_2 & \Delta_2 & \Gamma \\ 0 & 0 & \Gamma & \Delta_3 \end{pmatrix}, |\Psi\rangle = \begin{pmatrix} c_1 \\ c_2 \\ c_3 \\ c_4 \end{pmatrix}. \quad (2.24)$$

The detunings on the diagonal are a direct consequence of my choice of Θ for the first transformation.

It is simple to see from this that those states that are highly detuned will have large eigenvalues which will reduce the transition probability to these states.

The next step is to form a two state effective Hamiltonian from this, in the limit of large detuning. Naïvely this can be done simply by choosing $\Delta_3 = 0$ and $\Delta_1, \Delta_2 \gg g_1, g_2$, however level shifts mean that the choice of Δ_3 may be incorrect. By properly formulating the effective Hamiltonian, the actual condition for the multi-photon resonance will be derived at the same time. First the Hamiltonian is rearranged to put the two states of interest in the top left,

$$H'' = \begin{pmatrix} 0 & 0 & g_1 & 0 \\ 0 & \Delta_3 & 0 & \Gamma \\ g_1 & 0 & \Delta_1 & g_2 \\ 0 & \Gamma & g_2 & \Delta_2 \end{pmatrix}, |\Psi\rangle = \begin{pmatrix} c_1 \\ c_4 \\ c_2 \\ c_3 \end{pmatrix}. \quad (2.25)$$

Using the formula for producing an effective Hamiltonian (2.8) requires that the Hamiltonian is split into parts

$$H_0 = \begin{pmatrix} 0 & 0 \\ 0 & \Delta_3 \end{pmatrix}, \quad A = \begin{pmatrix} \Delta_1 & g_2 \\ g_2 & \Delta_2 \end{pmatrix}, \quad B = \begin{pmatrix} g_1 & 0 \\ 0 & \Gamma \end{pmatrix}. \quad (2.26)$$

By equation (2.8) the resultant effective Hamiltonian is

$$H_{\text{eff}} = \frac{1}{\Delta_1 \Delta_2 - g_2^2} \begin{pmatrix} -\Delta_2 g_1^2 & g_1 g_2 \Gamma \\ g_1 g_2 \Gamma & \Delta_3 (\Delta_1 \Delta_2 - g_2^2) - \Delta_1 \Gamma^2 \end{pmatrix}, \quad |\psi_{\text{eff}}\rangle = \begin{pmatrix} c_1 \\ c_4 \end{pmatrix}. \quad (2.27)$$

This can be reduced further because I have already made the assumption that $\Delta_1, \Delta_2 \gg g_1, g_2$,

$$H_{\text{eff}} \approx \begin{pmatrix} -\frac{g_1^2}{\Delta_1} & \frac{g_1 g_2 \Gamma}{\Delta_1 \Delta_2} \\ \frac{g_1 g_2 \Gamma}{\Delta_1 \Delta_2} & \Delta_3 - \frac{\Gamma^2}{\Delta_2} \end{pmatrix}. \quad (2.28)$$

The difference in the diagonal elements is the effective detuning

$$\Delta_{\text{eff}} \approx \Delta_3 - \frac{\Gamma^2}{\Delta_2} + \frac{g_1^2}{\Delta_1}. \quad (2.29)$$

The effective detuning is a large modification to the expected detuning. Considering that $\Delta_1, \Delta_2 \gg g_1, g_2, \Gamma$, the extra terms in the effective detuning are relatively large when compared to the effective detuning

$$g_{\text{eff}} \approx \frac{g_1 g_2 \Gamma}{\Delta_1 \Delta_2}. \quad (2.30)$$

The solution is the x -rotation gate in the interaction picture,

$$R_x(g_{\text{eff}}t) = \cos(g_{\text{eff}}t)\hat{\sigma}_0 - i \sin(g_{\text{eff}}t)\hat{\sigma}_x, \quad (2.31)$$

when the resonance condition $\Delta_{\text{eff}} = 0$ is satisfied. By performing the reverse transformations on this evolution operator the evolution operator in the Schrödinger picture (neglecting a global phase) is

$$R_x^{\text{Sch}} = \cos(g_{\text{eff}}t)\hat{\sigma}_0 - i \sin(g_{\text{eff}}t)[e^{i\omega_3 t}\hat{\sigma}_{10,01} + e^{-i\omega_3 t}\hat{\sigma}_{01,10}]. \quad (2.32)$$

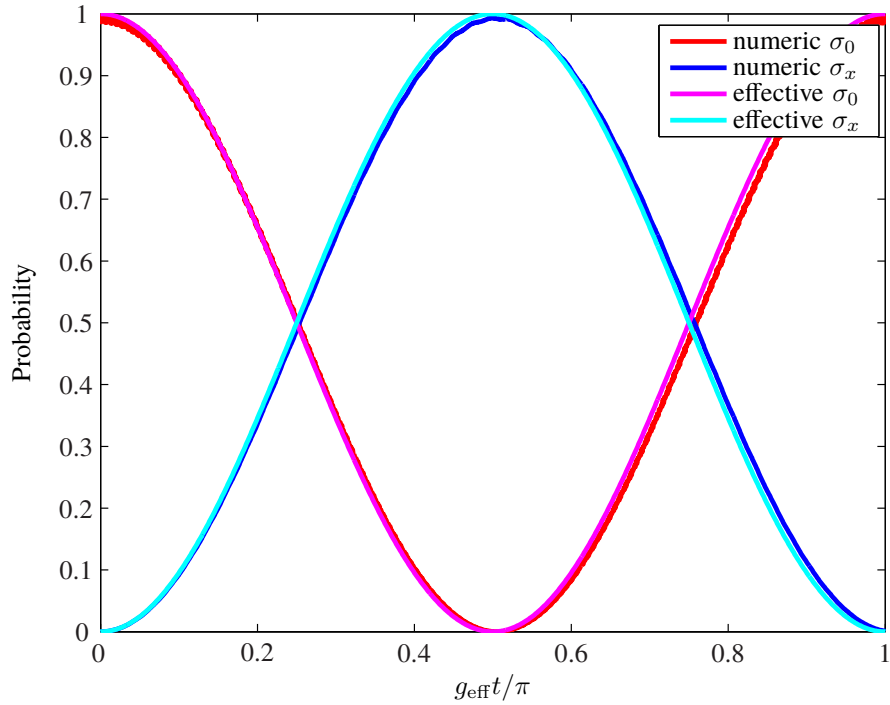


Figure 2.4: This plot shows the numerical prediction based upon the full Hamiltonian, and the prediction of the effective Hamiltonian. Numbers for the coupling constants and detunings were chosen with arbitrary units to be $g_1 = 1.5$, $g_2 = 1.0$, $\Gamma = 0.9$, $\Delta_1 = 25$, $\Delta_2 = 15$. Δ_3 was chosen using the resonance condition which gave -0.0360 in order to counter level shifting. This plot shows that in the appropriate limits the solution of the effective Hamiltonian agrees with the numerical predictions from the full Hamiltonian. The effective coupling constant for this choice of parameters is 0.0036 , an order of magnitude lower than Δ_3 , demonstrating that the effective Hamiltonian is needed to make predictions.

An error in the x -rotation gate in this system will result in the atom exiting in a state other than $|a\rangle$. This can be measured using state-selective field ionisation, forming a rudimentary error check. The fidelity of the gate with and without this check is shown in Figure 2.5.

An issue with the x -rotation as it stands is that the external transition pumps a transition that is against selection rules. This can be remedied by adding a further transition or swapping it for a two mode transition.

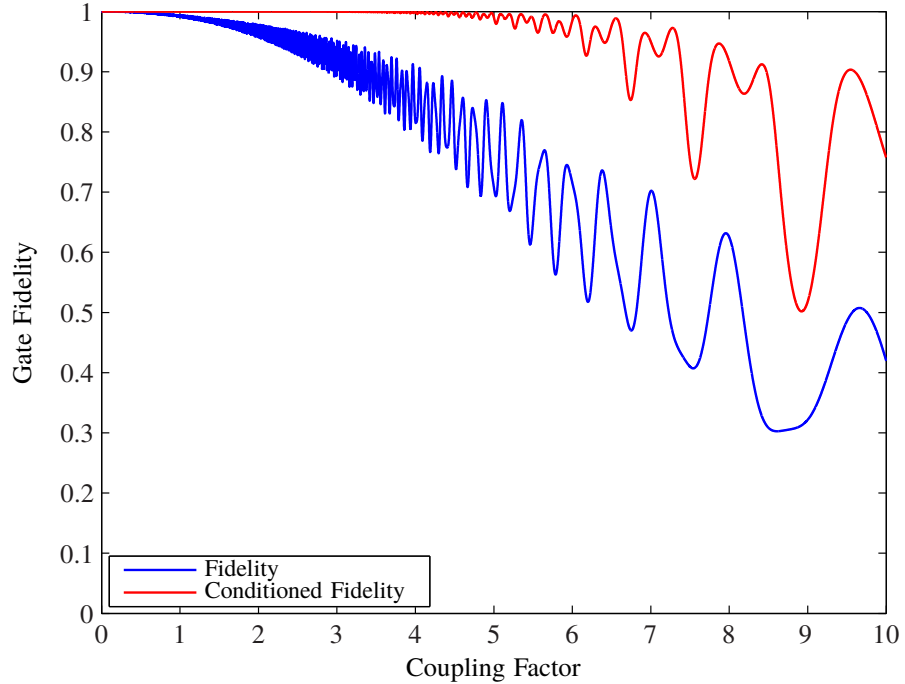


Figure 2.5: This plot uses the numbers from Figure 2.4, but the coupling constants are all multiplied by a ‘coupling factor’, on the x -axis of this plot. The fidelity is the fidelity of the numerical system with the prediction derived from the effective Hamiltonian for a $-i\sigma_x$ gate. The ‘conditioned fidelity’ is the fidelity of the gate conditioned on measuring the outgoing atom in state $|a\rangle$. The gate time for each point is $t = \pi/2g_{\text{eff}}$ where g_{eff} is from equation (2.30). As $g_1, g_2 \ll \Delta_1, \Delta_2$ becomes a worse assumption, the approximations made in deriving g_{eff} break down leading to loss of gate fidelity.

2.3 Entangling Multi-Qubit Gates

2.3.1 The Fredkin Gate

The Fredkin, or controlled swap gate, is a three qubit entangling gate which is universal for classical computation [31]. This was the first gate encoded on this system. The most obvious candidates for a multi-qubit entangling gate are the controlled NOT gate or the controlled phase gate, however I wanted to avoid using classical fields when possible and geometric arguments rule out level diagrams for these two gates without a classical field. The first case which could be done without this operation was the three qubit Fredkin gate. The swap gate was relatively simple to encode, and

Input	Output
$ 0, 0, 0\rangle$	$ 0, 0, 0\rangle$
$ 0, 0, 1\rangle$	$ 0, 0, 1\rangle$
$ 0, 1, 0\rangle$	$ 0, 1, 0\rangle$
$ 0, 1, 1\rangle$	$ 0, 1, 1\rangle$
$ 1, 0, 0\rangle$	$ 1, 0, 0\rangle$
$ 1, 0, 1\rangle$	$ 1, 1, 0\rangle$
$ 1, 1, 0\rangle$	$ 1, 0, 1\rangle$
$ 1, 1, 1\rangle$	$ 1, 1, 1\rangle$

Table 2.3: The truth table for the Fredkin (controlled swap) gate. This is a three qubit entangling gate, which when complemented with the single qubit rotations forms a universal set of gates for quantum computation.

by adding another energy level it was possible to add in the control qubit. Figure 2.6 shows the arrangement of levels and field modes that transitions couple to.

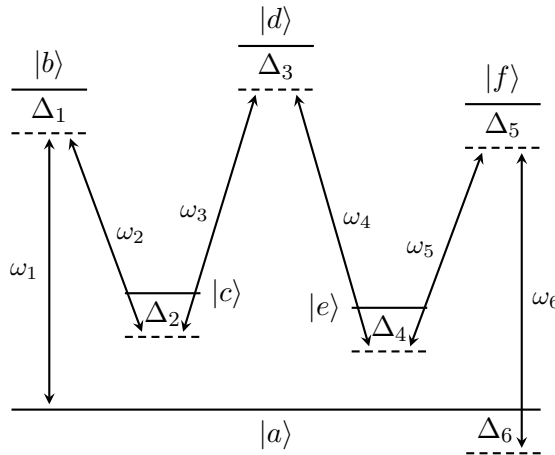


Figure 2.6: This level diagram is what is required to simulate a Fredkin gate. Note that mode one couples to two transitions. To simplify the derivation of the Hamiltonian in a particular interaction picture mode four does not feature in this diagram. In reality this diagram would be folded up for dipole allowed transitions; this layout is meant for aid in calculation.

2.3.1.1 The Hamiltonian

It is probably simpler to retroactively justify my choice of level system, so I will show how I derived the Hamiltonian and how it can be used as a Fredkin gate in the hope that the reader gains an

understanding through my working. The Hamiltonian in the Schrödinger picture is

$$H = \sum_{\alpha} E_{\alpha} \hat{\sigma}_{\alpha\alpha} + \sum_{i=1}^5 \omega_i \hat{a}_i^\dagger \hat{a}_i + \left[g_1 \hat{\sigma}_{ba} \hat{a}_1 + g_2 \hat{\sigma}_{cb} \hat{a}_2^\dagger + g_3 \hat{\sigma}_{dc} \hat{a}_3 + g_4 \hat{\sigma}_{ed} \hat{a}_1^\dagger + g_5 \hat{\sigma}_{fe} \hat{a}_5 + g_6 \hat{\sigma}_{af} \hat{a}_6^\dagger + \text{h.c.} \right], \quad (2.33)$$

where α runs over the energy levels in the diagram. The first transformation I make on this Hamiltonian produces a Hamiltonian in the form of Equation (1.15). This puts the Hamiltonian in the correct form but with some additional time dependence. The transformation is given by

$$\Theta = \sum_{\alpha} E_{\alpha} \hat{\sigma}_{\alpha\alpha} + \sum_{i=1}^5 \hat{a}_i^\dagger \hat{a}_i (\omega_i + \delta_i) . \quad (2.34)$$

Once again I am using the lower case deltas defined by

$$\begin{aligned} E_b - E_a &= \omega_1 + \delta_1 & \Delta_1 &= \delta_1 \\ E_b - E_c &= \omega_2 + \delta_2 & \Delta_2 &= \delta_1 - \delta_2 \\ E_d - E_c &= \omega_3 + \delta_3 & \Delta_3 &= \delta_1 - \delta_2 + \delta_3 \\ E_d - E_e &= \omega_4 + \delta_4 & \Delta_4 &= \delta_1 - \delta_2 + \delta_3 - \delta_4 \\ E_f - E_e &= \omega_5 + \delta_5 & \Delta_5 &= \delta_1 - \delta_2 + \delta_3 - \delta_4 + \delta_5 \\ E_f - E_a &= \omega_6 + \delta_6 & \Delta_6 &= \delta_1 - \delta_2 + \delta_3 - \delta_4 + \delta_5 - \delta_6 . \end{aligned} \quad (2.35)$$

The frequency coloured in red is coloured to highlight that it is the second transition with ω_1 when an ω_4 would be expected. As this system is supposed to include three qubits it appears that it is one mode short. The missing mode four is partnered with mode one to form a qubit, and it does not appear on the diagram because it is not close to resonance to any of the transitions. When the photon is in mode one, this system can make transitions around the loop of states. When the photon is in mode four, and for the appropriate detunings, the system cannot make any transitions. This is the mechanism that allows this pair of modes to form the control qubit.

The Hamiltonian after this transformation is

$$H = - \sum_{i=1}^5 \delta_i \hat{a}_i^\dagger \hat{a}_i + \left[g_1 \hat{\sigma}_{ba} \hat{a}_1 + g_2 \hat{\sigma}_{cb} \hat{a}_2^\dagger + g_3 \hat{\sigma}_{dc} \hat{a}_3 + g_4 e^{i(\delta_1 - \delta_4)t} \hat{\sigma}_{ed} \hat{a}_1^\dagger + g_5 \hat{\sigma}_{fe} \hat{a}_5 + g_6 \hat{\sigma}_{af} \hat{a}_6^\dagger + \text{h.c.} \right] . \quad (2.36)$$

The second term with mode one has gained a time dependency which I remove with the next

transformation, which is defined by

$$\Theta' = \left(\hat{a}_1^\dagger \hat{a}_1 + \hat{a}_2^\dagger \hat{a}_2 + \hat{a}_3^\dagger \hat{a}_3 + \hat{a}_6^\dagger \hat{a}_6 - \hat{\sigma}_{aa} - \hat{\sigma}_{cc} \right) (\delta_4 - \delta_1) - \delta_3 - \delta_4 - \delta_5. \quad (2.37)$$

This second transformation yields a Hamiltonian which will later produce Hamiltonian matrices with a zero in the top left corner and ascending detunings for the right ordering of states, just as in Equation (2.25) for the x -rotation gate. This leaves the Hamiltonian in the final form

$$H = \left(\hat{a}_1^\dagger \hat{a}_1 + \hat{a}_2^\dagger \hat{a}_2 + \hat{a}_3^\dagger \hat{a}_3 + \hat{a}_6^\dagger \hat{a}_6 - \hat{\sigma}_{aa} - \hat{\sigma}_{cc} \right) (\delta_1 - \delta_4) + \delta_3 + \delta_4 + \delta_5 - \sum_{i=1}^5 \delta_i \hat{a}_i^\dagger \hat{a}_i \\ + \left[g_1 \hat{\sigma}_{ba} \hat{a}_1 + g_2 \hat{\sigma}_{cb} \hat{a}_2^\dagger + g_3 \hat{\sigma}_{dc} \hat{a}_3 + g_4 \hat{\sigma}_{ed} \hat{a}_1^\dagger + g_5 \hat{\sigma}_{fe} \hat{a}_5 + g_6 \hat{\sigma}_{af} \hat{a}_6^\dagger + \text{h.c.} \right]. \quad (2.38)$$

This system has six modes. As I was to choose how I paired these modes up to make qubits, I used the arrangement

$$|q_1, q_2, q_3\rangle = |n_1 n_4, n_2 n_3, n_5 n_6\rangle. \quad (2.39)$$

As the Fredkin gate is simply a controlled swap operation, I eventually wanted to get

$$|1, 0, 1\rangle |a\rangle \leftrightarrow |1, 1, 0\rangle |a\rangle, \quad (2.40)$$

with all other states of the system remaining at, or returning to, their initial state at some time t . A list of the states of the system is given in table 2.4. The states in red in the table are the same ones

Qubits	Field Modes
$ 0, 0, 0\rangle$	$ 0, 1; 0, 1; 0, 1\rangle$
$ 0, 0, 1\rangle$	$ 0, 1; 0, 1; 1, 0\rangle$
$ 0, 1, 0\rangle$	$ 0, 1; 1, 0; 0, 1\rangle$
$ 0, 1, 1\rangle$	$ 0, 1; 1, 0; 1, 0\rangle$
$ 1, 0, 0\rangle$	$ 1, 0; 0, 1; 0, 1\rangle$
$ 1, 0, 1\rangle$	$ 1, 0; 0, 1; 1, 0\rangle$
$ 1, 1, 0\rangle$	$ 1, 0; 1, 0; 0, 1\rangle$
$ 1, 1, 1\rangle$	$ 1, 0; 1, 0; 1, 0\rangle$

Table 2.4: Encoding of three qubits in the multi-mode Fredkin gate system. The order the modes are listed in is given in Equation (2.39). The states in red are swapped when the Fredkin gate acts upon them. The other states should remain unchanged.

in Equation 2.40. I need to check that I can make these two states swap at some time t , and that at the same time and under the same conditions (detunings) the other states are unchanged.

Now I can justify my choice of level system. Translating the left hand side of Equation 2.40 into which modes have an excitation by using Equation 2.39, yields modes one, three and five

with a single photon, and modes two, four and six with zero. Referring to the level diagram in Figure 2.6, the accessible states of the system are simple to find and are given in table 2.5. If

Qubits	Field Modes	Atom
$ 1, 0, 1\rangle$	$ 1, 0; 0, 1; 1, 0\rangle$	$ a\rangle$
	$ 0, 0; 0, 1; 1, 0\rangle$	$ b\rangle$
	$ 0, 0; 1, 1; 1, 0\rangle$	$ c\rangle$
	$ 0, 0; 1, 0; 1, 0\rangle$	$ d\rangle$
$ 1, 1, 1\rangle$	$ 1, 0; 1, 0; 1, 0\rangle$	$ e\rangle$
	$ 1, 0; 1, 0; 0, 0\rangle$	$ f\rangle$
$ 1, 1, 0\rangle$	$ 1, 0; 1, 0; 0, 1\rangle$	$ a\rangle$
	$ 0, 0; 1, 0; 0, 1\rangle$	$ b\rangle$
	$ 0, 0; 2, 0; 0, 1\rangle$	$ c\rangle$

Table 2.5: A list of the states of the system that may evolve from $|1, 0, 1\rangle|a\rangle$. Blanks in the qubits column are when a state of the field does not map to qubits.

the intermediate states of the system, shown in black in Table 2.5, are all detuned but retain the multi-photon resonance between the two states of the field with the atom in state $|a\rangle$, shown in red in Table 2.5, then the system will Rabi flop between the two states I want. This trivially works for all the other states of the qubits because they cannot form a chain between two states of the system that begin and end with the atom in state $|a\rangle$.

2.3.1.2 Effective Two-Level Case

Now that the list of accessible states is known I can construct a matrix version of the Hamiltonian

$$H = \begin{pmatrix} 0 & g_1 & 0 & 0 & 0 & 0 & 0 & 0 & 0 \\ g_1 & \Delta_1 & g_2 & 0 & 0 & 0 & 0 & 0 & 0 \\ 0 & g_2 & \Delta_2 & g_3 & 0 & 0 & 0 & 0 & 0 \\ 0 & 0 & g_3 & \Delta_3 & g_4 & 0 & 0 & 0 & 0 \\ 0 & 0 & 0 & g_4 & \Delta_4 & g_5 & 0 & 0 & 0 \\ 0 & 0 & 0 & 0 & g_5 & \Delta_5 & g_6 & 0 & 0 \\ 0 & 0 & 0 & 0 & 0 & g_6 & \Delta_6 & g_1 & 0 \\ 0 & 0 & 0 & 0 & 0 & 0 & g_1 & \Delta_6 + \Delta_1 & g_2\sqrt{2} \\ 0 & 0 & 0 & 0 & 0 & 0 & 0 & g_2\sqrt{2} & \Delta_6 + \Delta_2 \end{pmatrix}. \quad (2.41)$$

The most obvious next step is to make an effective two state Hamiltonian. This is not, however, necessary as three or four state Hamiltonians are also possible. The two state system is the simplest to handle so I will show this first. Rearranging the Hamiltonian so that the first and sixth states are

in the top left, and splitting it into the components needed to construct the effective Hamiltonian

$$H_0 = \begin{pmatrix} 0 & 0 \\ 0 & \Delta_6 \end{pmatrix}$$

$$B = \begin{pmatrix} g_1 & 0 & 0 & 0 & 0 & 0 & 0 \\ 0 & 0 & 0 & 0 & g_6 & g_1 & 0 \end{pmatrix}$$

$$A = \begin{pmatrix} \Delta_1 & g_2 & 0 & 0 & 0 & 0 & 0 \\ g_2 & \Delta_2 & g_3 & 0 & 0 & 0 & 0 \\ 0 & g_3 & \Delta_3 & g_4 & 0 & 0 & 0 \\ 0 & 0 & g_4 & \Delta_4 & g_5 & 0 & 0 \\ 0 & 0 & 0 & g_5 & \Delta_5 & 0 & 0 \\ 0 & 0 & 0 & 0 & 0 & \Delta_6 + \Delta_1 & g_2\sqrt{2} \\ 0 & 0 & 0 & 0 & 0 & g_2\sqrt{2} & \Delta_6 + \Delta_2 \end{pmatrix}. \quad (2.42)$$

At this point I resorted to using a computer algebra system [80] to do the matrix inversion of A and matrix multiplication to generate the effective Hamiltonian according to Equation (2.8).

$$H_{\text{eff}} = \begin{pmatrix} 0 & -\frac{g_1 g_2 g_3 g_4 g_5 g_6}{\Delta_1 \Delta_2 \Delta_3 \Delta_4 \Delta_5} \\ -\frac{g_1 g_2 g_3 g_4 g_5 g_6}{\Delta_1 \Delta_2 \Delta_3 \Delta_4 \Delta_5} & \Delta_6 - \frac{g_6^2}{\Delta_5} \end{pmatrix}. \quad (2.43)$$

The resonance condition is the difference in the diagonal elements and the effective coupling is the off-diagonal elements,

$$\Delta_{\text{eff}} = \Delta_6 - \frac{g_6^2}{\Delta_5} \quad (2.44)$$

$$g_{\text{eff}} = -\frac{g_1 g_2 g_3 g_4 g_5 g_6}{\Delta_1 \Delta_2 \Delta_3 \Delta_4 \Delta_5}. \quad (2.45)$$

The discrepancy between the effective detuning and Δ_6 is relatively large when compared to the effective coupling constant, highlighting the importance of adiabatic elimination to predict the level shifts. The Jaynes-Cummings coupling constant in a laboratory micromaser is between 10 kHz and 100 kHz [25], and for a well behaved system the detunings should be an order of magnitude greater than a transitional coupling strength, which by Equation (2.45) gives a t of up to a second, beyond the lifetime of a current micromaser cavity which is approximately 0.3 s [25].

The other states of the field that correspond to qubits all lack at least one photon required for a multi-photon resonance, so that the atom is incapable of making any transitions, trapping the system

in its initial state. This satisfies the truth table for the Fredkin gate in Table 2.3 when $g_{\text{eff}}t = \pi/2$,

$$\begin{aligned} |1, 0, 1, a\rangle &\mapsto \cos(g_{\text{eff}}t) |1, 0, 1, a\rangle - i \sin(g_{\text{eff}}t) |1, 1, 0, a\rangle \\ |1, 1, 0, a\rangle &\mapsto \cos(g_{\text{eff}}t) |1, 1, 0, a\rangle - i \sin(g_{\text{eff}}t) |1, 0, 1, a\rangle . \end{aligned} \quad (2.46)$$

Remarkably this evolution is the same in the Schrödinger picture up to a global phase.

2.3.1.3 Effective Three-Level Case

In order to increase the effective coupling constant and decrease the gate time, it was sufficient to allow another resonance in the system. This increases the number of effective states in the system from two to three. It replaces the six photon resonance in the two state case into a pair of three photon transitions. These states are shown in table 2.6. The starting point for this was the full

Qubits	Field Modes	Atom
$ 1, 0, 1\rangle$	$ 1, 0; 0, 1; 1, 0\rangle$	$ a\rangle$
	$ 0, 0; 0, 1; 1, 0\rangle$	$ b\rangle$
	$ 0, 0; 1, 1; 1, 0\rangle$	$ c\rangle$
$ \phi\rangle$	$ 0, 0; 1, 0; 1, 0\rangle$	$ d\rangle$
$ 1, 1, 1\rangle$	$ 1, 0; 1, 0; 1, 0\rangle$	$ e\rangle$
	$ 1, 0; 1, 0; 0, 0\rangle$	$ f\rangle$
$ 1, 1, 0\rangle$	$ 1, 0; 1, 0; 0, 1\rangle$	$ a\rangle$
	$ 0, 0; 1, 0; 0, 1\rangle$	$ b\rangle$
	$ 0, 0; 2, 0; 0, 1\rangle$	$ c\rangle$

Table 2.6: This table contains the same states of the system as in table 2.5. The highlighted states are the states accessible to the effective three level Fredkin gate, which allows the additional state of the system in exchange for a much shortened gate time. $|\phi\rangle$ is a convenient short hand for the intermediate state of the field.

Hamiltonian of the system as given in Equation (2.41). The division of this matrix into matrices H_0 , A and B now requires that the diagonal elements associated the the states $|1, 0, 1, a\rangle$, $|1, 1, 0, a\rangle$ and $|\phi, a\rangle$ are moved to the upper left corner of the Hamiltonian. After this the matrix is split into

the parts

$$H_0 = \begin{pmatrix} 0 & 0 & 0 \\ 0 & \Delta_3 & 0 \\ 0 & 0 & \Delta_6 \end{pmatrix} \quad A = \begin{pmatrix} \Delta_1 & g_2 & 0 & 0 & 0 & 0 \\ g_2 & \Delta_2 & 0 & 0 & 0 & 0 \\ 0 & 0 & \Delta_4 & g_5 & 0 & 0 \\ 0 & 0 & g_5 & \Delta_5 & 0 & 0 \\ 0 & 0 & 0 & 0 & \Delta_6 + \Delta_1 & g_2\sqrt{2} \\ 0 & 0 & 0 & 0 & g_2\sqrt{2} & \Delta_6 + \Delta_2 \end{pmatrix}. \\ B = \begin{pmatrix} g_1 & 0 & 0 & 0 & 0 & 0 \\ 0 & g_3 & g_4 & 0 & 0 & 0 \\ 0 & 0 & 0 & g_6 & g_1 & 0 \end{pmatrix} \quad (2.47)$$

The inversion of A is much simpler than in the effective two level system since it is composed of 2×2 block diagonals. The effective Hamiltonian using these matrices is

$$H_{\text{eff}} \approx \begin{pmatrix} 0 & \frac{g_1 g_2 g_3}{\Delta_1 \Delta_2} & 0 \\ \frac{g_1 g_2 g_3}{\Delta_1 \Delta_2} & \Delta_3 + \frac{g_1^2}{\Delta_1} - \frac{g_3^2}{\Delta_2} - \frac{g_4^2}{\Delta_4} & \frac{g_4 g_5 g_6}{\Delta_4 \Delta_5} \\ 0 & \frac{g_4 g_5 g_6}{\Delta_4 \Delta_5} & \Delta_6 - \frac{g_6^2}{\Delta_5} \end{pmatrix}. \quad (2.48)$$

There are now two resonance conditions. The first is the required multi-photon resonance between the two desired states of the system,

$$\Delta_{\text{eff}} = \Delta_6 - \frac{g_6^2}{\Delta_5}. \quad (2.49)$$

The second condition is enforced to bring the intermediate state of the system into resonance,

$$\Delta_\phi = \Delta_3 + \frac{g_1^2}{\Delta_1} - \frac{g_3^2}{\Delta_2} - \frac{g_4^2}{\Delta_4}. \quad (2.50)$$

When $\Delta_3 \gg \frac{g_4^2}{\Delta_4} + \frac{g_3^2}{\Delta_2} - \frac{g_1^2}{\Delta_1}$ this resonance condition is broken and the effective three state system reduces to the effective two state system. Like the two state case, only two initial states evolve and the others are static. These states evolve according to the equations

$$\begin{aligned} |1, 1, 0, a\rangle \mapsto & [\bar{g}_\beta^2 + \bar{g}_\alpha^2 \cos(g't)] |1, 1, 0, a\rangle \\ & + i\bar{g}_\alpha \sin(g't) |\phi\rangle \\ & + \bar{g}_\alpha \bar{g}_\beta [\cos(g't) - 1] |1, 0, 1, a\rangle, \end{aligned} \quad (2.51)$$

where

$$g_\alpha = \frac{g_1 g_2 g_3}{\Delta_1 \Delta_2}, \quad g_\beta = \frac{g_4 g_5 g_6}{\Delta_4 \Delta_5}, \quad g' = \sqrt{g_\alpha^2 + g_\beta^2}, \quad \bar{g}_{\alpha, \beta} = \frac{g_{\alpha, \beta}}{g'}. \quad (2.52)$$

The effective couplings of the three state system are $g_{\alpha,\beta}$, and $\bar{g}_{\alpha,\beta}$ and g' are for convenience. For complete population transfer $g_\alpha = g_\beta = \sqrt{2}g_{\text{eff}}$, reducing Equation (2.51) to

$$\begin{aligned} |1, 1, 0, a\rangle &\mapsto \cos^2(g_{\text{eff}}t) |1, 1, 0, a\rangle \\ &+ i \frac{1}{\sqrt{2}} \sin(2g_{\text{eff}}t) |\phi\rangle \\ &- \sin^2(g_{\text{eff}}t) |1, 0, 1, a\rangle, \end{aligned} \quad (2.53)$$

and the gate action is completed when $g_{\text{eff}}t = \pi/2$,

$$\begin{aligned} |1, 0, 1, a\rangle &\mapsto -|1, 1, 0, a\rangle \\ |1, 1, 0, a\rangle &\mapsto -|1, 0, 1, a\rangle. \end{aligned} \quad (2.54)$$

There is freedom to adjust g_α and g_β by altering the detunings associated with them. As with the two-level case the states of interest are the same up to a global phase in the Schrödinger picture. This is a powerful tool when working with effective Hamiltonians; in exact Hamiltonians in cavity QED, such as the JCM when applied to the micromaser, there is little freedom to choose the coupling constant, but the effective coupling constants are composed of detuning parameters, which may easily be adjusted, as well as coupling constants which are defined by the properties of the cavity and are difficult to alter after manufacture.

Contrasting this with the effective two level system with similar detunings and coupling constants, the gate time for the effective three level case is on the order of 1000 times faster, well within the lifetime of current micromaser cavities.

2.3.2 Controlled Phase Gate

The controlled phase gate is equivalent under single qubit rotations to the controlled NOT gate, so it may also form a universal set with the single qubit rotation gates, i.e. R_x , R_z and controlled phase are universal for quantum computation.

Input	Output
$ 0, 0\rangle$	$ 0, 0\rangle$
$ 0, 1\rangle$	$ 0, 1\rangle$
$ 1, 0\rangle$	$ 1, 0\rangle$
$ 1, 1\rangle$	$- 1, 1\rangle$

Table 2.7: The truth table for the Controlled Phase gate. This is a two qubit entangling gate, which forms a universal set of logic for quantum computation when complemented with single qubit rotations.

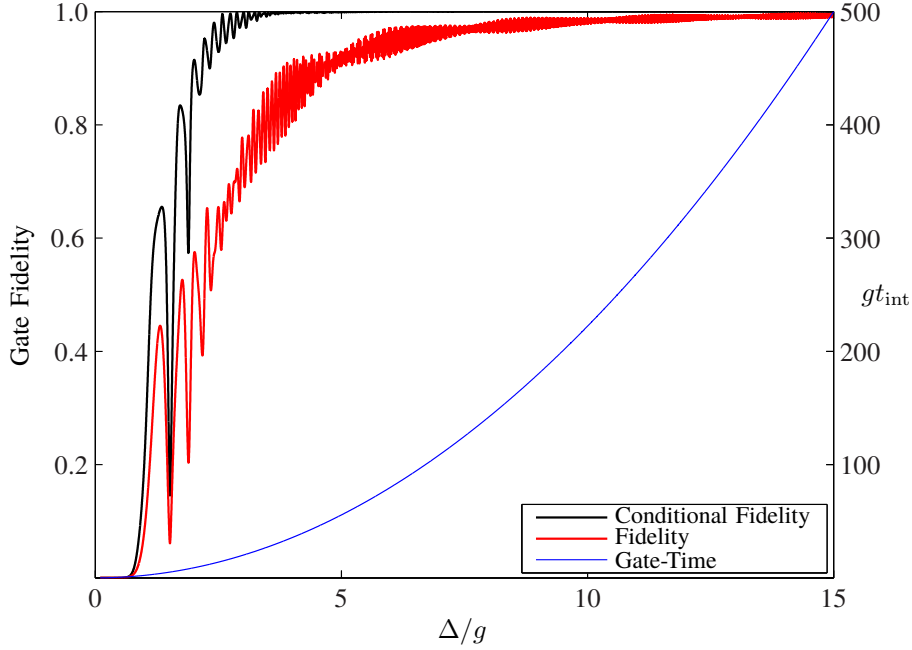


Figure 2.7: This plot demonstrates the fidelity of the numerically simulated Fredkin gate using values from the effective three state model. g is a typical coupling constant and Δ a typical detuning. For this plot all coupling strengths were set to be equal, as were the detunings Δ_1 , Δ_2 , Δ_4 and Δ_5 , however this plot holds for small variations in all these parameters. The values for Δ_3 and Δ_6 were derived from the three level model, Equations (2.49) and (2.50). The conditional fidelity applies if the atom is measured in $|a\rangle$.

This gate is a two photon version of the phase gate. A three level atomic system couples to two modes of the cavity. These modes belong to two different qubits (to be interacted). A photon in mode one corresponds to the first qubit in state $|1\rangle$, and a photon in mode two corresponds to the second qubit in state $|1\rangle$ as well. When both qubits are in the state $|1\rangle$ modes one and two both have a photon and the effective two state system can be excited up to the atomic state $|c\rangle$. Detuning this state by $\Delta_2 \ll \Delta_1$ leads to phase evolution of the system without excitation up to state $|c\rangle$ only when both modes have a photon. In the case of one or both qubits in the state $|0\rangle$, at least one of the two modes has no photon to allow virtual excitation up to level $|c\rangle$, leading to no phase evolution for these terms. As only the two qubit state $|1, 1\rangle$ evolves, a time can be chosen to agree with the truth table for the controlled phase gate in table 2.7.

The Hamiltonian of this system is

$$H = \sum_{\alpha=a,b,c} E_\alpha \hat{\sigma}_{\alpha\alpha} + \sum_{i=1,2} \omega_i \hat{a}_i^\dagger \hat{a}_i + g_1 (\hat{a}_1 \hat{\sigma}_{ba} + \hat{a}_1^\dagger \hat{\sigma}_{ab}) + g_2 (\hat{a}_2 \hat{\sigma}_{cb} + \hat{a}_2^\dagger \hat{\sigma}_{bc}). \quad (2.55)$$

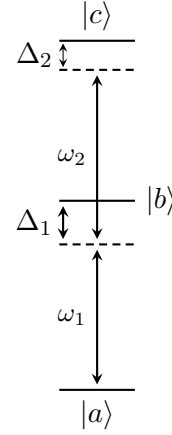


Figure 2.8: Using a ladder of three states, so that the upper and lower are near a multi-photon resonance with modes one and two, and far detuned from the intermediate level, this system enhances the phase evolution when there is a photon in each of the modes. If a photon is missing from one or both of the modes, phase evolution is suppressed. This can be used to construct a controlled phase gate. This is a multi-photon generalisation of the phase gate in Figure 2.1.

Equation (2.20) is used with

$$\Theta = \sum_{\alpha} E_{\alpha} \hat{\sigma}_{\alpha\alpha} + \sum_i (\omega_i + \delta_i) \hat{a}_i^{\dagger} \hat{a}_i + \delta_i \quad (2.56)$$

to transform this Hamiltonian into a more useful form, where $E_b - E_a = \omega_1 + \delta_1$ and $E_c - E_b = \omega_2 + \delta_2$. The detunings Δ_i and δ_i are related by $\Delta_1 = \delta_1$ and $\Delta_2 = \delta_1 + \delta_2$. The initial state of the system is $|1, 1, a\rangle$ and there are two other accessible states of the system, $|0, 1, b\rangle$ and $|0, 0, c\rangle$. The Hamiltonian matrix for this system is

$$H = \begin{pmatrix} 0 & g_1 & 0 \\ g_1 & \Delta_1 & g_2 \\ 0 & g_2 & \Delta_2 \end{pmatrix} \quad (2.57)$$

This matrix is rearranged and split into components for constructing the effective Hamiltonian

$$H_0 = \begin{pmatrix} 0 & 0 \\ 0 & \Delta_2 \end{pmatrix}, \quad A = \Delta_1, \quad B = \begin{pmatrix} g_1 \\ g_2 \end{pmatrix}. \quad (2.58)$$

This leads to the effective Hamiltonian in the limit of $\Delta_1 \gg \Delta_2, g_1, g_2$

$$H_{\text{eff}} = \begin{pmatrix} 0 & -\frac{g_1 g_2}{\Delta_1} \\ -\frac{g_1 g_2}{\Delta_1} & \Delta_2 + \frac{g_1^2 - g_2^2}{\Delta_1} \end{pmatrix}. \quad (2.59)$$

This is the Hamiltonian for the effective two level system, which has an effective coupling constant and effective detuning given by

$$g_{\text{eff}} = -\frac{g_1 g_2}{\Delta_1}, \quad \Delta_{\text{eff}} = \Delta_2 + \frac{g_1^2 - g_2^2}{\Delta_1}. \quad (2.60)$$

In order for the controlled phase gate to work, I repeated the procedure, this time simply reusing the result for the phase gate. In the limit of $\Delta_1 \gg \Delta_2$ and $\Delta_{\text{eff}} \gg g_{\text{eff}}$ this is the detuned limit of the effective two level system, leading to the evolution of the state $|1, 1, a\rangle$

$$|1, 1, a\rangle \mapsto \exp\left(\frac{ig_{\text{eff}}^2}{\Delta_{\text{eff}}}t\right) |1, 1, a\rangle \quad (2.61)$$

Choosing $t = \pi\Delta_{\text{eff}}/g_{\text{eff}}^2$ completes the truth table for the controlled phase gate in table 2.7.

2.4 Implementation

My background in micromaser physics leads me to use the micromaser as a prototype for implementing this form of quantum logic. In this section I list these requirements and justify the micromaser as a good host system for them.

2.4.1 Atoms on Demand

Atoms are required on demand in a particular state. As with the micromaser, Rydberg atoms are appealing due to the strong coupling to microwave cavities and the useful spectrum of energy levels. Multi-step laser excitation systems like those used in the laboratory are suitable for creating many different Rydberg states. Hawri Majeed, Bruno Sanguinetti and Luke Johnson used this fact to resolve the ^{85}Rb $P_{3/2}$ states between $n = 36$ and $n = 63$ [62].

Production of atoms is described in detail in Chapter 4. A Rubidium dispenser emits Rubidium atoms which are collimated. The multi-step laser excitation uses infrared lasers to excite atoms up to a Rydberg state. The velocity of these excited atoms can be controlled by placing the first step laser at an angle, and detuning the laser. Only atoms with a velocity which Doppler shifts the first step light back into resonance with the $5S_{1/2}$ to $5P_{3/2}$ transition are excited up to $5P_{3/2}$; slower atoms will see a frequency lower than the this first step transition and faster atoms with see a higher frequency. The remaining steps, $5P_{3/2}$ to $5D_{5/2}$ and $5D_{5/2}$ to $nP_{3/2}$, are perpendicular and the third step is tuned to choose a particular Rydberg state.

The remaining issue is producing a single atom at a well determined time. Suggestions include using a micromaser as a single atom source, a kind of optical lattice conveyor/accelerator [81] and the use of dipole blockade with a strobed first step laser.

2.4.2 Cavities

This architecture clearly requires elaborate cavities in order to function. Several options are worth pursuing. One possibility is a cavity engineered to have more than one useful mode. This is beyond the scope of current manufacturing techniques, but certainly a possibility in the future. A proof-of-principle would require only two useable modes to test the R_x , R_z and controlled phase set. Another possibility is a network of overlapping open cavities. Again only two cavities are needed to demonstrate the universal set of gates.

An alternative system that may be worth investigating in the future is stripline resonators [82, 83], or any system that can be approximated to the Jaynes-Cummings model extended to multiple modes.

2.5 Summary

I have shown that multi-mode cavities provide an interesting platform for quantum information processing. At present it is not possible to realise a large scale machine based upon it, but it is my hope that this work will become useful in the future as cavity manufacture becomes more advanced. The next steps for multi-mode quantum optical logic are a study of the dissipative dynamics of the system due to a leaky cavity by using a master equation. Another possible extension is to consider a pair of field modes as a *qudit* using more than just single excitations of field modes, as shown in Figure 2.2, rather than simply a qubit.

Chapter 3

Atom-Atom Entanglement

It is still possible that quantum theory does not absolutely guarantee that gravity has to be quantized. ...In this spirit I would like to suggest that it is possible that quantum mechanics fails at large distances and for large objects. Now, mind you, I do not say that I think that quantum mechanics does fail at large distances, I only say that it is not inconsistent with what we know.

Feynman Lectures on Gravitation [52]

Richard Feynman

Cavity QED schemes offer a broad range of methods for producing entangled states of atoms. This could be particularly useful for quantum information processing and even testing quantum gravity as shown in Section 3.5. One state of particular interest is the GHZ state. It can be used to test quantum mechanics at a fundamental level, by testing a Mermin-Klyshko inequality for nonlocality [32], and for quantum information purposes. In this chapter I show a method for producing entangled states. I start off with a phase gate for atoms, and use this to build up GHZ states by chaining phase gates together. I also demonstrate how this phase gate generalises to an interaction that can produce N -atom W states [77].

I came to view this as almost the opposite of what I did in Chapter 2. In that chapter, I specifically avoided storing any information on an atom by using dispersive interactions. In this chapter I use dispersive interactions again, but this time to avoid storing information in the cavity field. In addition, the work in this chapter leads up to a possible architecture for a graph state quantum computer [33, 34], which uses a multipartite entangled resource and measurements to drive the computation. In contrast the work in Chapter 2 uses the unitary model of quantum computation so that logic gates are reversible and measurements are usually used for readout rather than processing.

3.1 Controlled Phase Gates for Atoms

Zheng and Guo proposed a scheme using a detuned two atom Tavis-Cummings model to perform a controlled phase interaction between two atoms passing through a cavity [35]. Haroche *et al.* tested this interaction by using it to produce and test for Einstein-Podolsky-Rosen (EPR) states, but in a suboptimal system with one atom travelling colinear to the other and at a greater velocity [36]. The results from this experiment was consistent with the prediction for Zheng and Guo. Recent advances in micromaser technology and a purpose built system will provide a complete controlled phase gate to good fidelity, which we plan to produce in the near future in the laboratory at the University of Leeds. The paper by Zheng and Guo was published in Physical Review Letters, and the four page limitation has led to gaps in the derivation. In addition it was at a time when the controlled NOT gate was considered more important than the controlled phase gate, so they included rotations to transform the system into a controlled NOT which detracted from the main derivation. In Section 3.1.1 I give a more complete derivation than that available in the paper by Zheng and Guo [35].

3.1.1 The Tavis-Cummings Hamiltonian

The Tavis-Cummings model generalises the Jaynes-Cummings model to the case of a single mode field interacting with N atoms. The derivation is very similar to that of the Jaynes-Cummings model, and eventually leads to the Tavis-Cummings Hamiltonian in the interaction picture [4]

$$H_{\text{TC}} = \sum_{j=1}^N \left[\frac{\hbar\Delta}{2} \hat{\sigma}_3^{(j)} - i\hbar g \left(\hat{\sigma}_{(j)}^+ \hat{a} - \hat{\sigma}_{(j)}^- \hat{a}^\dagger \right) \right]. \quad (3.1)$$

This follows the same conventions I used to derive the Jaynes-Cummings model in Chapter 1, with the addition of subscripts and superscripts (j) to denote the j -th atom. It shares with the Jaynes-Cummings Hamiltonian one important feature; it preserves the number of excitations in the system. In the dispersive regime the detuning is large, so the movement of excitations from the atoms to the field, and vice versa, is not energy conserving and is suppressed. This does not limit the movement of excitation between atoms via virtual excitation of the field, as this conserves energy. Intuitively this provides an interesting way of interacting atoms together in a field without entangling them with it.

Zheng and Guo use the limit of large detuning to produce an effective Hamiltonian. By doing this they remove the field as a degree of freedom, eliminating atom-field entanglement, but allowing virtual excitation of the field to pass excitations between atoms. Zheng and Guo use two atoms so $N = 2$. Adiabatic elimination [29] can be used to derive an effective Hamiltonian from the original if some eigenvalues are very large (these correspond to the detuned states of the system when an excitation from an atom has been transferred to the field). The theory of effective Hamiltonians

is explored in greater depth in Chapter 2. A more rigorous alternative derivation can be found in appendix A.1. The essential part is the equation

$$H_{\text{eff}} = H_0 - B \cdot A^{-1} \cdot B^\dagger. \quad (3.2)$$

Projection operators are used to produce H_0 , A and B . H_0 corresponds to the states of interest, i.e. those that are not detuned. A corresponds to the rest of the states of the system, and B is (viewed in a block-wise matrix) the upper right matrix. If the states of the system H_0 are gathered to the top right of the Hamiltonian, then the block-wise matrix for the Hamiltonian is given as

$$H = \begin{pmatrix} H_0 & B \\ B^\dagger & A \end{pmatrix} \quad (3.3)$$

The only assumption made is that the eigenvalues of A are large (i.e. large detuning for particular states). If we can assemble any Hamiltonian in this way then an effective Hamiltonian may be produced to simplify modelling with good approximation. For the purposes of the Zheng and Guo controlled phase gate only the cases of two ground state atoms entering, or a ground and an excited state entering need be considered. One would expect to need the case of two excited atoms, but an auxiliary state will be used instead, which is so far from resonance with the field that it may be assumed to be not present, reducing the system to a detuned Jaynes-Cummings model. A level diagram is provided in Figure 3.1. This case will be handled later. First I consider the two atoms in

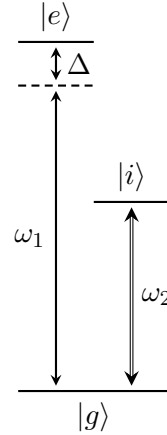


Figure 3.1: This level scheme shows the three levels used for atom-atom entanglement with the Zheng and Guo interaction. The cavity field mode has a frequency of ω_1 , which is detuned from resonance with the $|e\rangle$ to $|g\rangle$ transition to provide a dispersive interaction. A classical field can be used to shift the atom from $|g\rangle$ to $|i\rangle$ and back to remove it from interaction with the cavity field. This is used so that at most one atom of the pair is in the excited state.

ground states. This is rather simple, as neither atom has any excitation and the field is not resonant with the atomic transition, so no interaction occurs. When one and only one atom is excited there are several possible states of the system; $|e, g, n\rangle$, $|e, e, n - 1\rangle$, $|g, g, n + 1\rangle$ and $|g, e, n\rangle$. We expect the states $|e, e, n - 1\rangle$ and $|g, g, n + 1\rangle$ to be suppressed due to detuning, so these belong to matrix A and the resonant two to H_0 . Constructing the matrix using the template from Equation (3.3) yields

$$\frac{H}{\hbar} = \begin{pmatrix} 0 & 0 & -ig\sqrt{n+1} & ig\sqrt{n} \\ 0 & 0 & -ig\sqrt{n+1} & ig\sqrt{n} \\ ig\sqrt{n+1} & ig\sqrt{n+1} & -\Delta & 0 \\ -ig\sqrt{n} & -ig\sqrt{n} & 0 & \Delta \end{pmatrix} = \frac{1}{\hbar} \begin{pmatrix} H_0 & B \\ B^\dagger & A \end{pmatrix}, \quad (3.4)$$

where $|\Psi\rangle$ is in the order $(|e, g, n\rangle, |g, e, n\rangle, |g, g, n + 1\rangle, |e, e, n - 1\rangle)^T$. By Equation (3.2) this reduces to the effective Hamiltonian,

$$\begin{aligned} H_{\text{eff}} &= -\frac{\hbar g^2}{\Delta} \begin{pmatrix} 1 & 1 \\ 1 & 1 \end{pmatrix} \\ &= -\frac{\hbar g^2}{\Delta} (\hat{\sigma}_{eg,eg} + \hat{\sigma}_{ge,ge} + \hat{\sigma}_{eg,ge} + \hat{\sigma}_{ge,eg}) . \end{aligned} \quad (3.5)$$

Solving the Schrödinger equation for this produces time dependent evolution. When we make the mapping $|e\rangle \mapsto |1\rangle$ and $|g\rangle \mapsto |0\rangle$, the substitution $\lambda = g^2/\Delta$ and a transformation back to the Schrödinger picture, the time evolution is

$$\begin{aligned} |1, 0, n\rangle &\mapsto e^{i(\lambda-\omega_n)t} [\cos(\lambda t) |1, 0, n\rangle + i \sin(\lambda t) |0, 1, n\rangle] \\ |0, 1, n\rangle &\mapsto e^{i(\lambda-\omega_n)t} [\cos(\lambda t) |0, 1, n\rangle + i \sin(\lambda t) |1, 0, n\rangle] . \end{aligned} \quad (3.6)$$

This seems to be a different approach to that taken by Zheng and Guo. The results are consistent though, and my familiarity with effective Hamiltonians means that I favour this method. A more rigorous version can be found in Appendix A. These equations are useful for $\lambda t = \pi$ and $n = 0$, which returns the state of the system unchanged. When $n = 0$ the cavity must be in the vacuum state, which may be achieved by cooling. The importance of this is not seen by these equations due to the interaction picture, but a general state of the field will lead to a phase spread in the gate. The cavity is in a thermal state, and the only state for which the thermal state and number states converge is the $n = 0$ state. This eliminates the spread in phase.

I now consider the state $|0, 0\rangle$, which corresponds to the system initially in the state $|g, g, 0\rangle$. No excitations are present in this state of the system, so there is no phase evolution.

$$|g, g, 0\rangle \mapsto |g, g, 0\rangle \quad (3.7)$$

So far we have a working scheme that returns $|0, 0\rangle$, $|0, 1\rangle$ and $|1, 0\rangle$ unchanged. The remaining state to deal with is $|1, 1\rangle$. For this Zheng and Guo put a rotation zone before and after the cavity for one of the atomic beams. This rotates the atoms in the excited state in one stream only to $|i\rangle$, and back again on the other side of the cavity. This breaks part of the symmetry and changes one of the two equations above. This will change one initial state to look like $|g, i\rangle$, which like $|g, g\rangle$ will not interact with the field, retaining the parts already solved. The final possible state to input is altered from $|e, e\rangle$ to $|e, i\rangle$ before interaction, which is effectively a detuned Jaynes-Cummings model on the first atom as the second is so far from resonance. It is simple to derive the detuned JCM from the method used above, resulting in the evolution

$$\begin{aligned} |e, i, n\rangle &\mapsto e^{-i\lambda(n+1)t} |e, i, n\rangle \\ |g, i, n\rangle &\mapsto e^{-i\lambda nt} |g, i, n\rangle \end{aligned} \quad (3.8)$$

Selecting $\lambda t = \pi$ and $n = 0$ reduces this to a parity operation $|e, i\rangle \mapsto -|e, i\rangle$ and $|g, i\rangle \mapsto |g, i\rangle$. The truth table for before and after the interaction inclusive of all rotations is given by table 3.1.

Input	Output
$ 0, 0\rangle$	$ 0, 0\rangle$
$ 0, 1\rangle$	$ 0, 1\rangle$
$ 1, 0\rangle$	$ 1, 0\rangle$
$ 1, 1\rangle$	$- 1, 1\rangle$

Table 3.1: The truth table for the collisional phase gate introduced in [35]. This is inclusive of a pair of rotations performed before and after the cavity on one beam. I have used the mapping $|e\rangle \mapsto |1\rangle$ and $|g\rangle \mapsto |0\rangle$.

The physical realisation of this gate is rather simple in principle. The cavity is a pair of mirrors forming a high-Q resonator in the microwave regime, near 21.456GHz. The atomic transition can be chosen to be the same as that used by the micromaser, between 63P and 61D states of rubidium 85. The rotation zones may be microwave waveguide with microwaves of an appropriate frequency. Atoms pass through a hole in the side of the guide which is just a tube of copper of rectangular cross section. Alternatively a lower Q cavity may be used for each rotation zone. A diagram of the arrangement for the phase gate is in Figure 3.2.

¹Dr. Martin Jones insisted that I include $|t, o, n, i, c\rangle$.

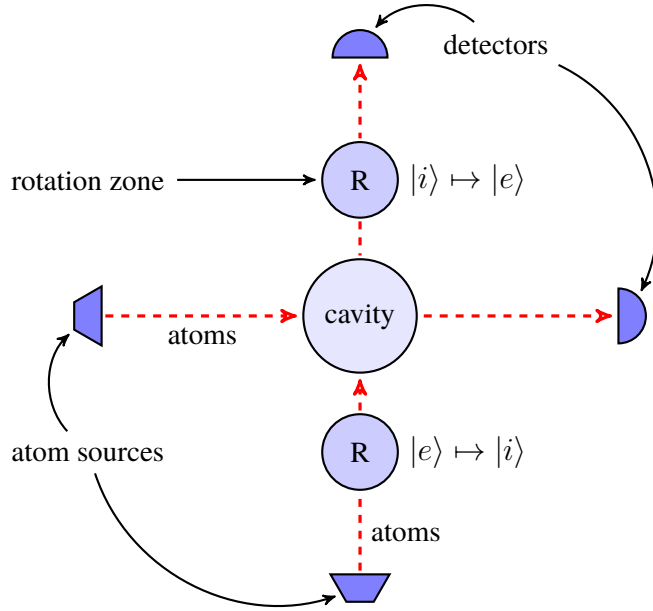


Figure 3.2: A diagram demonstrating the collisional phase gate with two atoms as the qubits. The atom sources produce synchronized atoms with equal speed. The dashed arrows indicate the trajectory of individual atoms, the solid arrows are used to label components. This arrangement is a controlled phase gate on atoms input in $(\alpha_1 |g\rangle + \beta_1 |e\rangle) \otimes (\alpha_2 |g\rangle + \beta_2 |e\rangle)$ with arbitrary $\alpha_{1,2}$ and $\beta_{1,2}$.

3.2 Making Greenberger-Horne-Zeilinger States

In this section I show how the Zheng and Guo collisional phase gate can be used to construct N atom GHZ states [37]. The N atom GHZ state is defined as [57]

$$|\text{GHZ}_N\rangle = \frac{|g\rangle^{\otimes N} + |e\rangle^{\otimes N}}{\sqrt{2}} \quad (3.9)$$

This method was developed for a paper I wrote entitled ‘*Dephasing of entangled atoms as an improved test of quantum gravity*’ [27].

Using one cavity and changing the interaction time so that $\lambda t = \pi/4$, two atoms may be interacted to produce an EPR state [38]. This may be done by removing the rotation zones in Figure 3.2 and sending in one atom in $|e\rangle$ and the other in $|g\rangle$ so that Equations (3.6) are sufficient to describe the interaction, resulting in the state $(|eg\rangle - |ge\rangle)/\sqrt{2}$.

Returning to the original interaction time $\lambda t = \pi$ and by fixing the system so that only atoms in the state $|+\rangle = (|g\rangle + |e\rangle)/\sqrt{2}$ enter, the result of the interaction with an additional rotation is the Bell state $(|gg\rangle + |ee\rangle)/\sqrt{2}$. This arrangement is shown in Figure 3.3. In the N atom generalisation of a GHZ state in Equation (3.9) this produces the $N = 2$ state, one of the Bell states.

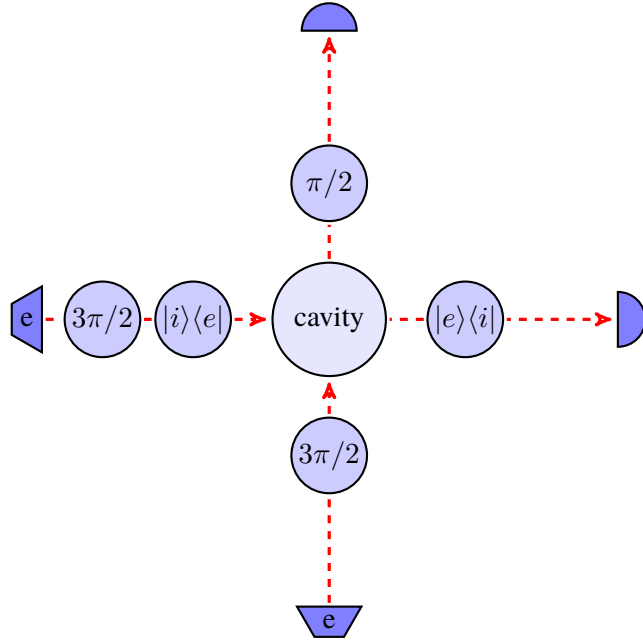


Figure 3.3: This diagram shows a more specific arrangement than the simple phase gate in Figure 3.2. Atoms are produced in the excited state by the sources and are rotated into the state $|+\rangle = (|g\rangle + |e\rangle)/\sqrt{2}$. The phase gate is then applied to these pairs of $|+\rangle$ state atoms. After the final rotation on each atom this produces an EPR state to be measured. The smaller circles here represent the rotation zones shown in Figure 3.2.

This system can be adapted to make larger GHZ states. By considering the graph state notation for an N -atom GHZ state the route to doing this becomes more obvious. This graph consists of a single qubit in the centre, with edges (controlled phase gates) to the rest of the qubits². This is shown in Figure 3.4. It is clear from this that one atom needs to interact with the rest of the atoms, but none of the other atoms need interact with each other. What the graph does not make clear is what single qubit rotations must be applied, since the graph depicts all states with equivalent entanglement to the GHZ state. This was simple enough to guess based upon the existing two atom case. The process for the atom travelling vertically in Figure 3.3 is simply repeated before the final rotation of the horizontally travelling atom. This is shown in Figure 3.5. The equivalent circuit for the state produced with the arrangement in Figure 3.5 is shown in Figure 3.6.

3.3 Making W States

The EPR state can be viewed as the degenerate case of an N -atom GHZ state and an N -atom W state containing a single one and $(N - 1)$ zeros, although it is not commonly thought of in this

²That is not to say that a graph describing a particular state is unique. The ‘central’ atom may obviously be permuted and other graphs that have a different number of edges may also be possible [39].

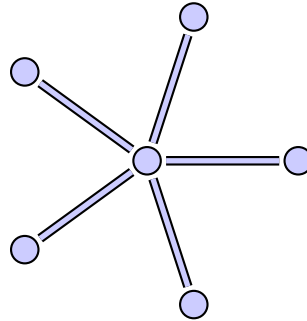


Figure 3.4: This is the graph representation of an $N = 6$ GHZ state. Each vertex represents a qubit initially in the $|+\rangle$ state, and each edge is a controlled phase gate between qubits. The order in which the controlled phase gates are performed does not matter since they commute. Additional single qubit rotations after entanglement are not described in this notation.

way. This hints at the possibility of using the dispersive interaction that Zheng and Guo used [35] with more atoms to form a W state. By sending $(N - 1)$ atoms into a cavity in the ground state with one atom in the excited state, a superposition of the excitation being present in every possible configuration of the N qubits could be seen after the interaction. This was my initial guess based upon conservation of energy.

Learning from the two atom case, I assumed that I had to work with an $n = 0$ field for W state production in this manner. In the interaction picture the Tavis-Cummings Hamiltonian (3.1) leads to the Hamiltonian matrix

$$H = \begin{pmatrix} 0 & 0 & \dots & 0 & -ig \\ 0 & 0 & \dots & 0 & -ig \\ \vdots & \vdots & \ddots & \vdots & \vdots \\ 0 & 0 & \dots & 0 & -ig \\ ig & ig & \dots & ig & -\Delta \end{pmatrix} \quad (3.10)$$

where the lower right corner corresponds to the state of the system with $n = 1$ and all ground state atoms, which is to be eliminated. Adiabatic elimination is trivial for this system³ and results in the effective Hamiltonian

$$H_{\text{eff}} = \frac{g^2}{\Delta} \begin{pmatrix} 1 & 1 & \dots & 1 \\ 1 & 1 & \dots & 1 \\ \vdots & \vdots & \ddots & \vdots \\ 1 & 1 & \dots & 1 \end{pmatrix} \quad (3.11)$$

where the matrix is of size $(N - 1) \times (N - 1)$. If the system starts in the state $|e, g, \dots, g\rangle$ then it

³I choose $A = -\Delta$, B is the rightmost column except for the $-\Delta$ term, and H_0 is the remaining $(N - 1) \times (N - 1)$ square matrix of zeros.

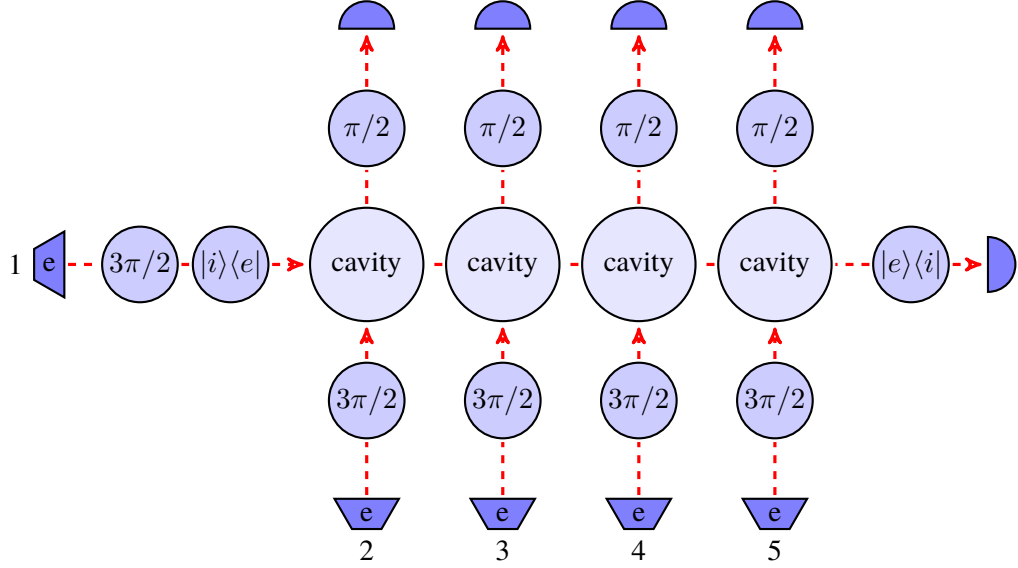


Figure 3.5: This diagram is an extension of Figure 3.3 to a 5-atom GHZ state. This demonstrates that for a GHZ state of size N , $N - 1$ cavities are needed. From the point of view of quantum circuits, five $|+\rangle$ states are manufactured, then one of them has a controlled phase interaction with each of the others in sequence. After a final rotation on each atom (except the first) of $\pi/2$ a GHZ state is made.

will evolve as (neglecting a global phase factor)

$$\begin{aligned} |e\rangle |g\rangle^{\otimes(N-1)} &\mapsto \left[\cos\left(\frac{N\lambda t}{2}\right) - i\frac{N-2}{N} \sin\left(\frac{N\lambda t}{2}\right) \right] |e\rangle |g\rangle^{\otimes N} \\ &\quad + i\frac{2}{N} \sin\left(\frac{N\lambda t}{2}\right) \sum_{M=1}^{N-1} |g\rangle^{\otimes M} |e\rangle |g\rangle^{\otimes(N-M-1)} \end{aligned} \quad (3.12)$$

where $\lambda = g^2/\Delta$. The amplitudes of the first term and the last term need to be equal in magnitude, which occurs at

$$t = \frac{2}{N\lambda} \arctan\left(\frac{N}{\sqrt{4N - N^2}}\right). \quad (3.13)$$

As t must be real, this result is only valid for $N \leq 4$. If $N = 3$, $t = 2\pi/9\lambda$. If $N = 2$ or $N = 4$, $t = \pi/4\lambda$. The $N = 2$ case is of course the EPR state. I found this a surprising result, but in agreement with numerical simulations. Before looking closely at this method of producing W state, I expected it to work for any number of input atoms, rather than a maximum of four.

In addition to this interaction time the amplitudes of each state need to have the same phase, which is true of this system due to symmetry except for the amplitude of the initial state. The necessary phase adjustment can be done by simply Stark shifting the atom that was initially in the excited state after it exits the cavity. This is a form of phase gate, which is discussed in Section

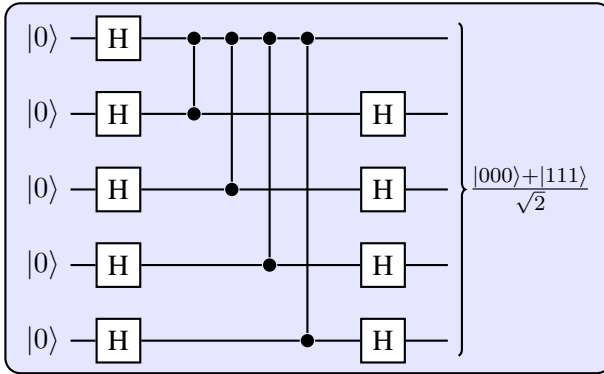


Figure 3.6: This is the equivalent circuit to an experiment involving four cavities and five atomic beams to produce an $N = 5$ GHZ state. $|e\rangle$ and $|g\rangle$ map to $|1\rangle$ and $|0\rangle$ respectively. The Hadamard operations are performed by a single Ramsey field to place atoms in $|g\rangle$ into the state $|e\rangle + |g\rangle / \sqrt{2}$. The four controlled phase gates are performed by the cavities in the experiment.

3.4.2.

3.4 Graph State Quantum Computation

Using atom-atom controlled phase gates it is possible to produce more general entangled states than GHZ states. One elaborate extreme is the production of hexagonal lattice graph states, as shown by Simon Benjamin [40]. As this work is unpublished I will give a brief description in this section.

3.4.1 Graph States

Graph state quantum computation [33] is a relative newcomer to the field of quantum information. Prior to it, quantum algorithms used mainly unitary evolution to do computations. The graph state approach is also known as measurement based quantum computation due to the reliance on projective measurements to drive computations. This approach assumes that a large entangled resource can be manufactured, and then measurements on component qubits in particular bases to encode, drive and read out the computation are used. As the operations are measurements they cannot be undone, in contrast to the unitary approach which is reversible by definition. Thus the original name *one-way quantum computation*.

A recent paper by Blythe and Varcoe [41] proposes a cluster state computer using crossed atomic beams. This can be achieved using arrays of the atom-atom controlled phase gate already described. Provided that timed single atom sources can be produced then this offers a potentially scalable way of producing two dimensional graph states. Time sources of atoms are briefly discussed in Section 2.4.1.

Two arrangements are particularly appealing. One is a minimalist approach, which uses the least resources possible to produce a hexagonal graph state. This is minimalist because each qubit has three edges (in graph notation), the minimum required to form a regular two dimensional lattice. It is important that the lattice is two dimensional, as a one dimensional graph state quantum computer can be efficiently simulated on a classical computer, meaning that there is no ‘quantum speedup’ [34]. An example of a hexagonal graph state is shown in Figure 3.7. The experimental

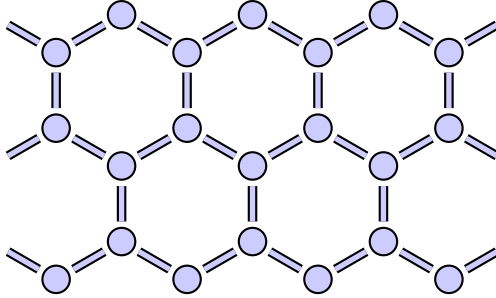


Figure 3.7: The hexagonal lattice graph state is in a sense the minimum useful resource for quantum computation with a quantum speed up. Edges have been added to the left and right sides to indicate that the horizontal extent of the cluster state is arbitrary.

arrangement for a hexagonal graph state is given in Figure 3.8. The enclosed region can be repeated to widen the graph state. One particularly interesting feature of this manner of producing graph states is continuous production. Only a small portion of the graph state exists at any given time, so a computation runs in one direction along the state. An advantage of this is that only the parts of the states being operated on need to exist. The rest of the state can be manufactured *just in time* for the next step in the computation. This avoids decoherence creeping in to computations as much as possible. Another advantage is that the graph state can be infinitely long. If the entangled resource was produced all at once, then the extent must be finite and state is prone to decoherence.

The second arrangement requires more resources, but scales in the same way. This arrangement entangles each atom with four others to produce a square lattice, or cluster state, as first proposed by Raussendorf and Briegel [33]. The apparatus to construct the state is shown in Figure 3.9. Literature on graph state quantum computation centres around the cluster state. Another proposal that uses continuously generated cluster states is the *photonic module* quantum computer presented in a paper by Stephens *et al.* [42].

3.4.2 Rotations on the Bloch Sphere for Atomic Qubits

As the surface of the Bloch sphere represents all pure states of a qubit, only two rotations on the sphere (about different axes) are required to access any qubit state. Conventionally the rotations on the Bloch sphere are R_x , R_y and R_z , which are the rotations about the x , y and z axes of the sphere. It is sufficient to pick rotations about two non-coincident axes on the Bloch sphere to produce any

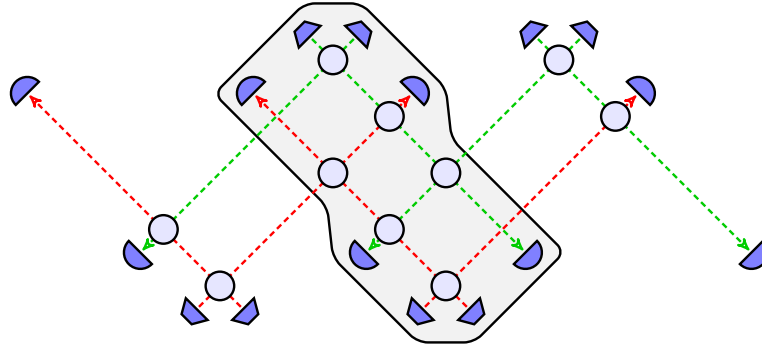


Figure 3.8: This arrangement of cavities constructs a hexagonal graph state. Ovens along the top (bottom) fire simultaneously so that they become entangled where the green (red) dashed lines cross over. The ovens along the top fire out of time with the ovens at the bottom so that atoms from the top and the bottom cross over where the green and red lines cross to become entangled. The enclosed region is the unit cell. Rotation zones are not shown as they are taken to be part of the apparatus of the ovens and the detectors. By inserting multiples of this cell side-by-side in the place of the one in this figure, the size of the graph state will increase.

rotation. In this section I show that the principles behind rotations in x and z have already been experimentally demonstrated and presented in a beautiful paper by Ryabtsev *et al.* [43]. These atomic rotations are designed to operate on Rydberg atoms in atomic beams, making them a perfect complement to the Zheng and Guo collisional phase gate [35] for building graph state quantum computers.

Two processes are used which produce a rotation R_x and a rotation R_z . Firstly, irradiating the atom with resonant electromagnetic radiation will drive the transition between the upper and lower levels in the atom, acting as a rotation about the x -axis of the Bloch sphere. This accounts for one of the two needed rotations, and this is fully described using the semiclassical theory of atom-light interactions. Equation 1.9 in Chapter 1 with a classical electric field can be solved to show that resonant radiation simply drives the population between the upper and lower states sinusoidally. The Hamiltonian for a two level atom in a resonant classical field in the interaction picture is

$$H_I = \frac{\hbar\Omega}{2} (\hat{\sigma}^+ + \hat{\sigma}^-), \quad (3.14)$$

where $\Omega/2$ is the coupling strength of the atom with the field⁴. The amplitudes of the atom given as $\alpha(t)|g\rangle + \beta(t)|e\rangle$ evolve according to the equations

$$\begin{aligned} \alpha(t) &= \alpha_0 \cos(\Omega t/2) - i\beta_0 \sin(\Omega t/2) \\ \beta(t) &= \beta_0 \cos(\Omega t/2) - i\alpha_0 \sin(\Omega t/2), \end{aligned} \quad (3.15)$$

⁴ Ω is the Rabi frequency.

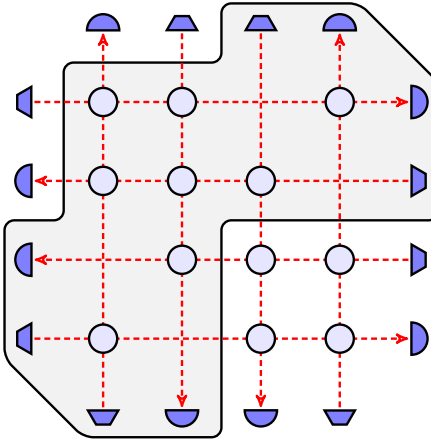


Figure 3.9: This arrangement of cavities constructs a cluster state. Ovens all fire at every time step. The enclosed region is the unit cell. By inserting multiples of this cell diagonally (and reversed to align ovens with detectors) in the place of the one in this Figure, the size of the cluster state will increase. With one this exact arrangement the state produced is a two qubit wide ribbon. This version was developed by Neil Lovett in collaboration with Ben Varcoe and myself.

which is equivalent to R_x . The simplest implementation of a second rotation is by applying an electric field to the atom. This effectively increases the transition energy between the levels of the atom. In the interaction picture this leads to an increased rate of phase evolution compared with an unshifted atom. This additional phase is equivalent to a rotation about the z -axis of the Bloch sphere.. This technique was shown to work by Ryabtsev *et al.* [43]. They applied a resonant microwave pulse to drive the transition between two sodium Rydberg states. This is the same interaction that I detailed above, tuned to place the atom in an equal superposition of the two states. The Stark shift is next applied followed by an identical microwave pulse to the first. The combination of interactions allows Ramsey interferometry of the R_z operation applied by the Stark shift. The measurements in [43] demonstrate that the phase operation R_z is indeed applied and is coherent.

Rydberg S and P states are particularly good to use. P is more susceptible to external fields than S states of the same principal quantum number n , so by applying an electric field to an atomic qubit with a lower level as an S state and a higher level as a P state, the upper level will shift away from the lower level in a predictable way. For Rydberg states of alkali metals the Stark shift varies approximately quadratically with the electric field amplitude.

$$\delta \propto -\alpha E^2, \quad (3.16)$$

where α is the polarizability of a particular state of the atom and E is the amplitude of the electric

field. The polarizability of two states will be different, so the relative phase shift will be given by

$$\Theta = \epsilon(\alpha_g - \alpha_e)E^2, \quad (3.17)$$

where ϵ is a factor related to the pulse shape of the electric field. Applying an electric field for some time t , the phase of the atom in the interaction picture evolves as

$$\alpha|e\rangle + \beta|g\rangle \mapsto e^{-i\Theta t}\alpha|e\rangle + \beta|g\rangle, \quad (3.18)$$

which is a phase shift gate R_z . The factor ϵ is calculated using an integral over the pulse shape of the electric field.

It is important to note that Rydberg atoms have complicated ‘Stark maps’. As the electric field is increased, some energy levels converge and for an adiabatic change in the field there will be avoided crossings. The approximation that the level shifts are quadratic with field is only true for relatively weak fields where avoided crossings do not occur, i.e. below the Inglis-Teller limit [75]. This necessarily means that the field will always be too weak to ionise the Rydberg atoms.

3.5 Probing Quantum Gravity

In a recent meeting at the Rutherford Appleton Laboratory I was involved in a discussion about matter-interferometer experiments that may be sensitive to *conformal fluctuations*; local perturbations in the spacetime metric equal in all directions. In recent papers conformal fluctuations are expected to be a hallmark of the mesoscopic domain of a quantum theory of gravity [53, 55, 56]. The vacuum graviton fluctuations of quantum gravity are coupled to conformal fluctuations that are near the Planck scale, which on the mesoscopic scale leads to anomalous proper times. The authors draw an analogy with Brownian motion, in that the origin of this effect is at a much smaller scale than the measured effect. In an atom interferometer this will lead to a dephasing and reduction in visibility of interference fringes. In this section I demonstrate how GHZ states of atoms provide a more sensitive measurement of dephasing than atom interferometers.

Theories of quantum gravity are not created equal. Each has a unique background parameter λ . This λ is associated with a rate of dephasing. Of course, in the laboratory there are numerous sources of dephasing which are likely to overwhelm the dephasing due to gravity. However, if an experiment is refined to the point where it passes the λ associated with a particular theory of quantum gravity then this theory is effectively ruled out. Interferometric measures of dephasing thus form a small scale laboratory test that rules out theories of gravity. The background parameter is defined and discussed in Section 3.5.2.

3.5.1 Quantum Gravity and Conformal Fluctuations

Work on conformal fluctuations in this context started with a paper by Power and Percival [53]. This was a first step which had some notable flaws, but the key concepts and mathematical foundation was used to update the theory and correct it in a paper by Wang *et al.* [55]. A conformal wave is a fluctuation in the spacetime metric in all directions. In the laboratory this can be considered in the low gravity limit

$$g_{\alpha\beta} = (1 + A)^2 \eta_{\alpha\beta}, \quad (3.19)$$

where g is the metric resulting from the wave, A is the amplitude of the wave and η is the Minkowski metric. This kind of wave was originally chosen because of the relative simplicity of it. Power and Percival went on to consider the effect of quantising conformal waves so that the conformal field is subject to vacuum fluctuations. They showed that the vacuum conformal fluctuations couple to matter. If an atom is split over two paths in an interferometer, then the random interactions with the conformal field will manifest as an anomalous proper time, dephasing the atom and reducing the visibility of interference fringes. It is important to note that the quantisation considered is in the weak field, low velocity limit. In these limits time can be considered separately from space, and gravitational waves can be quantised. This is expected to be a valid approximation at the mesoscopic scale but not the Planck scale, where an actual theory of quantum gravity is required.

Using the dephasing p of a two state system which will be defined in Equation (3.24) with the two states representing the two paths, Power and Percival showed that dephasing due to conformal fluctuations is given by

$$p = \sqrt{\frac{\pi}{2}} \frac{M^2 c^4 A_0^4 T \tau_0}{\hbar^2}, \quad (3.20)$$

where M is the mass of the atom, T is the time the atom travels along the arms of the interferometer, τ_0 is the Planck time and A_0 is the amplitude of the conformal field.

The major criticism of Power and Percival's work is that the conformal field is constrained, and not a good candidate for quantisation. Gravitational waves, in analogy to electromagnetic waves, are the natural candidate for quantisation as they are the only necessary dynamical degree of freedom. Wang developed *conformal geometrodynamics* [54] which would later address this problem [55]. Wang showed that the conformal waves and gravitational waves are bound together by a Hamiltonian constraint,

$$H = \int \left[\mathcal{H}^{(\text{CF})} + \mathcal{H}^{(\text{GW})} \right] d^3x, \quad (3.21)$$

where $\mathcal{H}^{(\text{CF})}$ is the Hamiltonian of the conformal field and $\mathcal{H}^{(\text{GW})}$ is the Hamiltonian of the gravitational waves. This equation is in the limit of slow motion and weak field⁵ to decouple the

⁵This is satisfied in the laboratory because the experiment that exploits this is an atom interferometer, in which the atoms are travelling slowly compared to the speed of light in the laboratory frame. The laboratory is also assumed to be a very weak gravitational field, which is the case for on Earth.

spatial components of the Minokowski metric as a Euclidean 3-metric appropriate to a laboratory experiment. In the limit of no gravitational or conformal waves, the vacuum gravitons dominate and amount to a surprisingly large energy. For the range of λ expected, vacuum graviton energy density is expected to be huge; at least 10^{74} kg/m^3 . This is clearly not what we see. Fortunately the derivation of Equation (3.21) showed that the conformal field has a negative energy density. Putting this together, the vacuum graviton energy must be balanced by conformal fluctuations to give $H = 0$. Thus there are expected to be conformal fluctuations, a fact that rescues much of the mathematics and reasoning by Power and Percival [53].

3.5.2 The Background Parameter

The background parameter λ was introduced by Power and Percival [53]. It is a dimensionless scale factor that relates the mesoscopic scale to the Planck scale by the relation

$$l_{\text{cutoff}} = \lambda l_{\text{Planck}} \quad (3.22)$$

This is the cutoff scale at which spacetime starts to look ‘bumpy’. At the Planck scale, it is expected that a theory should generate the background metric without the need for the background metric to be explicitly added, so by the correspondence principle, moving from the classical limit towards the quantum limit should show the beginning of a quantum theory of gravitation as this bumpiness on otherwise flat space (in a laboratory). Of course, it is not known which theory (if any at present) is correct, so λ depends entirely on the theory. This way the length scale of the beginning of the breakdown of general relativity can be used as an indicator of the underlying theory.

The background parameter λ is like a mean free path for an atom. As an atom travels through spacetime, it will be ‘jogged’ by conformal fluctuations, leading to the analogy with Brownian motion. When Brownian motion was first interpreted in 1905 [50] individual atoms were beyond the capability of the instruments of the time to measure, yet the effect atoms had on a much larger mass scale was apparent, and could be used to infer the presence of atoms and molecules. The mesoscopic scale at which dephasing can be measured can be used to indirectly measure physics at the Planck scale. The larger λ is, the longer the atom travels on average between jogs. Each jog leads to a phase shift on the atom, as the conformal fluctuation leads to an anomalous proper time. This effect needs a phase reference to be detected, and this is achieved through atom interferometry which effectively references the atom to itself over two different paths. Over many atoms this effect should average out as a loss of visibility in interference fringes. The updated result in [55] gives the link between the dephasing seen and λ as

$$\lambda = \left(\frac{8c^4\tau_0\sqrt{2\pi^5}}{9\hbar^2} \cdot \frac{M^2T}{p} \right)^{1/3}. \quad (3.23)$$

The background parameter is expected to be in the $10^2 - 10^6$ range [53]. Throughout this literature [53, 55] the experimental result quoted is the high precision Caesium atom interferometry of Peters *et al.* [44], which puts a lower bound on the background parameter of $\lambda > 10^3$. This is already within the range predicted by Bingham [45]. This is promising, as refinements to an interferometer to reduce other environmental causes of dephasing should raise the lower bound even more.

Unfortunately atom interferometers are difficult to refine. The obvious route to improving an experiment is to use more massive particles, such as carbon-60 or larger organic molecules. However these introduce more decoherence channels. For example, for a single atom heat has little meaning, but for a molecule it can have a serious impact on the visibility of interference fringes [46]. The scope for improving matter interferometers to the extent needed to cover the rest of the range of λ is limited.

3.5.3 GHZ Measurements of Dephasing

The type of decoherence due to the gravitational fluctuations discussed in [53, 55, 56] is dephasing. N -qubit GHZ states are known to be extremely sensitive to decoherence, and may be the ideal multipartite state to measure gravitationally induced dephasing [47]. Dephasing of a single two state system is given by

$$\begin{pmatrix} |\alpha|^2 & \alpha\beta^* \\ \alpha^*\beta & |\beta|^2 \end{pmatrix} \rightarrow \begin{pmatrix} |\alpha|^2 & 0 \\ 0 & |\beta|^2 \end{pmatrix} + (1-p) \begin{pmatrix} 0 & \alpha\beta^* \\ \alpha^*\beta & 0 \end{pmatrix} \quad (3.24)$$

where p ranges between zero for completely pure and one for completely dephased. Atom interferometers are sensitive to $(1-p)$ by measuring the visibility of interference fringes. For N parties in a GHZ state, the expectation of the system in the σ_x basis of all parties is related to the expectation of the dephasing. A general measurement basis is defined as [48]

$$B_i = [\sigma_x \cos(\phi_i) + \sigma_y \sin(\phi_i)] \sin(\theta_i) + \sigma_z \cos(\theta_i) . \quad (3.25)$$

The angles θ_i and ϕ_i correspond to angles on the Bloch sphere. The correlation for an N -particle GHZ state with observables in arbitrary bases B_i is

$$\langle B_1 B_2 \dots B_N \rangle = \frac{1 + (-1)^N}{2} \left(\prod_{i=1}^N \cos(\theta_i) \right) + (1-p)^N \cos \left(\sum_{i=1}^N \phi_i \right) \left(\prod_{i=1}^N \sin(\theta_i) \right) . \quad (3.26)$$

If the basis angles for all particles in the GHZ state are set to $\theta = \pi/4$ and $\phi = 0$ then this equation reduces to

$$\langle \sigma_x^{\otimes N} \rangle = (1-p)^N . \quad (3.27)$$

This demonstrates that the measurement of the correlation of the atoms comprising the GHZ state is more sensitive to dephasing than the measurement of any one atom alone. If this measurement is close to unity, then this can be approximated with the binomial expansion

$$\langle \sigma_x^{\otimes N} \rangle \approx 1 - Np, \quad (3.28)$$

so this measure is at least N times more sensitive than the corresponding atom interferometer. Using this it may be possible to produce an enhanced test of quantum gravity using the same micromaser technology that can produce GHZ states.

3.5.4 Augmented Tests with GHZ States

After some thought about gravitationally induced dephasing I surmised that it should also apply to distributed entangled states of atoms. The jump in logic here is from using an atom in a positional superposition as applies to the atom interferometry approach to using an atom in a superposition of electronic states. The first instinct is a reflex. The atom is in the same position whatever the electronic state. This is not true however, as electronic states of Rydberg atoms can have very different wavefunctions. It should be noted that this is an experiment on the electronic states of atoms, so the mass that must be considered is the mass of an electron which reduces the effectiveness of the interferometer. However, the scaling may be better than atom interferometers as I will show in Equation (3.30).

Plugging the dephasing of a GHZ state into Equation (3.23) is a naïve approach, but a reasonable first attempt at showing how micromaser technology may be used to measure quantum gravity. This is currently available as a preprint and has been submitted for publication [27]. The resulting equation is

$$\lambda = \left(\frac{8c^4\tau_0\sqrt{2\pi^5}}{9\hbar^2} \cdot \frac{M^2T}{1 - \langle \sigma_x^{\otimes N} \rangle^{1/N}} \right)^{1/3}. \quad (3.29)$$

This is an exciting result. It shows that by using GHZ states there is another free parameter to improve the experiment, escaping the limitations of atom interferometry. If Equation (3.28) is substituted in instead for the case of measurements close to unity, an Equation which is simpler to interpret is derived

$$\lambda \approx \left(\frac{8c^4\tau_0\sqrt{2\pi^5}}{9\hbar^2} \cdot \frac{NM^2T}{1 - \langle \sigma_x^{\otimes N} \rangle} \right)^{1/3}. \quad (3.30)$$

This equation shows that N does not scale as well as mass *in principle*. However, as I have already noted, mass is a difficult quantity to increase and making the jump to molecules allows other dephasing channels. The number of particles may be more practical to increase.

3.5.5 Discussion

If a very large GHZ state is considered, then from Equation (3.27) I assume that the dephasing becomes extremely fast. This offers a possible explanation for the emergence of the classical world from the quantum world. It is intriguing that quantum gravity may simply rule out the possibility of very large long lived entangled states due to dephasing. This may be an issue for quantum computers in the future. Some quantum computer architectures may rely on very large entangled states of massive particles to operate. Gravitational dephasing may mean that architectures have to be optimised to produce entanglement just-in-time such as the machine in Section 3.4.1. This effect is only predicted for GHZ states as the dephasing of a GHZ state as given in [48] does not generalise to other types of entangled state.

It is fairly simple to show that for an N party W state the dephasing of each atom enters the off-diagonal elements of the density matrix as a factor of $(1-p)^2$, for any value of N . This indicates no gain in sensitivity for W states. For a GHZ state this factor is $(1-p)^N$, leading to the chosen measure which appears to be maximally sensitive.

3.5.6 Alternatives

Another option for an enhanced measure of gravitational dephasing I have speculated is using NOON states of atoms in optical lattice where a NOON state is defined as [49]

$$|\psi_{\text{NOON}}\rangle = |N, 0\rangle + e^{iN\theta} |0, N\rangle \quad (3.31)$$

where $|N, 0\rangle$ is N atoms in one position and $|0, N\rangle$ another, i.e. two different wells in an optical lattice. This is essentially a quantum metrology experiment.

In this type of experiment the atoms are in a spatial superposition. This makes it directly compatible with the work of Wang *et al.* [55] with no modification. Another positive point is that this a NOON state is effectively a single particle with N times the mass of a single atom.

Atoms are loaded into a lattice potential. The potential barrier between this lattice point and a neighbouring one is lowered, producing a NOON state at the two lattice points and raised to preserve it [51]. After some time to evolve and interact with the conformal field the barrier is lowered again and atoms measured on either side. If perfect coherence is maintained all atoms should be measured in one potential well. If there is some dephasing then atoms will be measured on either side. Equation (3.23) in this situation is changed to include the factor of N .

$$\lambda = \left(\frac{8c^4 \tau_0 \sqrt{2\pi^5}}{9\hbar^2} \cdot \frac{(NM)^2 T}{p} \right)^{1/3}. \quad (3.32)$$

This is clearly an improvement over straightforward atom interferometry and the scheme I presented

for GHZ states. Sadly this idea is not yet mature enough to be properly presented in this thesis.

Part III

Experiment

Chapter 4

Experimental Set Up

4.1 The Cryostat

As explained in Chapter 1, the maser cavity must be kept cold. This is not only to superconduct to reduce resistive losses to the walls of the cavity, but to reduce the thermal photon count in the cavity field which would affect the dynamics of the system. It is essential that the maser cavity be kept as cold as possible. To that end we decided to use a *dry* helium dilution cryostat. Dry in this instance means that all cryogens are contained in closed cycles, eliminating the need for a helium bath. In principle it should require less maintenance and be able to run continuously. In addition the design of the cryostat allows fast turnaround. The entire chamber and heat shields can be built up in less than an hour by two people.

The machine is a prototype, and had software and hardware faults which we addressed. These include a malfunctioning compressor on the helium dilution cycle which was ultimately replaced for a different model, software upgrades, replacement of the rotary valve component of the pulse tube cryocooler, broken helium lines inside the cryostat which I soldered back together and most recently a broken turbomolecular pump controller for the pump in the helium line. Another problem was a large contamination of the helium cycle with dirty helium. I recently completed the clean of the helium, and the cryostat is ready to run again.

It is important to consider the power of the dilution cycle. At 100 mK the cooling power is rated at 100 μW . Fortunately the only component that needs to be this cold is the cavity and a device to tune it.

Figure 4.1 is a simplified cross-section of the VeriCold helium dilution cryostat that we use. The experimental region is in the large white space in the lower part of the diagram. The white spaces above 4 K are dominated by the pulse tube cooler. In the most modern design I have fed all cables in from the top of the chamber, using each stage to cool the cables in steps. Martin Jones had

already fed in the optical fibres from the top when the system was at Sussex. I fed through electrical cables, and eventually the microwave lines this way.

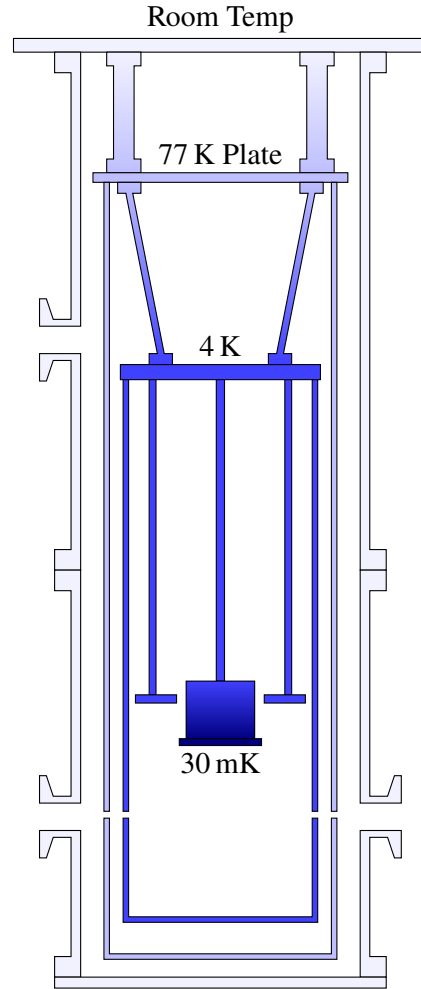


Figure 4.1: A simplified cross-section of the VeriCold helium dilution refrigerator. The cryostat is a single vacuum chamber with ports for feedthroughs at the top, a reconfigurable plate at the bottom and five KF40 ports for connecting vacuum equipment and other apparatus (three shown). The 77 K and 4 K stages are cooled by a pulse tube cryocooler (not shown). The mK stage is cooled using the helium dilution cycle. Most equipment is mounted on rods attached to the bottom of the 4 K stage to hold it in the experimental region (the large white space beneath the mK stage). The cavity is mounted on the mK stage in a similar manner. All wiring (microwave, high voltage, low voltage and fibres) enter from the top and are cooled at each stage. All white areas within the chamber are under vacuum.

I have provided a plot of a model cool-down in Figure 4.2. This plot was produced when the cryostat was first delivered to us at Sussex. Recently I used this as a benchmark to check the health of the cryostat. We have made significant changes to the original device. The changes include a

new rotary valve for the pulse tube cryocooler, new software and a new compressor for the dilution cycle. This prototype version of the cryostat is completely manual, and the software only performs measurements. This prototype lacks the automation of the newer models and there is a complex procedure for turning it on and tending to it. The changes we have made led me to update the instructions for the cryostat. The revised instructions can be found in Appendix C.

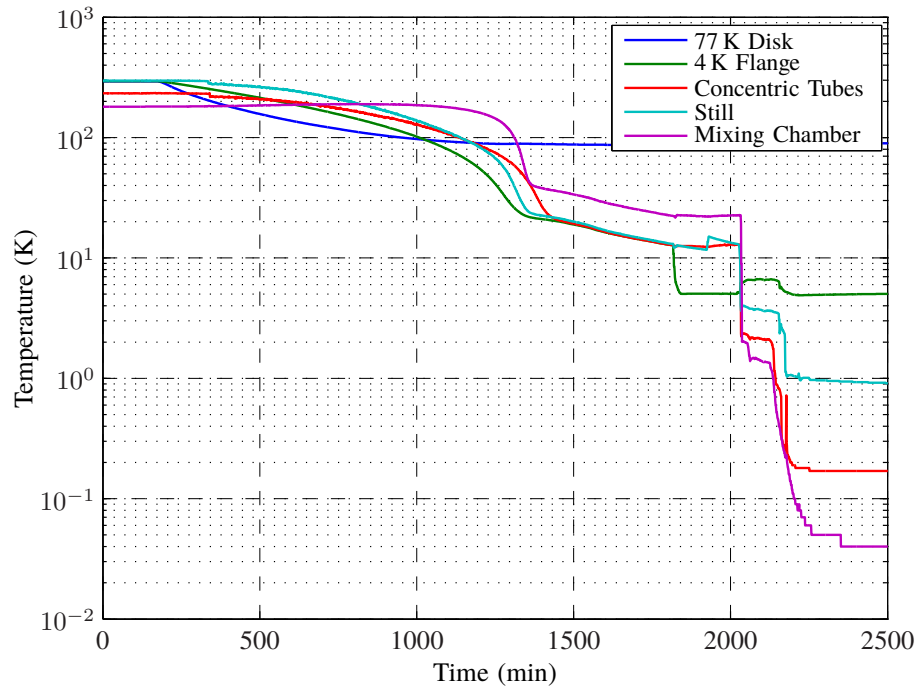


Figure 4.2: This data was taken when the VeriCold cryostat was first delivered to our lab at Sussex University in 2005. For testing purposes it was run with no extra apparatus inside. This is the ideal, unloaded, cooldown of the VeriCold cryostat. At $t \approx 200$ min the pulse-tube cooler was turned on, actively cooling the 77 K and 4 K stages. Shortly after this precooling was turned on to cool mK stage to 4 K. At $t \approx 1700$ min precooling was evacuated, and after evacuation at $t \approx 2000$ min helium was loaded into the mK stage. After a critical amount of ${}^4\text{He}$ is condensed into the mixing chamber the dilution stage begins to cool. The mixing chamber cools the mK stage through the movement of ${}^3\text{He}$ from a concentrated phase to a dilute phase with ${}^4\text{He}$. The concentric tubes act as a heat exchanger, cooling ${}^3\text{He}$ incoming to the mixing chamber with mixture from the chamber before the mixture enters the still, where it is pumped to remove ${}^3\text{He}$ for recirculation.

4.2 Rydberg Atoms

Rydberg states of an atom are attractive for experimental quantum optics for three reasons [58]

- The highly excited electron in a Rydberg state leads to a very large dipole moment, which

couples strongly with the electromagnetic field;

- Some transitions between a Rydberg state and neighbouring Rydberg states are in the K-band¹ of microwaves, on the order of a centimetre in length. This allows cavities with low order modes that are still large enough for long interaction times [58];
- Rydberg atoms have long lifetimes that scale as n^3 [59]. The Paris group uses *circular* Rydberg states [60, 61], that have a very high orbital angular momentum. This high angular momentum increases the lifetime by making the decay path consist of many low energy decays. This scales as n^5 [59].

Whether low- l or circular, the decay time of a Rydberg atom can be long enough that the interaction with a correctly prepared and tuned cavity dominates over decay from either the atom or the cavity field over the time of the interaction. This is known as the strong coupling regime. When the system is strongly coupled, the dynamics become approximately the same as the Jaynes-Cummings model.

4.2.1 Rubidium Dispensers

We use chemically bound rubidium in dispensers [79] to generate the atoms for the experiment. We refer to these simply as *ovens*, although the name is not strictly true. By passing a current between the legs of the dispenser, rubidium is liberated, and can be crudely collimated into a beam by pinholes in the heat shields of the cryostat. This is much safer than handling unbound rubidium and much less apparatus is needed than a traditional oven. This oven is shown in Figure 4.3. The one drawback of these ovens is that they need to be changed at least daily when experiments are running.

An alternative that I have helped to build is a version of a *candlestick oven* [64]. This uses a cylinder heated to about 70 °C to maintain a pool of liquid rubidium. Inside this cylinder is another cylinder. This one is heated from 70 °C up to 200 °C, so that the lower end is submerged in the pool of rubidium at 70 °C. There is an opening in the lower part of this cylinder, exposing the interior to the rubidium pool. The smaller cylinder is stuffed with a ‘wick’. Early designs used gold plated stainless steel to wet the surface of the wick. Later designs, and the one that our oven is being built with, use glass fibre as the wick, which is a less expensive material and simpler to prepare. As the name suggests, this wick draws the liquid rubidium up inside the inner cylinder. There is a pinhole close to the top where the cylinder is hottest, and this is aligned with a pinhole in the outer cylinder. The hot rubidium sprays out of these holes to be collimated into a beam. The outer cylinder has a layer of mesh on the inside to return rubidium which hits it to the pool. The assembly is temperature controlled and heated using thermocouples with the sheath closed and conductors welded at one

¹IEEE K-band is 18 GHz to 27 GHz



Figure 4.3: The rubidium dispenser. This is a very simple device. The two cables seen fed through a KF40 flange. The wires continue as steel rods which are clamped onto the rubidium dispenser at the very tip. When a current is passed across the dispenser rubidium is liberated.

end [64], and there is a water cooled rod which the assembly is mounted to. An image of this oven can be found in Figure 4.4.

The benefit of this method is that it will operate as a stable rubidium source for a very long time, requiring a refill approximately once a year. This design is related to the recirculating oven used at the University of Manchester [84]. The dispensers in contrast need to be replaced after only a day of use. The drawbacks include the need for its own small vacuum chamber to be mounted in, and handling rubidium when the oven needs to be refilled. Earlier models which used gold plated stainless steel wicks often failed to draw rubidium, and required changes of wick [64]. The replacement with glass fibre should be more successful and will be tested soon.

4.2.2 Exciting Rubidium up to Rydberg states

The two Rydberg states of interest to us are $63P_{3/2}$ and $61D_{5/2}$ of $^{85}_{37}\text{Rb}$. The ground state of the Rubidium is raised to $63P_{3/2}$ by a three step laser excitation system. This three step system uses three infrared diode lasers, which are much less expensive to purchase and maintain than the frequency doubled dye laser used in the predecessor to our micromaser [25]. This system was perfected by Hawri Majeed, Luke Johnson, Bruno Sanguinetti and Gary Wilkes working in our lab [62, 63]. The system uses three infrared lasers locked to two rubidium cells. Recently they successfully locked all three steps to cells, which is a difficult problem to solve. Prior to this the third step had to be locked by using an auxiliary atomic beam line and counting Rydberg states using a channel electron multiplier (CEM) with an ionising electric field or by locking to an optical frequency comb.

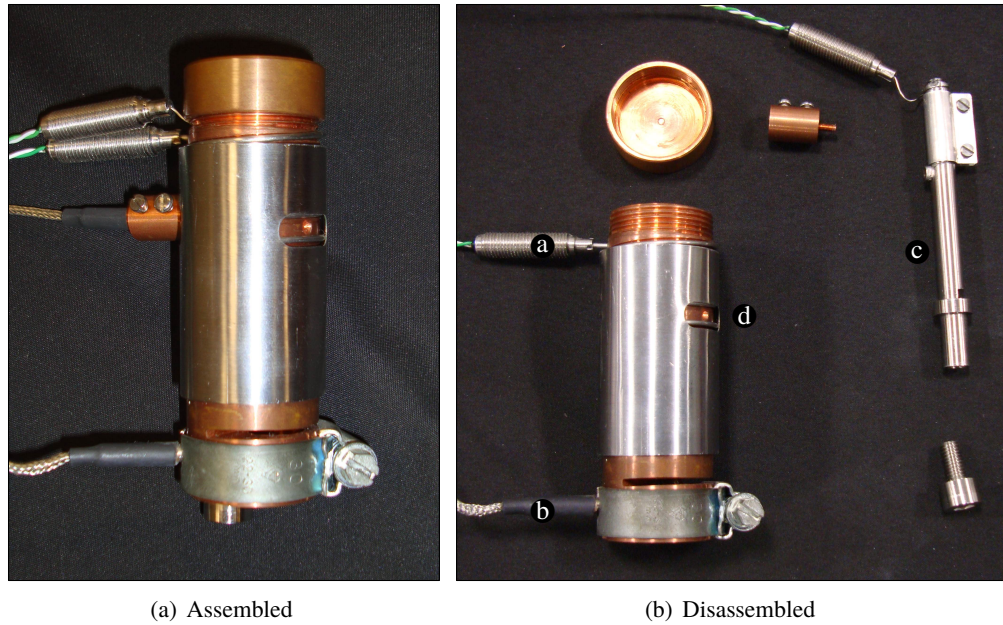


Figure 4.4: The candlestick oven. These diagrams show the components of the oven. On the right, the outside of the oven can be seen with a thermocouple for heating (a) which is coiled under the steel collar. Another thermocouple measures temperature at the base (b). A thinner steel tube (c) slots into the outer tube and is fixed into place with a bolt with a knife edge to seal the assembly. This also has a collar with a thermocouple to heat it. Both heating thermocouples are type-*K* sheathed in stainless steel. Inside will be a ‘wick’ which draws liquid rubidium from the base to the hotter top. The nozzle in the outer cylinder can be clearly seen through a window in the outer collar (d).

4.3 Microwave Transmission

Microwave transmission to and from room temperature to base temperature is important for cavity resonance tests and Ramsey fields needed for the phase sensitive micromaser. The cooling power of the cryostat is limited, so choosing a method for microwave transmission that transmits the minimum power with low attenuation is very important. If heat conduction was not a concern, then rectangular waveguide would be a natural choice. Unfortunately, it is made of copper and the heat conduction would be far too great.

4.3.1 Coaxial Cable

The best choice was Astrolab astro-cobra-flex 31086 [85]. This semi-rigid coaxial cable uses copper clad steel for the core and silver coated copper clad stainless steel for the shield, with a polytetrafluoroethylene (PTFE) insulator which minimises thermal conductivity. The shield is

corrugated so that after cooling and heating many times the insulator will not migrate. The complex design of the cable makes it hard to model, so I calculated thermal conduction using a very rough model of half stainless steel and half copper (rough thermal conductivity of $200 \text{ W K}^{-1} \text{ m}^{-1}$) cable with a cross sectional area of $8.4 \times 10^{-6} \text{ m}^2$ (which is approximately the area of the cable cross-section minus the insulator) and a temperature difference of 300 K. The length of cable needed is approximately 2 m. This is a pessimistic estimate as the corrugations in the shield increase the length of the cable and the thermal conductivity will certainly be lower. The estimate is approximately 250 mW per cable, which is acceptable for mounting to the 4 K stage provided it is also cooled by the 77 K stage first. Subsequent tests of the cryostat showed that the cryostat saw practically no thermal load due to these cables. A cross section of this cable is shown in Figure 4.5.

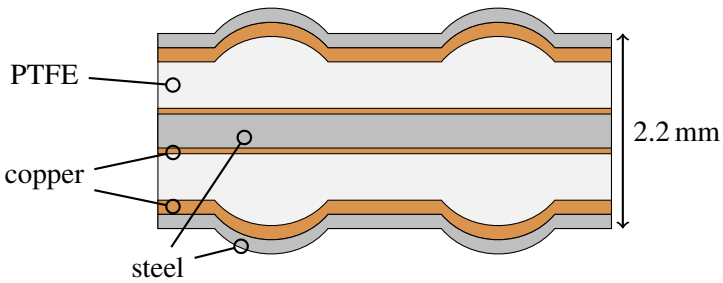


Figure 4.5: A cross section of the astro-cobra-flex cable used for microwave transmission into the cryostat. The lumps are to stop the migration of the PTFE insulator after many cool-downs. The cable is semi-rigid, and can be flexed enough to fix inside the cryostat.

4.3.2 Goubau Lines

Another interesting option is a Goubau line [66–68]. This is a method of projecting a microwave signal as a surface wave over an insulated conducting wire. The wire can be made extremely fine and out of a superconductor, lowering thermal conductivity, as it is not the transmission medium in the usual sense. Using a relatively simple arrangement a microwave signal travelling through a coaxial waveguide can be converted into a surface wave along a single cable, which manifests as compression waves in the electrons of the conductor. The energy of these waves is in the electric and magnetic fields around the conductor. The dielectric coating of the cable draws in the radial extent of the field. This allows for low loss microwave transmission in a manner that minimises the cross sectional area of a conductor. The basic design uses a launcher which is simply a conducting cone attached to the end of a coaxial cable, as shown in Figure 4.6. Where D is the diameter of the aperture and L is side of the cone, $D = 0.6L$ is approximately the right shape, and the side is related to the wavelength of the signal sent by $L < 3\lambda$. The catcher, which puts the signal back into a coaxial cable, is identical to the launcher.

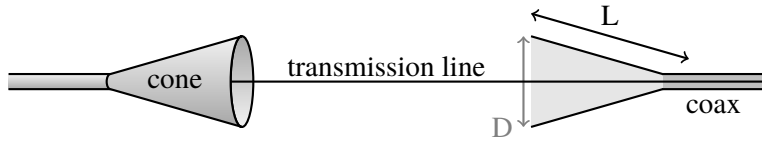


Figure 4.6: This diagram shows the basic design of a Goubau launcher and catcher, with a coaxial cable attached at either end. The launcher and catcher are the same, but the one on the right is a cross section to show how the conductor from the coaxial cable emerges from the insulator of the coax into the catcher cone, where it becomes the transmission line. This line has a thin coating of insulator to lower the radial extent of the surface wave.

The relationship of the cone to the wavelength is the limiting factor of Goubau lines. At the frequencies we use the cone would need to be approximately 4.5 cm wide, which is rather large. It is also unknown how badly radiation would couple into other components in the cryostat, or how close together two Goubau lines could be placed with an acceptable level of crosstalk. However, a short length may be sufficient to allow direct connection between a microwave line and the cavity. At present a piece of waveguide is suspended approximately a millimetre from the cavity to eliminate thermal load from the microwave line.

4.4 High Quality Microwave Resonators

The chosen resonant frequency of our cavities is 21.456 GHz, or $\lambda = 1.40$ cm to coincide with the transition frequency between the $63P_{3/2}$ to $61D_{5/2}$ states of $^{85}_{37}\text{Rb}$. This lies in the IEEE K-Band (18 GHz to 27 GHz) to microwave engineers, and super high frequency (SHF) or centimetre band to the telecommunications industry (3 GHz to 30 GHz or 10 cm to 1 cm).

4.4.1 Geometry

The design we used for micromaser cavities has remained largely unchanged for 20 years and is described in a paper by Klein *et al.* [70]. The design inherits from particle accelerator cavities, and it commonly referred to in that community as a pillbox cavity. Very simply it is modelled on a section of cylindrical waveguide shorted at either end. Particle physicists use electromagnetic cavities to accelerate particles, which requires a non-zero electric field along the axis of the cavity corresponding to a transverse magnetic (TM) mode of the cavity. In contrast micromaser cavities use a transverse electric (TE) mode of the cavity, and these modes have no electric field component in the axis of the cavity. The mode of a cylindrical cavity is characterised using three indices, m , n and p . $2m$ gives the order of rotational symmetry of the field about the axis of the cavity, n is related to the number of nodes between the inner surface of the cavity and the axis, and p is related to the number of nodes along the length of the cavity. The chosen mode for the micromaser cavity

is TE_{121} , as the TE modes have better unloaded quality factors [70], and low values of m , n and p allow better tuning of the cavity by mechanically squeezing it, the apparatus for which is shown in Figure 4.8. The frequency of a cylindrical cavity TE mode in a vacuum is given by [71, p. 42]

$$f_{mnp} = \frac{c}{2\pi} \sqrt{\left(\frac{j'_{mn}}{R}\right)^2 + \left(\frac{p\pi}{L}\right)^2} \quad (4.1)$$

where j'_{mn} is the n^{th} root of the differential of the Bessel function J_m . For the TE_{121} mode $j'_{12} \approx 5.331$ is a good approximation. To optimise the quality, the length of the cavity L should be twice the radius R [71], which leads to a cavity with $L = 2.47$ cm.

4.4.2 Material

4.4.2.1 Copper

The first cavity manufactured by the group is still a good test model. It features coupling holes that are a much lower quality factor than the body, so that measurements on this cavity are easily performed. Copper was chosen for its mechanical properties, which at room temperature are close

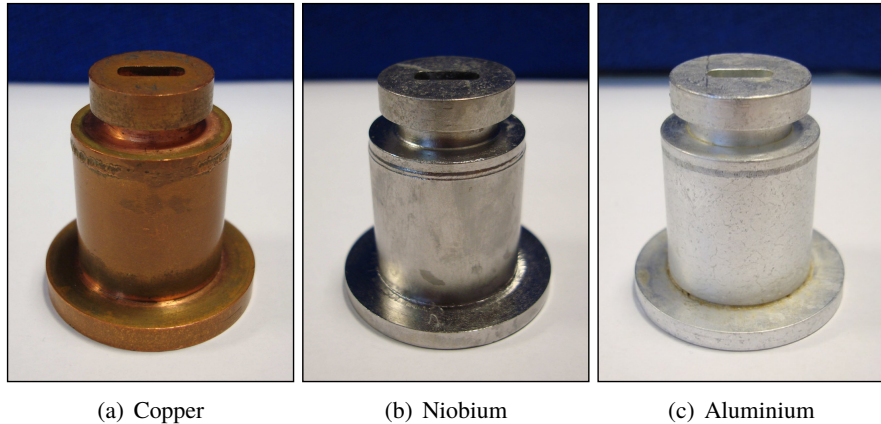


Figure 4.7: Three materials used for test cavities. The copper cavity is good for testing resonance sweeps due to good coupling, and it has similar mechanical properties to niobium in cryogenic conditions which is good for testing the cavity squeezer, shown in Figure 4.8, at room temperature. Some domain boundaries can be seen on the niobium cavity from a failed bake from when the oven was not receiving a large enough flow of coolant. The aluminium cavity is pitted from one student's over-zealous chemical etch. Aluminium superconducts and may provide a more cost effective cavity than niobium. Welds can be seen where the cap of each cavity joins the body near the top. We left one aluminium cavity with three unwelded lids with different Q holes in order to test cavity scans.

to those of niobium at cryogenic temperatures. This similarity allowed us to check the effectiveness

of the cavity squeezer described in section 4.4.3. This cavity is good for trialling new resonance testing experiments and software.

4.4.2.2 Aluminium

Aluminium was chosen as an alternative material to niobium. It is simpler to machine and costs less. Although aluminium has a critical temperature of 1.2 K, which would not have been acceptable in previous micromasers which ran on liquid helium, this is perfectly acceptable for a helium dilution cryostat which easily reaches temperatures below this. Problems with preparation such as bad etches leading to pitting, and failed bakes in the oven stopped tests of an aluminium cavity in the cryostat. Details on cavity preparation were not part of my study and are outside of the scope of this thesis.

4.4.2.3 Niobium

Niobium is the material used in accelerator cavities, which our cavity technology is largely drawn from. This cavity is very close to the original pillbox design by Klein *et al.* [70], and the copper and niobium cavities inherit their geometry from it. Niobium cavities can be produced with impressive quality factors of at least $Q = 10^{11}$ [70].

4.4.2.4 Niobium Coated Copper Open Cavities

A completely different design which we are working on at present uses a copper Fabry-Perot resonator coated with niobium. This design is explored in a paper by Clarke and Rosenberg [72]. It is harder to produce the same quality factors as in a pillbox cavity with an open cavity, but as we intend to use it for dispersive atom-atom interactions (see Chapter 3) the quality factor is less important.

4.4.3 Mount and Cables

The cavity will need tuning into resonance with the atomic transition, so a squeezer is integrated into the cavity mount. Compressing the walls of the cavity will alter the mode shape of the cavity and with it the resonant frequencies. These parts were designed by Bruno Sanguinetti prior to the start of my studentship [65]. The squeezer uses a *squiggle motor*, which moves and rotates a threaded rod up and down using the piezoelectric effect. This pushes on a lever which compresses the cavity to alter the resonant frequencies for tuning [65]. A piezo stack presses on the other side of the cavity for fine tuning. The squeezer is powered using five niobium titanium cables. The mK stage is extremely sensitive to thermal load, so cables needed to be selected carefully. The cables are 100 μm in diameter each, with a thermal conductivity of $0.1 \text{ W K}^{-1} \text{ m}^{-1}$ [73]. Using pessimistic

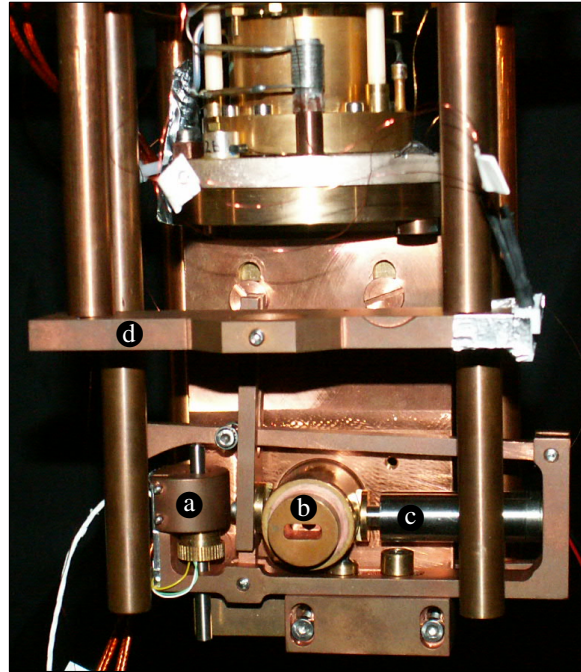


Figure 4.8: The cavity mount and squeezing apparatus. In the foreground (d) is the mount for the detector box suspended from two posts, and immediately behind are two more posts. Behind these the cavity (b) can be seen mounted with the squeezer around it. The squiggle motor is housed in a copper enclosure (a), which pushes up on a lever to compress the wall of the cavity. On the other side of the cavity is a piezo stack for fine tuning (c). The mount of the cavity is attached to the mK stage.

estimates of a gap of 10 K over 2 m these five cables deliver approximately 19 nW, which is well within the tolerance of the dilution stage.

In Figure 4.8 the mount for the cavity can be seen attached to the mK stage. In Figure 4.9 the wiring has been mocked up. The wiring changed little after this image. The 4 K part of the pulse tube cooler can clearly be seen in this diagram, with cables attached to the colder part of it.

4.5 State-selective Detection

As the upper state is closer to ionisation than the lower state, it will ionise first in a ramped electric field. As these Rydberg states are already so excited the electric field to ionise them is about 25 V cm^{-1} . The electron produced by ionising an atom follows field lines into a channel electron multiplier (CEM). These are commonly found in mass spectrometers and consist of a hollow continuous dynode spiral which multiplies an electron or ion through secondary emission up to an avalanche of electrons that can be more easily detected. A second CEM collects electrons from the ionised lower state, which is ionised (on average) after the excited state due to the ramped field.

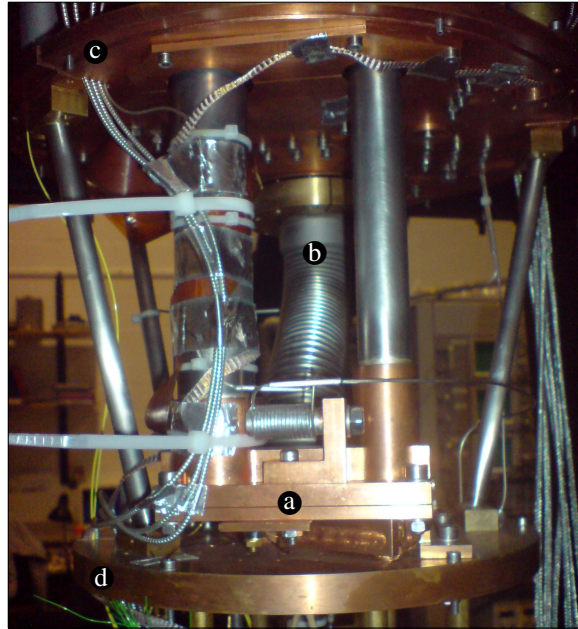


Figure 4.9: Wiring has been mocked up between the 77 K and the 4 K plates (**c** and **d**) before the move to the new lab. In the centre in the foreground, **a**, is the 4 K part of the pulse tube cryocooler. Behind the outlet of the dilution cycle can be seen, **b**. On the far right, some high voltage cables for both CEM can be seen unconnected. These later turned out to be too large a heat load and were removed. Just beneath label **c** the microwave cables can be seen, which pass over the pulse tube cooler before progressing to the 4 K plate. In yellow, optical fibres can also be seen. Running along the 77 K plate is the NbTi woven loom used to power the squiggle motor and field plates of the detector box. Above label **a** a coil can be seen. This cools helium for the precooling and dilution cycles.

The detector box needs two high voltage (for the collector and bias) and one low voltage line (for the cone) per CEM, which introduces a significant heat load on the cryostat. Until recently we had cables that were relatively fine delivering high voltage, but the insulator began to break down so these need replacing. We are now examining the possibility of electron optics to channel the electrons up to a detector box mounted at 70 K. A CEM is not very efficient at very low temperatures, so this alteration would improve efficiency. Other cables are needed to provide voltage for field plates in the detector box. These cables are fed down with the cables for the cavity squeezer in a Nomex woven loom of niobium titanium alloy wire. Figure 4.10 shows the inside of the detector box, with the two CEMs and field plates.

This box was designed by Bruno Sanguinetti and Gary Wilkes. Martin Jones is currently working on an updated version that optimises the field profile. This work can be found in his thesis [75].



Figure 4.10: Interior of the detector box. Two CEM are mounted to a stainless steel plate. The one on the left is intended to detect upper states through field ionisation provided by the copper field plates below. The upper and lower plates provide a voltage, and the two middle plates mask the field to produce a ramp, causing upper states to ionise before lower states. The steel plate is attached to the field plates by MACOR rods. These in turn attach to a copper shell that is grounded and covers the assembly. This shell also allows mounting.

4.6 The Experimental Region

Below the mK stage in the cryostat is where the experiment is mounted. Figure 4.11 is a cross section through the cryostat showing the approximate positioning of the components that make up the micromaser. Figure 4.12 shows all the parts in position, except for the microwave line to the cavity. Most of these components are actually mounted to the 4 K stage. They are a relatively large heat load, and even one of the microwave cables would overwhelm the mK stage. The only components on the mK stage are the cavity and mount with the squeezer, which is powered by superconducting niobium titanium alloy cables, which are very fine to reduce heat load. At room temperature, clamped onto the outside of the cryostat, is the oven which is described in Section 4.2.1. The atomic beam is collimated by the heat shields at 77 K and 4 K. The first component at 4 K encountered by the atoms is the laser excitation region, which is described in Section 4.2.2. The three optical fibres are fed to this component from above, and are cooled by each stage successively. Next are the Ramsey fields. These are made of rectangular copper microwave waveguide, fed from one end by the coaxial cable described in section 4.3.1 and terminated at the other end. I designed the mounting for these. The cavity is between the Ramsey zones, mounted to the mK stage with the squeezer. After the second Ramsey zone is the state selective field ionisation detector. Referring

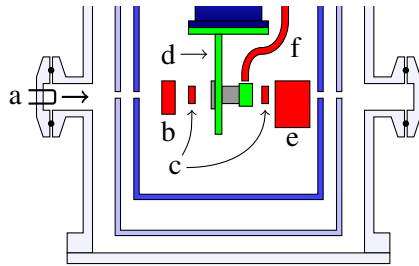


Figure 4.11: The experiment. This diagram neglects the mounts for components except for the cavity. Red parts are anchored to 4 K and green parts (with the grey cavity embedded in them) are anchored to 30 mK. In the order that an atom encounters each component; **a** is the oven, **b** is the laser excitation zone which elevates atoms to a Rydberg state, **c** are microwave waveguides for Ramsey spectroscopy, **d** is the cavity with mount and cap, **e** is the state selective field ionisation detector and **f** is a microwave waveguide for running scans of the cavity.

back to Chapter 1 Figure 1.10 this layout has all the components necessary to be a phase sensitive micromaser.

An image of the cryostat and supporting equipment I have worked with in my time is in Figure 4.13 and specifically the cryostat is shown in Figure 4.14.

4.7 Software

One of my largest contributions to the laboratory is software. Most of the custom software used in the lab has been written by me. Contributions include all of the software for running resonance scans of cavities, most of the software for sweeping the third step laser to find Rydberg states, receiving counts from each CEM and obtaining time of arrival data from Fiberbyte (now ChronoLogic) equipment. The Fiberbyte devices allow for sub-nanosecond timed data acquisition using devices synchronised over universal serial bus (USB) with USB-inSync, a technology which they developed. The Fiberbyte devices will ultimately be used to time pulses and acquire time of arrival data from CEMs. This will also allow us to determine the time resolution of the detector box. I've also written little UNIX utilities to convert data from proprietary formats into files that can be read by data analysis software and our own software. An example of some of the code I have written is shown in Appendix B. Since software in a laboratory is a means to an end, and not intrinsically interesting, I will not dwell on it in this thesis.

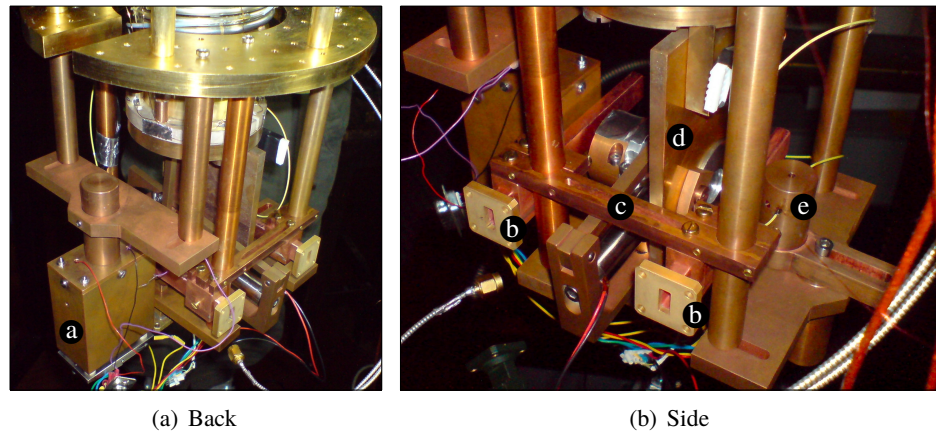


Figure 4.12: The core of the micromaser. At the back the detector box (a) can be seen mounted and inside a copper housing. At the side two lengths of rectangular waveguide (b) can be seen attached to a mount (c) that goes around the cavity mount (d), which can be seen nestled in the centre. On the right hand side of the side view the laser excitation zone (e) can be seen with yellow fibres emerging from it. Alignment of this system can be particularly tricky. An invaluable tool was a surveyors laser. Most of the mounting equipment seen was developed by me. The detector box was developed by Bruno Sanguinetti and Gary Wilkes and laser excitation zone was developed by Martin Jones. The cavity mount and squeezer was developed by Bruno Sanguinetti. All microwave components and wiring (not seen here) were developed by me.

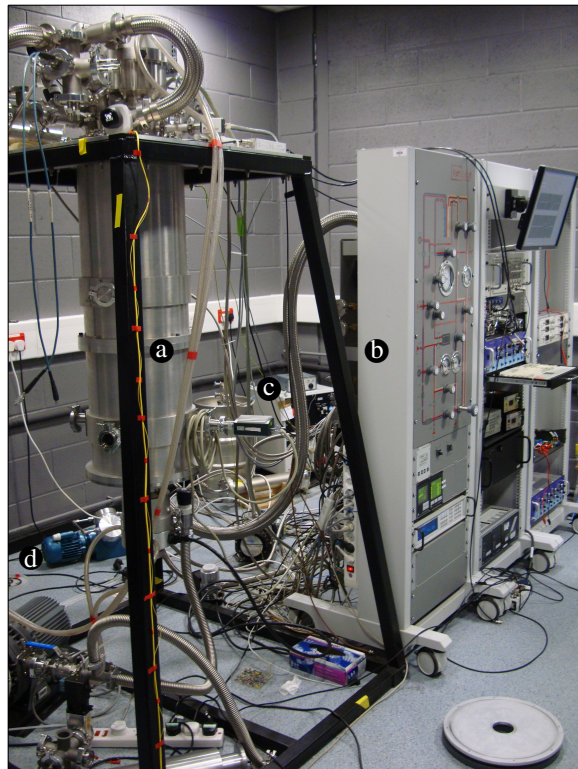


Figure 4.13: This picture shows the cryostat (a) with some support equipment. The closest rack (b) contains control valves, vacuum gauges, pump controllers and temperature measurement equipment for the cryostat. The next rack contains the computer for the experiment, oscilloscopes, some more vacuum controllers and high voltage equipment. The final rack is for the testing of Martin Jones' new detector box. In the corner of the room, obscured by a hose, is the compressor for the pulse tube cryocooler (c). In the lower left of the image is the blue compressor for the dilution cycle (d).



Figure 4.14: A front view of the cryostat. In the top left of the image two blue cables (a) can be seen attached to the microwave feedthrough. Beneath, yellow plastic clad fibres for the laser excitation zone are taped to the black support frame. These come from a laser table via underfloor trunking. These can be seen connected to a feedthrough in the upper right of the image (b). Most of the equipment seen above the cryostat is valves and a turbomolecular pump for the dilution and precooling cycles. Below the chamber a large turbomolecular pump (c) is placed to evacuate the chamber, and this is backed with an oil free scroll pump (d) at the bottom of the image.

Chapter 5

Microwave Cavity Resonance Scans

Arguably the most important component of a micromaser is the electromagnetic cavity at the centre of the system. If it has no resonance close to the transition frequency between the two atomic levels of choice, or the quality is too low, then the experiment will produce no new results. Two types of cavity are used. Most prevalent in the laboratory at the time of writing is the ‘pillbox’ or *closed* cavity. The other type which is becoming increasingly important, the *open* cavity, is a pair of mirrors forming a confocal cavity. These are significantly different designs from a measurement perspective. The closed cavity is designed with two holes in to allow atoms to pass through the field, and these can also be used to make measurements of the field. The open cavity needs no holes, so probes are used to measure the properties of these cavities.

These methods were developed to be low power, suitable for use with a cryogenically cooled cavity below 1 K. For fast measurement an alternative set of tests can be produced using high power large linewidth oscillators in a transmission arrangement. The microwaves transmitted through the cavity will be filtered to allow only frequencies close to a resonance.

5.1 Quality Factor

Before doing spectroscopy on a cavity, it is important to know whether or not it is possible. There are methods to determine the quality of a cavity, and methods to determine the resonant frequency of a cavity. For low qualities which return an obvious Lorentzian when swept with microwave frequencies close to resonance, the position of the peak can be used to estimate the resonant frequency, and the width of the peak can be used to estimate the quality factor. However, coupling radiation into cavities to probe them is difficult when they are very high quality. This makes measuring the resonant frequency and quality factor of our cavities difficult tests to design. The quality factor of a

microwave cavity is given by

$$Q = -\omega_0 E \left(\frac{dE}{dt} \right)^{-1} \quad (5.1)$$

where ω_0 is the resonant angular frequency and E is energy. A high Q cavity will have a small decay constant when compared with the resonant frequency. Equivalently the Q factor can be defined by the decay equation for the cavity field

$$E(t) = E_0 \exp \left(-\frac{\omega_0}{Q} t \right) \quad (5.2)$$

i.e. the decay constant $\lambda = \omega_0/Q$. Different parts of the cavity will dissipate at different rates. This can be modelled as each part having different Q factors. The Q is inversely proportional to power loss, so adding the Q factors of parts of a cavity is reciprocal too. The cavity can be split into two Q factors; the body of the cavity and the holes. These correspond to the loss due to microwaves coupling out through the holes and absorption of microwaves by the body of the cavity. The composite Q factor is thus given by

$$\frac{1}{Q} = \frac{1}{Q_H} + \frac{1}{Q_B} \quad (5.3)$$

Equation (5.3) means that if the quality of the holes is significantly higher than the quality of the body, then the preferential route for power to be lost is by the body. Roughly speaking, the hole of a cavity needs to have a Q of the same order of magnitude as the body to be able to load it and see a signal from the cavity as it unloads.

The simplest type of cavity test involves a sweep of a driving microwave field over the resonant frequencies, and looking at the returned power. The results are Lorentzian resonance peaks if the scan is sensitive enough to detect them. When the full-width-half-maximum of the resonance peaks is known, the quality of the cavity may be derived.

$$Q = \frac{\omega_0}{\Delta\omega} = \frac{f_0}{\Delta f}, \quad (5.4)$$

where ω_0 is the resonant frequency and $\Delta\omega$ is the FWHM linewidth.

5.2 Transmission or Reflection?

There are three basic methods that I used to probe cavities

1. Power reflection measurement.
2. Power transmission measurement.

3. Ring-down measurement.

The first tests how much radiation is reflected from a cavity for a range of microwave frequencies provided by a microwave synthesiser step by step as demonstrated in Section 5.3. When the microwaves are resonant with the cavity, the reflected power should be lower than when off resonance.

The second is very similar to the first, but measures the power output from another hole in the cavity. When the microwave source is not resonant with the cavity, no radiation couples into the cavity. When the source is resonant, some radiation will couple in, and some portion will decay through the hole that is being measured. An advantage of this approach is that the cavity acts as a filter, reducing noise from the synthesiser side of the experiment. A disadvantage is that typically only one of the holes is low quality enough to measure radiation decaying from the cavity field.

The third uses a synthesiser over a range of frequencies, again step by step, this time pulsed. During the pulse, if the cavity field is resonant then it will be loaded. When the pulse stops, the field amplitude will decay, and this ‘ringing’ can be measured by taking traces from an oscilloscope. The rate of decay of the signal is used to determine the quality of the cavity. This type of test is extremely labour intensive. There are no oscilloscopes available that have a frequency response capable of measuring 21.4 GHz, so the ringing must be mixed with a nearby frequency generated by another synthesiser. The difference in frequencies is observable on an oscilloscope.

In the subsections that follow I note some experimental results that use these types of methods and comment on the equipment used. I present data that concentrates on reflection and ring-down based measurements as these are the best suited to the pillbox cavities available. These experiments were developed with portability in mind. Future production of cavities will require that measurement equipment can be moved to and from a chemistry laboratory so that Niobium cavities can be measured between incremental chemical etches to bring them close enough to the right resonant frequency for the squeezing apparatus to tune it into resonance with the micromaser frequency. Etches also improve the finish of the cavity surface, enhancing the Q factor. Typically these experiments use a USB to general purpose interface bus (GPIB) converter box to communicate with instruments, and when possible acquire data, so that no specialised data acquisition cards are needed and a laptop can be used.

5.3 Simple scans with a Schottky diode

This is the most basic test that I have performed on microwave cavities. The data presented in this section was taken by me. All code used was solely my work. A diagram of this experiment is shown in figure 5.1. For this type of measurement I programmed a computer to communicate with a Giga-tronics model 2400B microwave synthesiser. The current generation of software is coded in LabVIEW 8.20. The first generation of software was built in C. After a number of iterations of this C code I made the transition to LabVIEW, as its helper functions greatly simplified the

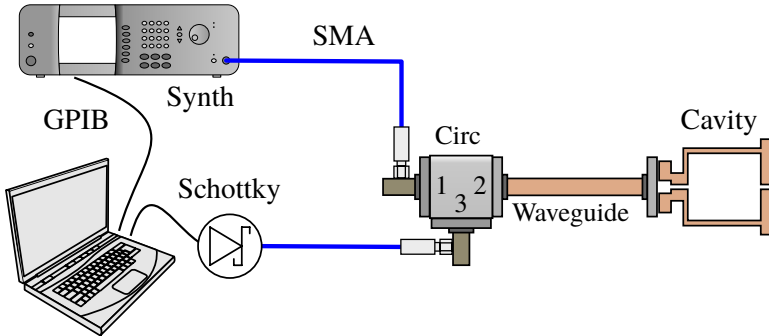


Figure 5.1: The straight forward cavity resonance sweep, suitable for cavities with $Q < 10^5$. A Schottky diode is used as a microwave sensor to measure microwaves reflected from the cavity. When the microwave signal is tuned into resonance a dip in intensity is seen. A circulator routes the incoming microwaves to the cavity and the reflected microwaves to the Schottky diode. Laptop graphic courtesy of the Open Clipart Library.

code. This program takes a start frequency, a stop frequency and a step frequency with an optional time delay. Data is saved into a tab delimited file, which is automatically labelled by date. The Schottky diode measures the microwaves reflected from the cavity and this data is acquired using a National Instruments data acquisition card. Several different data acquisition cards were used and they were roughly equivalent. The model used for data acquisition of resonance sweeps was a National Instruments PCI-6034E with 16 bit analogue inputs.

The microwave frequencies that are not close to the resonance reflect from the cavity, whereas those that are resonant can enter the cavity and be dissipated, so the diode will read a reduction in intensity when the synthesiser is close to resonance with the cavity. Figure 5.2 shows this kind of scan on a copper cavity, and Figure 5.3 is a scan of an aluminium cavity with a low quality lid.

5.4 Simple scans using a power meter

The Schottky diode measurements are only efficient for cavities with relatively lossy holes. When the overall quality of the cavity is increased, or the quality factor of the hole being probed approaches or surpasses that of the body of the cavity, other methods of measuring the resonant frequencies and quality factor of a cavity must be used.

The first improvement that can be made is on the measurement device. A Schottky diode can be replaced with a microwave power meter for more precise measurements over a much larger range. The device I used was a Giga-tronics 8540C power meter. This device was coaxed into giving fast measurements over GPIB to perform as a direct replacement for the diode, eliminating the need for an analogue measurement channel for this experiment. This also makes the experiment more portable, since the power meter is always used for diagnostic tests of the microwave components

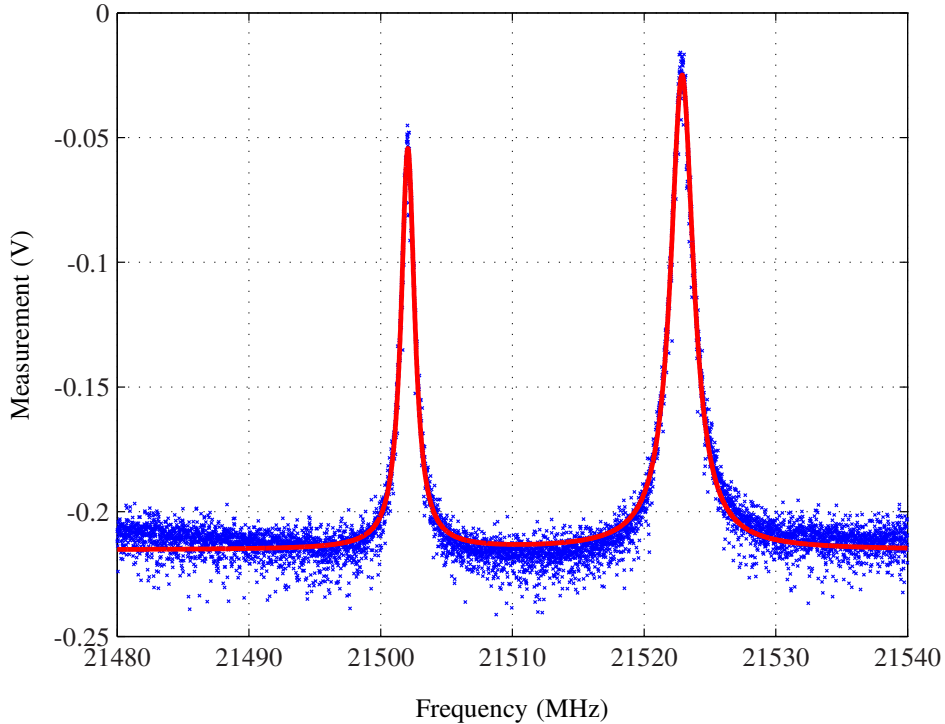


Figure 5.2: This is a plot of data taken using a Schottky diode measuring the reflection of a resonance sweep over the copper cavity with the low Q coupling hole. Since the Q of the body is significantly higher than that of the coupling hole, this kind of sweep easily detects the resonance peaks. The y -scale is proportional to the power, on a negative scale. The blue dots are the raw data points, and the red line is Lorentzian fits to the two resonances. This fit places the widths of the first and second peaks at 1.25 MHz and 2.11 MHz, corresponding to $Q \approx 10^4$. The different resonance peaks are from the short and long axis of the cavity, which has an slightly oval cross section. These two modes also have a different quality factor, although these are close. [71].

and a data acquisition box is no longer necessary. An example scan of a low quality aluminium cavity is in Figure 5.4.

5.5 Ring-Down Spectroscopy

Ring-down spectroscopy is a high precision method of determining the resonant frequencies and quality factor of a cavity. It is often used in the optical domain to study gas samples in a cavity [74], but it is equally valid for measuring properties of a cavity in the microwave domain. This form of test relies on the principle that when a cavity is pumped by a resonant field it will resonate, and when the driving field is turned off a decay of radiation from the cavity can be measured. If the driving field is not close to resonance with the cavity field, the cavity will not be pumped and there will be little decay to detect. When a decay is detected, the quality factor of the cavity is derived

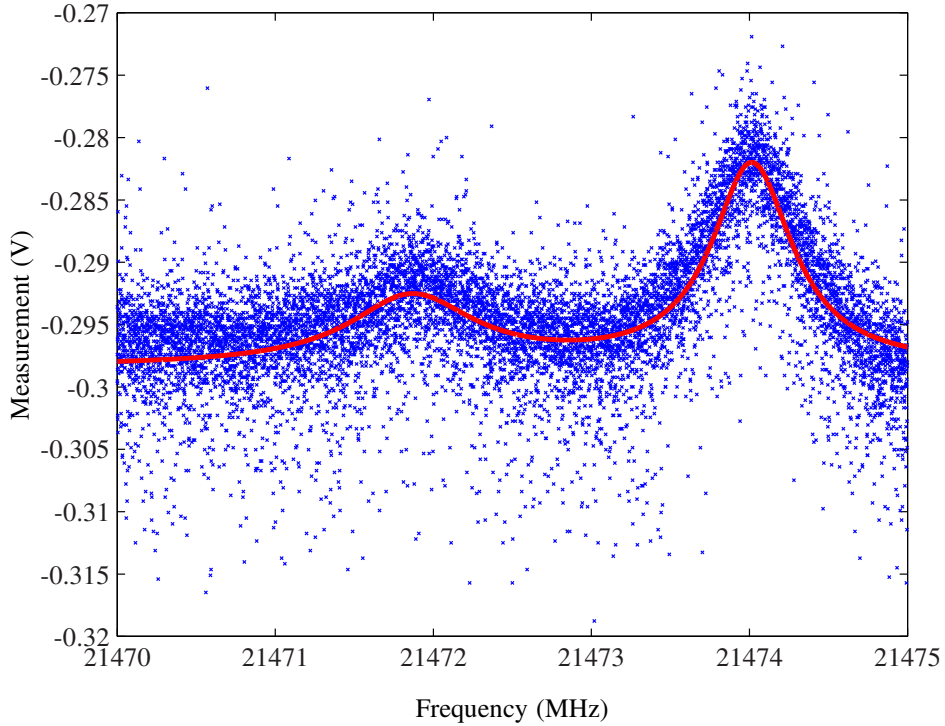


Figure 5.3: This plot was produced in exactly the same way as that in figure 5.2. This was done using the unwelded aluminium cavity with cap 5 (see Figure 4.7), which has the lowest Q hole of the set of caps for this cavity and thus is most easily measured. This is at the limit of the resolution of the Schottky diode. Resolving smaller peaks requires extensive filtering and averaging, and using a power meter becomes a more appealing option. The fit places the linewidths of this cavity at 1.93 MHz and 1.24 MHz placing the quality factor at $Q \approx 1.1 \times 10^4$.

from equation 5.1. For a decay constant given by λ

$$Q = \frac{\omega_0}{\lambda}. \quad (5.5)$$

Several factors make this a difficult test to use. For very high quality cavities the linewidth is extremely small compared with the range of frequencies that a resonance may be found within. This means that the test is slow to perform as the sweep over relevant frequencies must be slow in order to spot the decay. The cavities we manufacture have resonant frequencies around 21.4 GHz, which was far beyond the frequency response of any available oscilloscopes. The signal from a cavity decay must hence be mixed with microwaves from a second synthesiser to see the decay on an oscilloscope. This is particularly difficult because if the synthesisers are not kept at a steady $\Delta\omega$ separation then the change in the frequency response of a mixer may be mistaken for a resonance. Finally, this task cannot be automated. The quantity of data generated is too large to process in real time, so an oscilloscope must be manned and the synthesisers controlled by hand to allow the

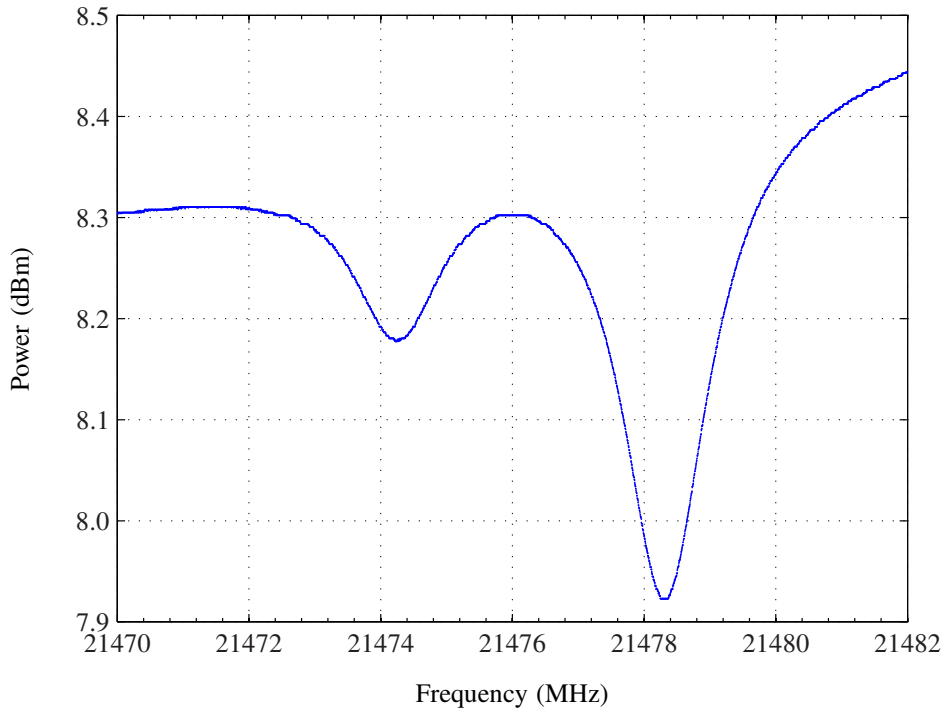


Figure 5.4: This plot is a scan of the same cavity and cap as in figure 5.3, using a power meter in the place of the Schottky diode. This data is so clean that it did not require any filtering. As with figure 5.3 the Q factor of the resonances is $Q \approx 1.1 \times 10^4$. The shift in frequency of the peaks is likely due to this scan being performed in an air conditioned environment, with a cooler cavity.

movement back and forth over a resonance. Observing a resonance is something of an art form, and it is impossible to know if a resonance can even be observed in a cavity before an observation has been made. Needless to say, this was my least favourite test and it consumed countless hours of my time.

One small refinement I made was a small utility that can set the frequency of one synthesiser or grab it from the device, and with a user defined step size move the frequency up or down with the second synthesiser at a set frequency difference Δf from the first. Keeping Δf constant stops it from moving outside of the oscilloscope frequency range, and allows narrow filters to be applied to remove noise.

I have included two figures to show the output of this kind of measurement. Figure 5.5 shows an aluminium cavity ring-down. Figure 5.6 is a curiosity that occurred because the linewidths of two resonant frequencies and the separation between the resonance peaks is similar. This led to a beat between the two decaying frequencies.

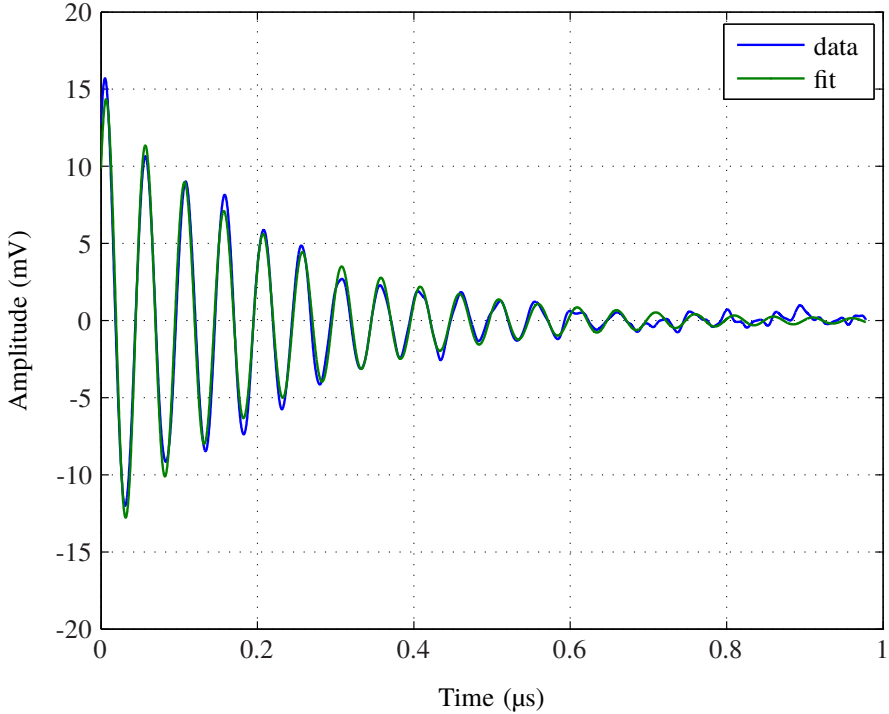


Figure 5.5: This plot shows the ring-down seen from a relatively low quality cavity, with a fit used to calculate the decay constant. Using this the quality factor was calculated to be $Q = 4600$. Note that this is actually the measurement of the ring-down signal multiplied by another microwave signal 20 MHz different from it. This results in a decaying oscillation that appears to be oscillating at 20 MHz, which is within the frequency response of the LeCroy Waverunner Xi that I used to take the data for this plot.

5.6 Using a Lock-In Amplifier for High Quality Resonators

Very high quality cavities return a signal that will be so weak that it will be overwhelmed by noise. This is due to high Q holes leading to very long filling times, so very little radiation is coupled into the cavity [71]. A lock-in amplifier can be used to recover enough signal to find a resonance. This test is based upon the simple sweep with a Schottky diode. The synthesiser has a frequency modulation driven by a signal generator. This signal is fed to the lock-in amplifier as a reference signal. When the synthesiser is over a resonance of a cavity the additional modulation will cross the resonance leading to a periodic signal from the Schottky diode which the amplifier can lock to. The locking signal gives the position of the resonant frequency. For this test I used a SIGNAL RECOVERY 7265 dual phase DSP lock-in amplifier in addition to the equipment in section 5.3. This device was controlled by GPIB and a data acquisition card used to measure the locking signal from a terminal on the back of the device.

This method can be very difficult to implement. The lock-in amplifier is set to detect signals at

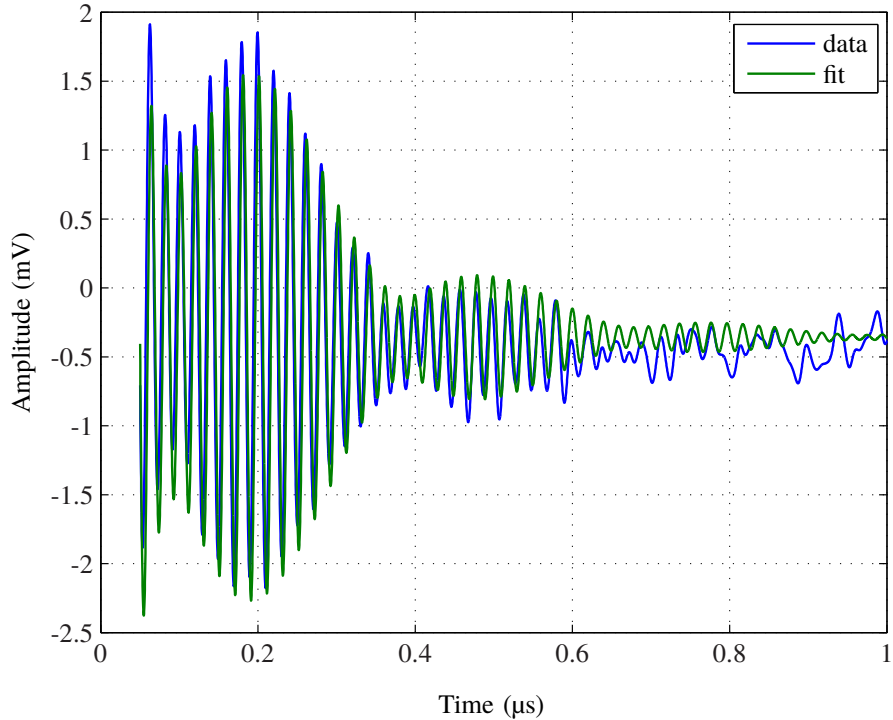


Figure 5.6: For this plot a synthesiser was tuned to half way between the resonant frequencies of the aluminium cavity with the low quality lid at 21.471 GHz. The resonant frequencies are close enough together that the synthesiser loads both modes at the same time, so that the decay from the cavity is at both frequencies. This was an unexpected effect. A loose analogy for each mode is that a pendulum can be driven at a frequency close to (but not at) resonance, and when the driving stops the pendulum will oscillate at its natural frequency. The fit gives the resonant frequencies with a separation of 3.44 MHz which is the frequency of the envelope.

the second harmonic of the reference frequency. As the modulated synthesiser frequency is centred on a resonance, a Fourier transform of the idealised signal from the Schottky diode would show a peak at the second harmonic of the reference frequency. The fact that a component of the signal from the Schottky diode will be at the second harmonic close to resonance is used by the lock-in amplifier. This modulation frequency must be chosen to maximise the second harmonic component in the return signal. If the modulation is too large, then the Lorentzian peaks will be so far separated that the second harmonic component is reduced. If the modulation is chosen to be close to twice the full-width-half-maximum of the resonance then the second harmonic component will be maximised for detection. Therefore in order to see a resonance in this test an educated guess at the linewidth of the cavity must be made.

To verify this assumption I derived the signal that the Schottky diode should produce

$$S = S_0 \frac{\Gamma^2}{4(\alpha\Gamma \sin(\epsilon t) - \omega_0)^2 + \Gamma^2}, \quad (5.6)$$

where Γ is the line width, $2\alpha\Gamma$ is the window of frequencies modulated over (the frequency varies between $\omega_0 \pm \alpha\Gamma$), S_0 is a scale factor and ϵ is the modulation frequency. This equation for several values of α is plotted in Figure 5.7.

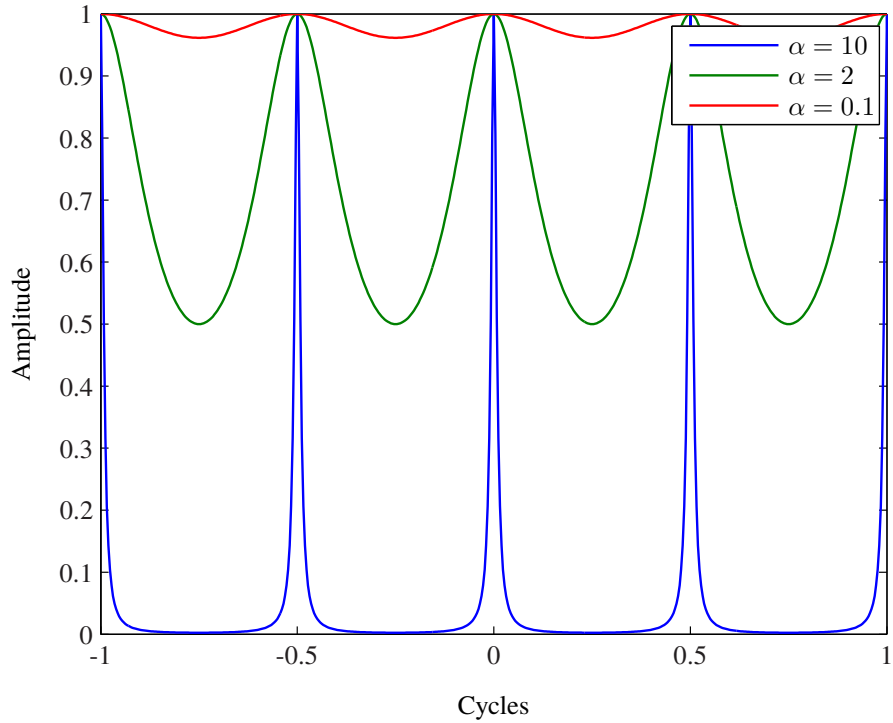


Figure 5.7: If the modulation (α is a multiple of the linewidth) on the synthesiser is chosen to be large (blue curve) with respect to the linewidth of the resonance peak then the resulting signal has a small sinusoidal component at twice the modulation frequency. If the modulation is chosen to be approximately the linewidth, then the sinusoidal component is maximised (green). If the modulation is too small then there is still a sinusoidal component, but the amplitude is reduced.

To maximise the signal that the lock-in amplifier is sensitive to, the second harmonic component needed to be maximised. The second harmonic component of equation 5.6 was found by deriving the second cosine component of the Fourier series of S and differentiating it with respect to α . The solution to the resulting equation places the optimal value at $\alpha = 1$, i.e. the assumption that the modulation amplitude should be approximately the linewidth was accurate. To test this assumption the aluminium cavity with cap number five was used again as a benchmark. The result of this scan is shown in Figure 5.9. Figure 5.8 shows an equivalent scan using the first harmonic.

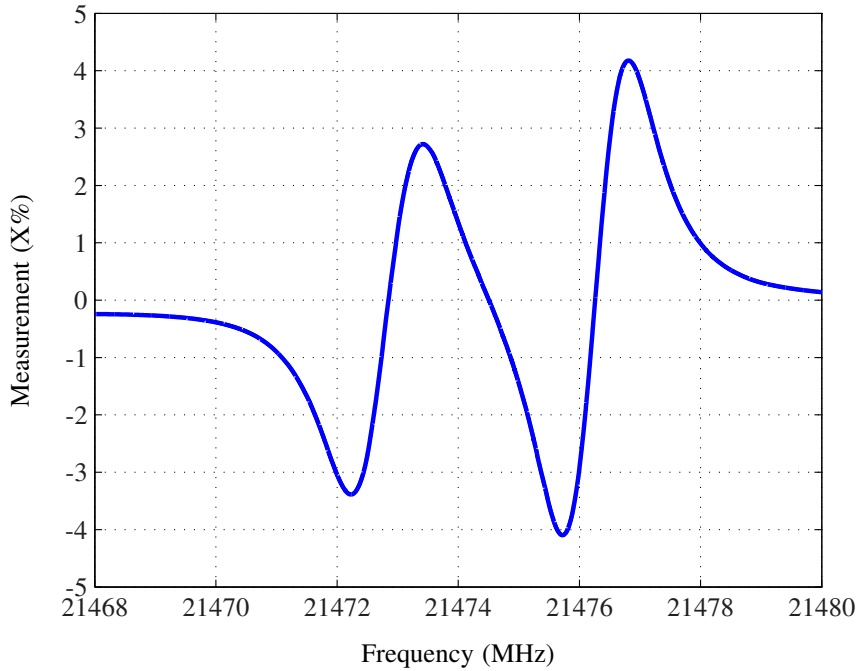


Figure 5.8: This is a scan of the aluminium cavity with cap number 5. As the linewidth of this cavity is already known to be about 2 MHz, this was used as the modulation amplitude on the microwave synthesiser to maximise the signal from a lock-in amplifier. The amplifier was programmed to take the frequency of modulation as a reference, and output a locking signal corresponding to frequency of this reference. This is locking to the first harmonic, which was not the ultimate goal. It works well on Al-05 because it already responded well to the Schottky diode with a relatively low noise. The signal from the Schottky is out of phase with the reference as the synthesiser moves over the start of a resonance, and as it passes the centre of the resonance it moves into phase, leading the plot to look like some multiple of the derivative of the resonance peaks.

Unfortunately, whilst locking to the second harmonic did produce a signal with a better signal to noise ratio than a raw scan output of the Schottky diode, it is not a particularly impressive improvement. Using the first harmonic, the amplifier is sensitive to the edges of the resonance, where the gradient is larger than the background.

5.6.1 Discussion

A lock-in amplifier can be used to dramatically improve the signal from a cavity resonance. Both first and second harmonic scans have been successfully attempted, and the first harmonic scans have proven to be extremely sensitive. These scans are only effective for locating resonant frequencies of a cavity, and other methods are better suited to resolving the linewidth. If these can be improved further, then it will be possible to write a program that will acquire a resonant frequency of a cavity and follow it as the cavity is cooled in the cryostat. This will be particularly useful for gathering data

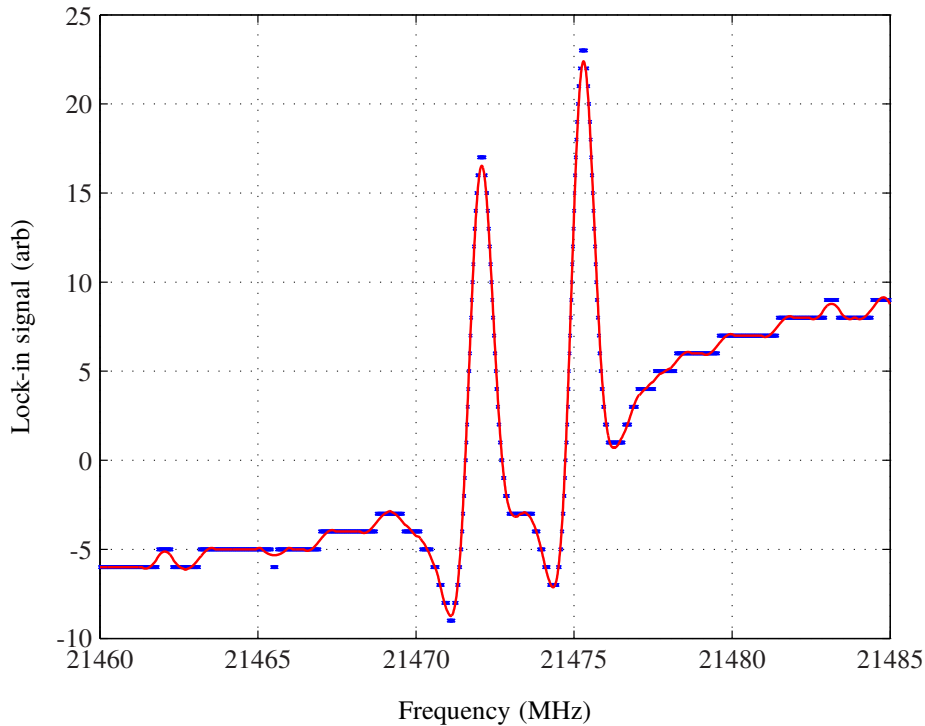


Figure 5.9: Using the second harmonic, the lock-in amplifier is sensitive to the peak of a resonance, as modulating the synthesiser with frequency f when it is centred on the resonance will produce a signal with frequency $2f$, as in figure 5.7.

on how the cavities change with temperature, and at what temperature the superconducting transition occurs. We are interested in using aluminium in the place of niobium for making cavities, and the precise behaviour of aluminium and aluminium oxide at very low temperatures needs research.

5.7 Using a Lock-In Amplifier with Ring-Down Measurements.

It is possible to eliminate many of the issues with ring-down measurements. By using a splitter to bleed a small amount of the microwave power from the synthesiser, microwaves decaying from the cavity can be beat against the bled off power. A mixer allows the beat to be measured. If the synthesiser is modulated fast, and by a similar frequency to that of the lock-in amplifier oscillator, then the decaying microwaves from the cavity will be detected by the lock-in amplifier around the resonant frequencies.

This method will produce a signal for relatively low quality cavities, but it is more appropriate to use on higher quality cavities. This is due to the limit on the lock-in oscillator frequency at 250 kHz, and as the frequency modulation of the synthesiser should be close to this frequency too, the most effective results will be seen when the linewidth of a resonance is less than 250 kHz. Longer

lifetimes will lead to slower modulation, so for high quality cavities the modulation frequency will go down. This is also in line with the shrinking linewidth with rising quality factor. As such this type of test will become more useful when higher quality cavities are available to test.

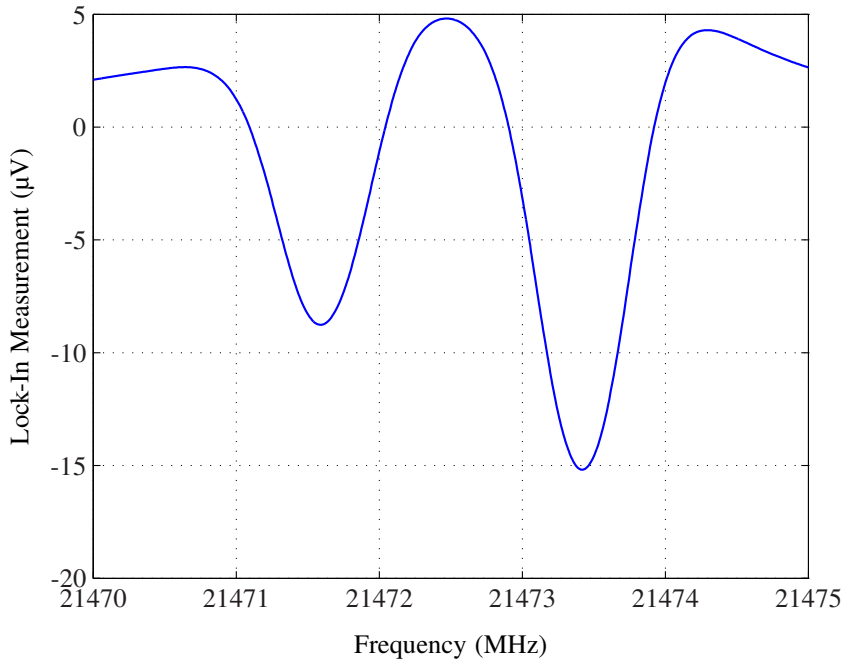


Figure 5.10: By modulating the synthesiser, the decaying microwaves from a cavity are beat against a range of frequencies. When the synthesiser is modulating over a resonant frequency the decay is much larger since the resonant field can be loaded. The two dips seen in this plot are two resonant frequencies from an aluminium cavity.

A further improvement uses two synthesisers. This was a problem before because they needed to be dialled by hand, but now both synthesisers can be controlled programmatically, and kept separated by the reference frequency. This test can only be performed using the transmission arrangement, and is effectively just an enhanced resonance sweep. The expected signal is much like that seen for the first harmonic lock-in measurement of the aluminium low quality cavity in figure 5.8.

5.8 Summary

Several types of experiment have been shown in this chapter. The recent success of the new microwave lines means that the next step will be to trial these on a cavity inside the cryostat. These scanning methods are available and portable for when the production of new cavities starts. Furthermore, the tests all have programs to run them with a simple user interface so that the person etching a cavity will need no particular expertise to test it. These tests were all performed with a

CHAPTER 5. MICROWAVE CAVITY RESONANCE SCANS

retort stand to hold the cavity and microwave components. To assist with mobile testing a harness will be constructed that a cavity can simply be clipped into for testing.

The new Fabry-Pérot (open) cavities will also be tested using these methods. The sweeps should be done for these cavities using a transmission arrangement rather than a reflection arrangement for the frequency sweep tests, but essentially there is no change in how the tests are performed. The radiation can be coupled into and out of the field using small microwave aerials which are placed at the edge of the cavity field in order to avoid perturbation of the resonant frequency and lowering of the quality.

Conclusion

Summary of Results

Cavities may be used to hold quantum information. I showed in Chapter 2 that this can be extended so that operations may be performed on qubits stored in a multi-mode cavity field without entangling the atoms with the system. The passage of an atom is analogous to a clock pulse. I demonstrated that a universal gate set is possible, and there is significant flexibility for constructing more gates. This theory may also be applicable to other systems that use the JCM. Circuit QED, quantum dots and ion traps may be interesting in this context.

In Chapter 3 I showed how to use a controlled phase gate consisting of a cavity and two atomic qubits to construct graph states, including N -atom GHZ states, cluster states and hexagonal graph states. The generation of these states is continuous, so that a graph state can have effectively infinite depth. This avoids the decoherence that a large preprepared graph state will be subject to, as the parts of the state to be operated on are generated dynamically. Single qubit rotations have already been performed, satisfying the requirements for universal one-way quantum computation. I also demonstrated that the controlled phase interaction equipment can be used to build three and four atom W states.

GHZ states are a type of graph state that are interesting in their own right. Tests of non-locality that can be performed in a single shot are possible with them, in contrast with Bell tests, which require many runs to resolve an answer. GHZ states are also known to be very sensitive to dephasing. I showed that this sensitivity can be leveraged to construct an improved test of quantum gravity with a better scaling in sensitivity than atom-interferometers which are currently used. These tests cannot single out a particular theory of quantum gravity, but by showing that a GHZ state dephases more slowly than a particular theory predicts, then that theory can be ruled out.

Chapter 4 contains details on the micromaser experiment at Leeds university. I was responsible for the day-to-day running of the cryostat, the routing of high and low voltage cables, microwave lines and optical fibres and the mounting of components in the experimental region. In particular the new microwave lines and superconducting low voltage lines have been very successful.

Chapter 5 showcases methods I have used to probe cavities. Using these, the resonant frequencies and quality factors of high quality cavities can be determined inside the cryostat. I designed the tests to be portable and simple to use with custom programs that set up the equipment and automate scans for a user who may have no expertise in physics. This will allow a person etching cavities in a chemistry laboratory to perform tests.

Future Work

The work on multi-mode quantum optical logic will be continued with the extension of the theory into dissipative systems. This will allow quantum gates to be modelled under realistic conditions.

CONCLUSION

Extensions of the optical qubits into qudits will be explored as an option. Other host systems will be explored to see if analogues of this type of gate exist, and if they have benefits over cavity QED.

In Chapter 3 most of the work has been done for producing graph states, and is waiting for an experimental realisation in the laboratory. The cavities involved are rather large, so research into alternative interactions and cavity geometries should be done to see if this can be improved. For the entanglement enhanced tests of quantum gravity NOON states of atoms will be considered in optical lattices, and perhaps Bose-Einstein condensates in a superposition of two positions. Both of these ideas increase the mass of the effective particle in superposition. Continued research will lead to an experiment that will place a new minimum value on the background parameter discussed in Section 3.5.2.

The candlestick oven in Section 4.2.1 is near completion. When an order of glass fibre arrives, this can be inserted into the oven to act as a wick and the oven can be tested. With the candlestick oven running, long term operation becomes possible. With the current rubidium dispensers the life of the dispenser is typically less than a day, limiting the duration of future experiments.

The dilution cycle of the cryostat was recently cleaned after a large contamination of the cycle occurred. Now that the cryostat is operational it is possible to cool a cavity down to 30 mK. The first test that should be done is with a low quality factor aluminium cavity. Observation of the superconducting transition and the contraction of the cavity made of aluminium will allow us to determine the usefulness of aluminium as an alternative cavity material to niobium. Cavities that superconduct have more reflective surfaces due to the reduction in resistive losses in the cavity walls, leading to higher Q factors. The final components that need routing in the cryostat are high voltage lines to the detector box that minimise heat conduction. An alternative option is to use electron optics to deliver electrons from ionised Rydberg atoms up to a detector box mounted at a higher temperature, avoiding the problem of the high voltage lines conducting more heat than the cryostat can handle. This will save valuable space in the experimental region and keep the CEMs warmer, and thus more efficient. The next student to join the micromaser team will be assigned to constructing high quality microwave resonators. With a high quality cavity, the system will be ready to perform experiments.

The new cavity resonance scans and tests to measure quality factors showcased in Chapter 5 will be used in the production of new cavities at the correct frequency. To aide in this, a harness will be constructed to clip a cavity into for testing, and this will bolt directly onto the waveguide circuit used. With a cycle of baking and etching the cavity to eliminate impurities, very high quality factors on the order of $Q = 10^{11}$ are attainable [70]. These scanning techniques will also be used in the cryogenic tests of new cavities.

Part IV

Appendix

Appendix A

Extended Derivations

This part of the appendix contains expanded derivations.

A.1 Zheng and Guo's Controlled Phase Gate

This section contains an extended derivation. The derivation presented in [35] appears to simply jump to the second order process for the effective Hamiltonian. This approach may be too simplistic, so I have opted for adiabatic elimination for a more rigorous route. I start with the two atom Tavis-Cummings Hamiltonian.

$$H_{\text{TC}} = \sum_{j=1}^2 \left[\frac{\hbar\Delta}{2} \hat{\sigma}_3^{(j)} - i\hbar g \left(\hat{\sigma}_{(j)}^+ \hat{a} - \hat{\sigma}_{(j)}^- \hat{a}^\dagger \right) \right]. \quad (\text{A.1})$$

This interaction involves two atoms and the field, with the field detuned into the dispersive regime to adiabatically eliminate it. A transformation can be made using $\Theta = \frac{\hbar\Delta}{2}(\hat{\sigma}_3^1 + \hat{\sigma}_3^2)$ to get to an interaction picture similar to that used by Zheng and Guo

$$H'_{\text{TC}} = -i\hbar g \sum_{j=1}^2 \left[e^{i\Delta t} \hat{\sigma}_{(j)}^+ \hat{a} - e^{-i\Delta t} \hat{\sigma}_{(j)}^- \hat{a}^\dagger \right]. \quad (\text{A.2})$$

I will continue by using H_{TC} rather than H'_{TC}

Once again the theory of effective Hamiltonians is used. The projection operators are chosen to be

$$\begin{aligned} P &= \hat{\sigma}_2^+ \hat{\sigma}_2^- \hat{\sigma}_1^- \hat{\sigma}_1^+ + \hat{\sigma}_2^- \hat{\sigma}_2^+ \hat{\sigma}_1^+ \hat{\sigma}_1^- \\ Q &= \hat{\sigma}_2^- \hat{\sigma}_2^+ \hat{\sigma}_1^- \hat{\sigma}_1^+ + \hat{\sigma}_2^+ \hat{\sigma}_2^- \hat{\sigma}_1^+ \hat{\sigma}_1^- \end{aligned} \quad (\text{A.3})$$

APPENDIX A. EXTENDED DERIVATIONS

to satisfy $PP = P$, $QQ = Q$, $PQ = QP = 0$, and $P + Q = \mathbb{1}$. Note that these only operate on the atoms. The effective Hamiltonian is built using the equation

$$\begin{aligned} H_{\text{eff}} &= PHP - PHQ(QHQ)^{-1}QHP \\ &= H_0 - BA^{-1}B^\dagger. \end{aligned} \quad (\text{A.4})$$

Using H_{TC} yields the parts

$$\begin{aligned} H_0 &= 0 \\ A &= \hbar\Delta(\hat{\sigma}_2^+\hat{\sigma}_2^-\hat{\sigma}_1^+\hat{\sigma}_1^- - \hat{\sigma}_2^-\hat{\sigma}_2^+\hat{\sigma}_1^-\hat{\sigma}_1^+) \\ B &= -i\hbar g(\hat{\sigma}_2^-\hat{\sigma}_2^+\hat{\sigma}_1^+\hat{a} - \hat{\sigma}_2^+\hat{\sigma}_2^-\hat{\sigma}_1^-\hat{a}^\dagger + \hat{\sigma}_1^-\hat{\sigma}_1^+\hat{\sigma}_2^+\hat{a} - \hat{\sigma}_1^+\hat{\sigma}_1^-\hat{\sigma}_2^-\hat{a}^\dagger) \\ B^\dagger &= i\hbar g(\hat{\sigma}_2^-\hat{\sigma}_2^+\hat{\sigma}_1^-\hat{a}^\dagger - \hat{\sigma}_2^+\hat{\sigma}_2^-\hat{\sigma}_1^+\hat{a} + \hat{\sigma}_1^-\hat{\sigma}_1^+\hat{\sigma}_2^-\hat{a}^\dagger - \hat{\sigma}_1^+\hat{\sigma}_1^-\hat{\sigma}_2^+\hat{a}) \end{aligned} \quad (\text{A.5})$$

Consider that A spans the states $|e, e\rangle$ and $|g, g\rangle$, which are to be eliminated. This is perhaps more clear in the block-wise notation. The inverse of A should thus result in $AA^{-1} = |e, e, n\rangle\langle e, e, n| + |g, g, n\rangle\langle g, g, n|$, i.e. identity over these states. With this in mind, the inverse of A is simply

$$A^{-1} = \frac{1}{\hbar\Delta}(\hat{\sigma}_2^+\hat{\sigma}_2^-\hat{\sigma}_1^+\hat{\sigma}_1^- - \hat{\sigma}_2^-\hat{\sigma}_2^+\hat{\sigma}_1^-\hat{\sigma}_1^+). \quad (\text{A.6})$$

Finally these parts are multiplied together to get

$$\begin{aligned} H_{\text{eff}} &= \frac{\hbar g^2}{\Delta}(\hat{\sigma}_1^+\hat{\sigma}_1^-\hat{\sigma}_2^-\hat{\sigma}_2^+ + \hat{\sigma}_1^+\hat{\sigma}_2^- + \hat{\sigma}_1^-\hat{\sigma}_2^+ + \hat{\sigma}_1^-\hat{\sigma}_1^+\hat{\sigma}_2^+\hat{\sigma}_2^-)[\hat{a}, \hat{a}^\dagger] \\ &= \frac{\hbar g^2}{\Delta}(\hat{\sigma}_{ge,ge} + \hat{\sigma}_{ge,eg} + \hat{\sigma}_{eg,ge} + \hat{\sigma}_{eg,eg})[\hat{a}, \hat{a}^\dagger]. \end{aligned} \quad (\text{A.7})$$

The commutator has been left in as an explicit reference to identity for the field. This Hamiltonian is the same for these states as Zheng and Guo's Hamiltonian, albeit rather different in appearance. From the eliminated terms it is clear that the states $|e, e, n\rangle$ and $|g, g, n\rangle$ do not couple to other states and are subject only to phase evolution.

The effective Hamiltonian for the $|g, g, n\rangle$ component is still important. To avoid phase related problems the state of the field is chosen to be $n = 0$. This is where it becomes important that the cavity is as cold as possible. In this limit H_{TC} reduces to $H_{\text{TC}} = -\Delta$ for the state $|g, g\rangle$. It is a good idea to chose $n = 0$ anyway, since any field state except for a number state will lead to some phase spread in the resulting gate. The only state for which the number states and the thermal states converge is the $n = 0$ state.

The effective Hamiltonian for $|e, e\rangle$ is unimportant. The makeup of the gate is such that this state never exists in the cavity.

Appendix B

Code

This appendix contains samples of code I have written in my time as a graduate student, in the hope that it may be useful for those following me.

B.1 Log File Converter

I wrote a small script called **log2ascii** to turn the Vericold cryostat binary log files into ASCII tab delimited files. This was used to extract the cryostat data plotted in chapter 4. These log files are atypical, as the first 12288 bytes are in ASCII with some binary junk, and everything after is in binary. Programmes like Matlab could not handle these log files easily so I wrote this script to allow batch conversion at the command line. This script converts the Vericold files to comma delimited text files with column headers.

The string portion of the log files is partially garbled, with random binary mess between useful strings. Sorting this is beyond my ability to code in a reasonable time, so I resorted to standard Unix command line programs. My colleagues and I in the laboratory predominantly use Linux and Macs which inherit from Unix, and those who don't have easy access to a machine that also does or Cygwin on Windows which ports these utilities. The shell script makes extensive use of *pipes*, which send the output of one program to the input of the next. This can be viewed as a series of transformations on the input to get the desired output.

The script begins by determining the name of the input file, and creating a new filename which is identical except for the .csv suffix. This stands for *comma separated values* and is recognised by most statistics software or spreadsheet packages. The next thing the script has to do is determine the number of columns in the file. Earlier log files had 53 columns and later ones 51. This may change again so hard coding is a bad idea. Fortunately the first column of data in the file is filled with the number of bytes on each line. The script gives the file to *hexdump*, which skips the first 12288 bytes and reads the following 8 bytes, i.e. the first double precision floating point number

in the file, which is the number of bytes in the first row. Bash is then used to return this number divided by eight, which is the number of columns in the first (and thus every) row.

Next the script finds the column headers by reading the first 12288 characters of the input file using the command *head*. This is then handed to *strings* which extracts the useful strings from the binary mess, placing each string on its own line. The number of columns determines how many lines *tail* takes off of the end for column headers, and this is sent to *tr* to swap the newline characters for commas. Finally *sed* cleans a comma off the end of the line and the comma separated column headers are written to the output file.

The final stage uses *hexdump* again; this time to decode the entire binary block of the file. The contents are decoded into comma separated values in the appropriate number of columns, and then *sed* is used to remove the comma on the end of every line.

This approach was extremely fast to code. Remarkably the ASCII file that results from this is considerably smaller than the Vericold log file, voiding any advantage the bizarre format could possibly have, save for obfuscating data.

```

1  #!/bin/sh
2
3  # log2ascii: Convert Vericold log files to a human readable format.
4  # This is useful for importing data into Matlab/Octave or a spreadsheet.
5
6  for file in $*
7  do
8      # Work out the output filename.
9      newfile=${file%.*}.csv
10     # Work out number of columns.
11     columns=$((`hexdump -s 12288 -n 8 -e '%%g' ${file}` / 8))
12     # Create output file and place column headers.
13     head -c 12288 ${file} | strings | tail -n $columns | tr '\n' ',' | sed 's/,,$
14         //' > $newfile
15     # Decode binary data and place in output file.
16     echo $columns/8 \'%g,\\"'\n'\\\'\\\'\n'\' > format.temp
17     hexdump -s 12288 -v -f format.temp ${file} | sed 's/,,$//' >> $newfile
18     rm format.temp
19     echo "created $newfile"
20 done
21 exit 0

```

Listing B.1: log2ascii.sh

B.2 Power Meter Cavity Resonance Sweep

I have included figure B.1 as an example of LabVIEW code. It is a relatively small programme, and some of the detail is hidden as only one event in the event structure can be viewed at a time. This is simply supplied as a code sample. LabVIEW has many possible coding styles, but here I have followed conventions. It is my hope that students following me will learn a few tricks from this.

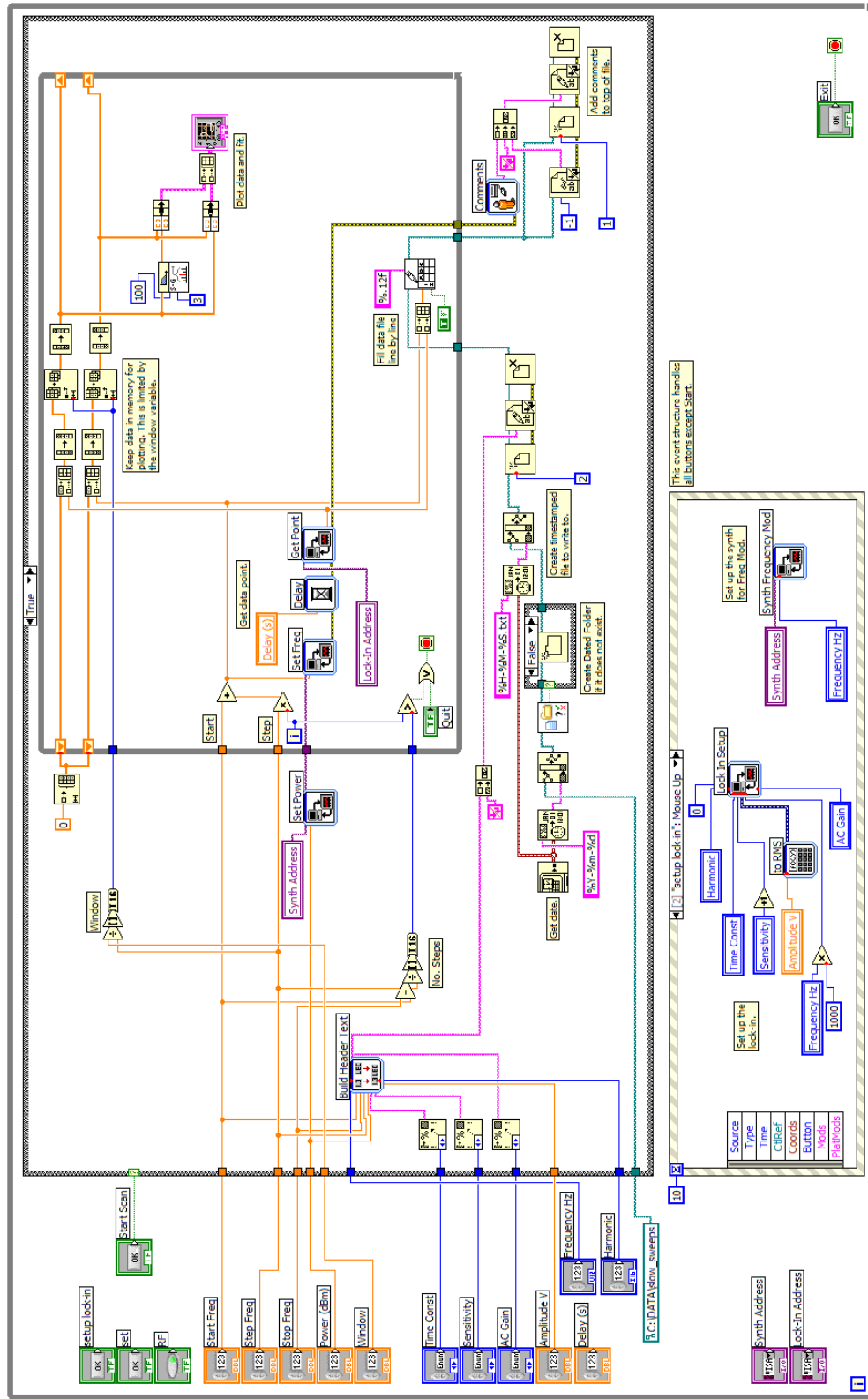


Figure B.1: This code steps a microwave synthesiser by a given step frequency over a frequency range, and for each step acquires data from a lock in amplifier as discussed in section 5.6. All control and data acquisition is done using GPIB.

Appendix C

Revised Cryostat Operation

The Vericold dilution refrigerator used in the laboratory has had some modifications since the group acquired it. In particular the precooling/dilution stage compressor has been replaced with a model less prone to the valves becoming stuck closed. The software for the cryostat has also been updated, which introduced new problems. In particular the compressor for the pulse tube cooler must now be started manually. The original instructions are also contradictory in places, so I felt it necessary to place a revised version of the instructions in this appendix. An original version can be found in Bruno Sanguinetti's thesis [63].

C.1 Preparation

After any major work has been done close to internal helium lines, a sniffer test should be done to check that no pipe has become ruptured. To do this the helium lines must be pressurised to slightly above an atmosphere with Helium, so that any leaks can be identified by the jets of helium they produce. Helium from a gas bottle should be used, and the lines thoroughly pumped out again before use to avoid contamination by water and nitrogen. Pumping these lines overnight produces good results.

Internal shields should be put together using two people to avoid contact with sensitive parts. Make sure before starting that you have a 2.5 mm ball driver, a 2.5 mm Allen key, a 3 mm ball driver and two 6mm ball drivers before starting. The 2.5 mm ball driver can be used for most of the screws, but the ones facing down on the 70 plate will need an Allen key to fit. If thermal connection between the shields is a problem then Apiezon N grease can be used.

The vacuum chamber should be put together with care to clean every seal that has been opened. Metallic surfaces with no Viton seal ring should be cleaned using a lint-free wipe and methanol (use gloves). Surfaces with a Viton ring should be wiped clean with a dry lint-free wipe, and a small amount of vacuum grease reapplied to the ring. This should be a thin layer, enough to make

the Viton look wet without any streaks or globs. Use gloves throughout this procedure.

The vacuum chamber needs at least two people to put together. For the upper shield, there are two bolts in the top plate in place to guide the shield in. Take care, since these bolts could easily scratch the seal. Once the shield is in place one person can hold the shield in place whilst the other fastens the bolts. The lower shield is a similar process, but will need lining up as there are no guide bolts. The bottom plate uses the 3 mm hex key. If the plate with the large turbomolecular pump is to be attached then one person must pinch it in place whilst the other fastens the bolts due to the weight. When the chamber is closed it is worth performing a leak test. The chamber Penning gauge will need to be turned on before the pressure is too low to operate properly. Do this when the pressure is $\approx 1 \times 10^{-3}$ mbar. This gauge must be turned on for the software to allow the cooler to operate.

C.2 Pulse Tube Cooling

This is the first stage in starting the cryostat. The pulse tube actively cools the 77 K and 4 K stages in a simple to use closed cycle. Originally this was fully automatic, but issues with the software mean that the compressor must be started manually. Before starting the pulse tube cooler, check that

1. The vacuum in the chamber is $< 1 \times 10^{-3}$ mbar. If the chamber is stable at this pressure then you probably have a leak. Ideally the pressure should be $< 1 \times 10^{-4}$ mbar.
2. All lines are connected.
3. Coolant water is flowing to the compressor. If you are using a large turbomolecular pump make sure water is flowing to this too.
4. The Penning gauge is turned on and working properly.

Once this list has been checked it is safe to start the pulse tube cooler as follows:

1. Using the software, turn on the rotary valve.
2. Once the valve is working, press the **on** button on the compressor. The pressure on the compressor should be flickering around the red bar.
3. Use the software to start a new log file and display a plot of the temperatures in the cryostat.

C.3 Pre-cooling

As the 77 K and 4 K stages are cooling, a thermal connection between the mK stage and the 4 K stage must be made to cool the mK stage. This connection is referred to as *precooling*. Put simply,

a small amount of the helium mixture is pumped through the precooling line to produce a thermal contact between the mK stage and the 4 K stage. This is a necessary step before the mixing cycle.

1. Close all valves, except for V1, V2, V20, V22, V28¹ and V32 which should be opened after the rest have been closed if they are not already open.
2. Open V11. M4 should measure some mixture.
3. Open V29. M3 should measure 0.8 bar.
4. Open V10 to equalise M3 and M4 measurements.
5. Check that the backing pump works by toggling the “fore-pump” switch.
6. Open V7 to complete the pre-cooling line.
7. Start the compressor.
8. Open V12 slowly to raise the pressure readings from M1 and M2 slightly. M1 should register a much higher pressure than M2 if the compressor is operating properly. A good pressure to keep on M1 is 1 bar². Previous revisions state a maximum of 6 bar, but with the new compressor this is not recommended and will ultimately lead to ice buildup on the outlet line.
9. Close V10.

Take care that the outlet pipe from the cryostat does not ice up. If this happens then the flow is too high and the cooling suboptimal. This may also compromise the helium lines by breaking seals. In this event reduce the flow by allowing some of the helium back into the holding tank via V6.

C.4 Mixing Cycle

The mixing cycle is the final stage of cooling. This stage may only be started when all the sub-4 K thermometers measure less than 20 K, but above 10 K to ensure that the helium vapour pressure is high for better flow and cooling power. The chamber pressure should be $\approx 3 \times 10^{-7}$ mbar. This process assumes that the precooling cycle is running. First pre-cooling must be evacuated.

1. Some of the Helium can be let back into the holding drum through V6 with the compressor. Do this and then close V6.
2. Make sure that V24 is closed and that V10 and V11 are open.

¹If the helium lines are over-pressured then OPV1 returns excess mixture to the holding drum, but V28 must be open to allow this. It is extremely important that this is open when the cryostat is in operation. OPV1 activates when the pressure exceeds 8 bar

²Remember that the gauges are 1 bar off as they have a vacuum around them, so 1 bar looks like 0 bar on the gauge.

3. Turn on the fore-pump.
4. Open V31.
5. Open V5.
6. After the bulk of the Helium is in the holding drum, the turbomolecular pump can be used to help evacuate one side of precooling. Close V23 and V1, and open V35 and V24. Turn on the turbomolecular pump.
7. V4 and V21 may also be opened if there is some concern of pressure in the mixing cycle. The compressor must remain on to allow the flow of helium through it.
8. Leave pumping for between one to four hours.

With pre-cooling evacuated, the mixing cycle must be filled. In this stage the cycle is filled and topped-up as helium condenses. Assuming that all the steps above have been followed the next sequence of instructions should start the mixing cycle. Ideally the pre-cooled parts of the cryostat should be below 6 K.

1. Close V35, V2, V4, V5 and V10. Make sure that V8 is also closed. Leave the fore-pump and turbomolecular pump on.
2. Open V3, V21 and V12. The mixing cycle should now be open.
3. Bleed Helium into the cycle through V9 slowly. Do not exceed 3 mbar on M22, or 6 bar on M1.
4. Maintain the pressure in the cycle by adding helium through V9. Do not allow the temperature to exceed 6 K by adding too much.
5. The still temperature should eventually reach 500 mK. By activating the heater at about 35% the still should approach 750 mK. This will maximise flow.

C.5 Stopping the Cryostat

If neither the pre-cooling nor the mixing cycle have started, then turn off the compressor manually, and then stop the rotary valve in the software. If only precooling has been started, then follow the steps in section C.4 to pump it out. If a blockage due to contaminant by water or nitrogen etc. formed make sure that all the Helium is out of the system, and then close off the holding tank before starting the cleaning procedure in Section C.6. If the full mixing cycle was operating, then follow the procedure below with the assumption that the turbomolecular pump is running.

1. close V2 and V7 to keep a little Helium around the compressor. The compressor can now be turned off.
2. High pressure helium should be routed to the holding tank through V28, making sure that V6 is closed afterward. The remaining helium should be pumped into the tank through V11, V10 and V29.
3. Open V5 slowly. M22 should not go above 1 mbar. Pre-cooling may be evacuated again by opening V35.
4. After evacuation close V31, V11, and V10.
5. Making sure that all helium is secure follow the cleaning procedure in Section C.6 before moving on to the next step.
6. To turn off the 4 K and 77 K stages, first turn off the compressor manually from its front panel using the OFF button. Following this, turn off the rotary valve from the software. If you have been successful, the small white box with a red LED readout on the back of the cryostat rack will read 0.0.

C.6 Cleaning the Helium Lines

Historically I have had the most success running the cryostat after at least a day of cleaning the helium lines. For this basic cleaning all parts of the cryostat are pumped using a small turbomolecular pump through V27. When the pressure is very low the integrated turbomolecular pump can be used to extract more dirt. This should be started below 77 K so that helium is removed before other gases are liberated. The cryostat acts as an impedance, so a pressure difference of three orders of magnitude can be sustained across the internal helium lines. This should be kept in mind when using the integrated turbomolecular pump.

Appendix D

Performing Transformations

Transforming a Hamiltonian into another frame is a powerful tool for understanding quantum mechanical systems. The most trivial example of a transformation is setting the lowest energy state of a system to zero, and referencing all states from it. The transformation procedure here is general, so that operators can be used in the transformation, leading to less trivial results.

This procedure is certainly not new. It is used by many academics. I have found that amongst young researchers such as myself there is often confusion around the topic, so I have included a simple derivation in the hope that it is useful to my successors.

D.1 Derivation

A unitary transformation operator \hat{T} is a general transformation to be performed on a system to take it from the Schrödinger to an interaction picture (or between interaction pictures). For the sake of simplicity I have omitted factors of \hbar . The transformation operates on the wavefunction $|\psi\rangle$ to yield the transformed wavefunction $|\psi'\rangle$.

$$\begin{aligned} |\psi'\rangle &= \hat{T} |\psi\rangle \\ |\psi\rangle &= \hat{T}^\dagger |\psi'\rangle \end{aligned} \tag{D.1}$$

The Schrödinger equation is

$$H |\psi\rangle = i \frac{d}{dt} |\psi\rangle \tag{D.2}$$

The transformed wavefunction is then substituted into the Schrödinger equation.

$$H \hat{T}^\dagger |\psi'\rangle = i \frac{d}{dt} (\hat{T}^\dagger |\psi'\rangle) \tag{D.3}$$

The right hand side is expanded using the product rule.

$$H\hat{T}^\dagger |\psi'\rangle = i\hat{T}^\dagger \frac{d}{dt} |\psi'\rangle + i \frac{d\hat{T}^\dagger}{dt} |\psi'\rangle \quad (\text{D.4})$$

Multiplying both sides by \hat{T} gives

$$\hat{T}H\hat{T}^\dagger |\psi'\rangle = i \frac{d}{dt} |\psi'\rangle + i\hat{T} \frac{d\hat{T}^\dagger}{dt} |\psi'\rangle . \quad (\text{D.5})$$

By rearrangement this can be made to look like the Schrödinger equation

$$\left(\hat{T}H\hat{T}^\dagger - i\hat{T} \frac{d\hat{T}^\dagger}{dt} \right) |\psi'\rangle = i \frac{d}{dt} |\psi'\rangle . \quad (\text{D.6})$$

The part in brackets is the transformed Hamiltonian

$$H' = \hat{T}H\hat{T}^\dagger - i\hat{T} \frac{d\hat{T}^\dagger}{dt} . \quad (\text{D.7})$$

The solution to the Schrödinger equation for this transformed system needs to be used now to get the solution for the wavefunction in the Schrödinger picture.

$$|\psi'_t\rangle = e^{-iH't} |\psi'_0\rangle = U'_t |\psi'_0\rangle \quad (\text{D.8})$$

where U' is the time evolution operator in the chosen interaction picture. Applying the reverse transformation returns the desired wavefunction and also demonstrates the transformation of a time evolution operator.

$$|\psi_t\rangle = \hat{T}^\dagger U'_t \hat{T} |\psi_0\rangle \quad (\text{D.9})$$

A unitary operator can be constructed with an Hermitian operator by the relation $\hat{T} = \exp(i\hat{\Theta}t)$. Equation (D.7) can now be rewritten in terms of $\hat{\Theta}$

$$H' = e^{i\hat{\Theta}t} H e^{-i\hat{\Theta}t} - \hat{\Theta} . \quad (\text{D.10})$$

The subtraction of $\hat{\Theta}$ is a useful feature. It can sometimes suggest useful forms of $\hat{\Theta}$ based upon what parts of a Hamiltonian need to be removed or introduced. In the most trivial case $\hat{\Theta}$ will commute with the Hamiltonian. When this is true

$$\begin{aligned} e^{i\hat{\Theta}t} H e^{-i\hat{\Theta}t} &= H \\ H' &= H - \hat{\Theta} \end{aligned} \quad \text{iff } [H, \hat{\Theta}] = 0 \quad (\text{D.11})$$

Such a situation arises when the reference energy of a system is changed. The transformation simplifies to a subtraction or addition of an energy to every state level.

D.2 A Simple Example

In Part I I used a transformation to go between equations (1.11) and (1.12). In this section I demonstrate how this transformation was performed as an example. I started with equation (1.11)

$$H_{\text{atom-light}} = \underbrace{\frac{\hbar\omega_a}{2}\hat{\sigma}_3}_{\text{atom}} + \underbrace{\hbar\omega\left(\hat{a}^\dagger\hat{a} + \frac{1}{2}\right)}_{\text{field}} - i\hbar g\left(\hat{a} - \hat{a}^\dagger\right)\left(\hat{\sigma}^+ + \hat{\sigma}^-\right), \quad (\text{D.12})$$

and the transformation resulted in equation (1.12)

$$H_I = \underbrace{\frac{\hbar\Delta}{2}\hat{\sigma}_3}_{H_0} - i\hbar g\left(\hat{\sigma}^+\text{e}^{i\omega t} + \hat{\sigma}^-\text{e}^{-i\omega t}\right)\left(\hat{a}\text{e}^{-i\omega t} - \hat{a}^\dagger\text{e}^{i\omega t}\right). \quad (\text{D.13})$$

First I had to select a $\hat{\Theta}$ to do this transformation. The clue is that I want to get rid of the atom and field parts, and introduce a new factor in their place $\hbar\Delta\hat{\sigma}_3/2$.

$$\hat{\Theta} = \omega\left(\frac{\hat{\sigma}_3}{2} + \hat{a}^\dagger\hat{a} + \frac{1}{2}\right) \quad (\text{D.14})$$

Different parts of $\hat{\Theta}$ operate on different operators in the Hamiltonian. Firstly, $\hat{\Theta}$ commutes with the atom and light parts of the initial Hamiltonian and $\Delta = \omega_a - \omega$, so the transformation looks like

$$H_I = \frac{\hbar\Delta}{2}\hat{\sigma}_3 - i\hbar g\text{e}^{i\hat{\Theta}t}\left(\hat{a} - \hat{a}^\dagger\right)\left(\hat{\sigma}^+ + \hat{\sigma}^-\right)\text{e}^{-i\hat{\Theta}t}. \quad (\text{D.15})$$

Since $\hat{T} = \exp(i\hat{\Theta}t)$ is unitary, $\hat{T}\hat{T}^\dagger = \hat{T}^\dagger\hat{T} = \mathbb{1}$ can be inserted between the brackets, allowing operations on individual operators for simplicity, i.e.

$$H_I = \frac{\hbar\Delta}{2}\hat{\sigma}_3 - i\hbar g\text{e}^{i\hat{\Theta}t}\left(\hat{a} - \hat{a}^\dagger\right)\text{e}^{-i\hat{\Theta}t}\text{e}^{i\hat{\Theta}t}\left(\hat{\sigma}^+ + \hat{\sigma}^-\right)\text{e}^{-i\hat{\Theta}t}. \quad (\text{D.16})$$

The first operator to handle is the annihilation operator. The operator needs to be on one side of both the transformation operators. The only term in $\hat{\Theta}$ of concern is the $\hat{a}^\dagger\hat{a}$ term. The others lead to a zero in the exponential and thus identity operators which can be neglected

$$\text{e}^{i\hat{\Theta}t}\hat{a}\text{e}^{-i\hat{\Theta}t} = \exp\left(i\omega\hat{a}^\dagger\hat{a}t\right)\hat{a}\exp\left(-i\omega\hat{a}^\dagger\hat{a}t\right). \quad (\text{D.17})$$

The exponential of the number operator $\hat{a}^\dagger \hat{a}$ is composed of increasing powers of $\hat{a}^\dagger \hat{a}$. If there is an annihilation operator on the left of $\exp(-i\hbar\omega \hat{a}^\dagger \hat{a}t)$ then it can be tacked onto the front of every component in the expansion of the exponential, and an annihilation operator removed from the end so that

$$\hat{a} \exp(-i\omega \hat{a}^\dagger \hat{a}t) = \exp(-i\omega \hat{a} \hat{a}^\dagger t) \hat{a}. \quad (\text{D.18})$$

Inserting this into equation (D.17)

$$\begin{aligned} e^{i\hat{\Theta}t} \hat{a} e^{-i\hat{\Theta}t} &= \exp(i\omega \hat{a}^\dagger \hat{a}t) \exp(-i\omega \hat{a} \hat{a}^\dagger t) \hat{a} \\ &= e^{-i\omega t} \hat{a}. \end{aligned} \quad (\text{D.19})$$

Similarly, for the creation operator

$$e^{i\hat{\Theta}t} \hat{a}^\dagger e^{-i\hat{\Theta}t} = \hat{a}^\dagger e^{i\omega t}, \quad (\text{D.20})$$

which eliminates the operators in the exponential, leaving a time dependent phase. These exponential factors are simply numbers, so they can go on either side of the creation and annihilation operators. Next are the atomic raising and lowering operators. The relevant term in $\hat{\Theta}$ is now the term with $\hat{\sigma}_3$.

$$e^{i\hat{\Theta}t} \hat{\sigma}^+ e^{-i\hat{\Theta}t} = \exp\left(i\frac{\omega}{2} \hat{\sigma}_3 t\right) \hat{\sigma}^+ \exp\left(-i\frac{\omega}{2} \hat{\sigma}_3 t\right) \quad (\text{D.21})$$

Again, the exponential of $\hat{\sigma}_3$ is treated as increasing powers of $\hat{\sigma}_3 = \hat{\sigma}^+ \hat{\sigma}^- - \hat{\sigma}^- \hat{\sigma}^+$. Keeping in mind that $\hat{\sigma}^- \hat{\sigma}^- = \hat{\sigma}^+ \hat{\sigma}^+ = 0$,

$$\begin{aligned} e^{i\hat{\Theta}t} \hat{\sigma}^+ e^{-i\hat{\Theta}t} &= \exp\left(i\frac{\omega}{2} \hat{\sigma}_3 t\right) \hat{\sigma}^+ \exp\left(-i\frac{\omega}{2} \hat{\sigma}_3 t\right) \\ &= \exp\left(i\frac{\omega}{2} \hat{\sigma}^+ \hat{\sigma}^- t\right) \hat{\sigma}^+ \exp\left(-i\frac{-\omega}{2} \hat{\sigma}^- \hat{\sigma}^+ t\right) \\ &= \exp\left(i\frac{\omega}{2} t\right) \hat{\sigma}^+ \hat{\sigma}^- \hat{\sigma}^+ \hat{\sigma}^- \exp\left(i\frac{\omega}{2} t\right) \\ &= e^{i\omega t} \hat{\sigma}^+. \end{aligned} \quad (\text{D.22})$$

Similarly for the lowering operator

$$e^{i\hat{\Theta}t} \hat{\sigma}^- e^{-i\hat{\Theta}t} = e^{-i\omega t} \hat{\sigma}^-. \quad (\text{D.23})$$

Inserting these results back into equation (D.16) completes the transformation

$$H_I = \frac{\hbar\Delta}{2} \hat{\sigma}_3 - i\hbar g \left(\hat{\sigma}^+ e^{i\hbar\omega t} + \hat{\sigma}^- e^{-i\hbar\omega t} \right) \left(\hat{a} e^{-i\hbar\omega t} - \hat{a}^\dagger e^{i\hbar\omega t} \right). \quad (\text{D.24})$$

Bibliography

- [1] E. T. Jaynes and F. W. Cummings. ‘Comparison of quantum and semiclassical radiation theories with application to the beam maser’. *Proceedings of the IEEE*, 1963. **51** (1) 89.
- [2] B. W. Shore and P. L. Knight. ‘The Jaynes-Cummings Model’. *Journal of Modern Optics*, 1993. **40** (7) 1195. DOI: 10.1080/09500349314551321.
- [3] R. H. Dicke. ‘Coherence in Spontaneous Radiation Processes’. *Physical Review Online Archive (Prola)*, 1954. **93** (1) 99. DOI: 10.1103/PhysRev.93.99.
- [4] M. Tavis and F. W. Cummings. ‘Exact Solution for an N-Molecule-Radiation-Field Hamiltonian’. *Physical Review*, 1968. **170** (2) 379. DOI: 10.1103/PhysRev.170.379.
- [5] P. Meystre and M. Sargent. *Elements of Quantum Optics* (Springer-Verlag Berlin and Heidelberg GmbH & Co. K), 2nd edition, 1991. ISBN: 354054190X.
- [6] G. S. Agarwal. ‘Vacuum-field Rabi oscillations of atoms in a cavity’. *J. Opt. Soc. Am. B*, 1985. **2** (3) 480. DOI: 10.1364/JOSAB.2.000480.
- [7] E. M. Purcell. ‘Spontaneous Emission Probabilities at Radio Frequencies’. *Physical Review*, 1946. **69** 681. DOI: 10.1103/PhysRev.69.674.2.
- [8] J. H. Eberly, N. B. Narozhny, and J. J. Sanchez-Mondragon. ‘Periodic Spontaneous Collapse and Revival in a Simple Quantum Model’. *Physical Review Letters*, 1980. **44** (20) 1323. DOI: 10.1103/PhysRevLett.44.1323.
- [9] F. Casagrande, A. Lulli, and V. Santagostino. ‘Coherently driven and coherently pumped micromaser’. *Physical Review A*, 2002. **65** (2) 023809. DOI: 10.1103/PhysRevA.65.023809.
- [10] J. D. Cresser and S. M. Pickles. ‘A quantum trajectory analysis of the one-atom micromaser’. *Quantum and Semiclassical Optics: Journal of the European Optical Society Part B*, 1996. **8** (1) 73. DOI: 10.1088/1355-5111/8/1/008.
- [11] H. P. Breuer. ‘Non-Markovian generalization of the Lindblad theory of open quantum systems’. *Physical Review A*, 2007. **75** (2) 022103. DOI: 10.1103/PhysRevA.75.022103.
- [12] M. Moodley and F. Petruccione. ‘Stochastic wave-function unraveling of the generalized Lindblad master equation’. *Physical Review A*, 2009. **79** (4) 042103. DOI: 10.1103/PhysRevA.79.042103.

BIBLIOGRAPHY

- [13] B. G. Englert and G. Morigi. ‘Five Lectures On Dissipative Master Equations’, 2002. *Preprint*: arXiv:quant-ph/0206116.
- [14] P. Filipowicz, J. Javanainen, and P. Meystre. ‘Theory of a microscopic maser’. *Physical Review A*, 1986. **34** 3077. DOI: 10.1103/PhysRevA.34.3077.
- [15] M. O. Scully, H. Walther, G. S. Agarwal, T. Quang, and W. Schleich. ‘Micromaser spectrum’. *Physical Review A*, 1991. **44** (9) 5992. DOI: 10.1103/PhysRevA.44.5992.
- [16] F. Casagrande, A. Ferraro, A. Lulli, R. Bonifacio, E. Solano, and H. Walther. ‘How to Measure the Phase Diffusion Dynamics in the Micromaser’. *Physical Review Letters*, 2003. **90** (18) 183601. DOI: 10.1103/PhysRevLett.90.183601.
- [17] F. Casagrande, A. Ferraro, A. Lulli, R. Bonifacio, E. Solano, and H. Walther. ‘Micromaser spectrum and phase diffusion dynamics’. *Journal of Optics B: Quantum and Semiclassical Optics*, 2003. **5** (4) S459. DOI: 10.1088/1464-4266/5/4/351.
- [18] G. S. Agarwal, W. Lange, and H. Walther. ‘Intense-field renormalization of cavity-induced spontaneous emission’. *Physical Review A*, 1993. **48** (6) 4555. DOI: 10.1103/PhysRevA.48.4555.
- [19] B. G. Englert, M. Löffler, O. Benson, B. Varcoe, M. Weidinger, and H. Walther. ‘Entangled Atoms in Micromaser Physics’. *Fortschritte der Physik*, 1998. **46** (6-8) 897. DOI: 10.1002/(SICI)1521-3978(199811)46:6/8%3C897::AID-PROP897%3E3.0.CO;2-2.
- [20] H. Walther, B. T. H. Varcoe, S. Brattke, and M. Weidinger. ‘Preparing pure photon number states of the radiation field’. *Nature*, 2000. **403** (6771) 743. DOI: 10.1038/35001526.
- [21] S. Brattke, B. Varcoe, and H. Walther. ‘Preparing Fock states in the micromaser’. *Optics Express*, 2001. **8** (2) 131. DOI: 10.1364/OE.8.000131.
- [22] B. T. H. Varcoe, S. Brattke, and H. Walther. ‘Generation of Fock states in the micromaser’. *Journal of Optics B: Quantum and Semiclassical Optics*, 2000. **2** (2) 154. DOI: 10.1088/1464-4266/2/2/316.
- [23] S. Brattke, B. T. H. Varcoe, and H. Walther. ‘Generation of Photon Number States on Demand via Cavity Quantum Electrodynamics’. *Physical Review Letters*, 2001. **86** (16) 3534. DOI: 10.1103/PhysRevLett.86.3534.
- [24] S. Brattke, B.-G. Englert, B. T. Varcoe, and H. Walther. ‘Fock states in a cyclically pumped one-atom maser’. *Journal of Modern Optics*, 2000. **47** (14) 2857. DOI: 10.1080/09500340008232201.
- [25] H. Walther, B. T. H. Varcoe, B. G. Englert, and T. Becker. ‘Cavity quantum electrodynamics’. *Reports on Progress in Physics*, 2006. **69** (5) 1325. DOI: 10.1088/0034-4885/69/5/R02.
- [26] M. O. Scully and M. S. Zubairy. *Quantum Optics* (Cambridge University Press), first edition, 1997. ISBN: 9780521435956.

BIBLIOGRAPHY

- [27] M. S. Everitt, M. L. Jones, and B. T. H. Varcoe. ‘Dephasing of entangled atoms as an improved test of quantum gravity’, 2008. *Preprint*: arXiv:0812.3052.
- [28] M. S. Everitt and B. M. Garraway. ‘Multimode Quantum Optical Logic’. In ‘Conference on Coherence and Quantum Optics’, OSA Technical Digest (CD) (Optical Society of America), 2007 pages 456–457.
- [29] B. W. Shore. ‘Two-level behavior of coherent excitation of multilevel systems’. *Physical Review A*, 1981. **24** (3) 1413. *DOI*: 10.1103/PhysRevA.24.1413.
- [30] R. J. Cook and B. W. Shore. ‘Coherent dynamics of N-level atoms and molecules. III. An analytically soluble periodic case’. *Physical Review A*, 1979. **20** (2) 539. *DOI*: 10.1103/PhysRevA.20.539.
- [31] M. A. Nielsen and I. L. Chuang. *Quantum Computation and Quantum Information* (Cambridge University Press), 2000. *ISBN*: 9780521635035.
- [32] N. D. Mermin. ‘Extreme quantum entanglement in a superposition of macroscopically distinct states’. *Physical Review Letters*, 1990. **65** (15) 1838. *DOI*: 10.1103/PhysRevLett.65.1838.
- [33] R. Raussendorf and H. J. Briegel. ‘A One-Way Quantum Computer’. *Physical Review Letters*, 2001. **86** (22) 5188. *DOI*: 10.1103/PhysRevLett.86.5188.
- [34] M. Nielsen. ‘Cluster-state quantum computation’. *Reports on Mathematical Physics*, 2006. **57** (1) 147. *DOI*: 10.1016/S0034-4877(06)80014-5.
- [35] S.-B. Zheng and G.-C. Guo. ‘Efficient Scheme for Two-Atom Entanglement and Quantum Information Processing in Cavity QED’. *Physical Review Letters*, 2000. **85** (11) 2392. *DOI*: 10.1103/PhysRevLett.85.2392.
- [36] S. Osnaghi, P. Bertet, A. Auffeves, P. Maioli, M. Brune, J. M. Raimond, and S. Haroche. ‘Coherent Control of an Atomic Collision in a Cavity’. *Physical Review Letters*, 2001. **87** (3) 037902. *DOI*: 10.1103/PhysRevLett.87.037902.
- [37] D. Bouwmeester, J.-W. Pan, M. Daniell, H. Weinfurter, and A. Zeilinger. ‘Observation of Three-Photon Greenberger-Horne-Zeilinger Entanglement’. *Physical Review Letters*, 1999. **82** (7) 1345. *DOI*: 10.1103/PhysRevLett.82.1345.
- [38] A. Einstein, B. Podolsky, and N. Rosen. ‘Can Quantum-Mechanical Description of Physical Reality Be Considered Complete?’ *Physical Review*, 1935. **47** 777. *DOI*: 10.1103/PhysRev.47.777.
- [39] M. Hein, J. Eisert, and H. J. Briegel. ‘Multiparty entanglement in graph states’. *Physical Review A*, 2004. **69** (6) 062311. *DOI*: 10.1103/PhysRevA.69.062311.
- [40] S. Benjamin. ‘Quantum looms: entangling continuous particle streams’, 2008. Unpublished.
- [41] P. J. Blythe and B. T. H. Varcoe. ‘A cavity-QED scheme for cluster-state quantum computing using crossed atomic beams’. *New Journal of Physics*, 2006. **8** (10) 231. *DOI*: 10.1088/1367-2630/8/10/231.

BIBLIOGRAPHY

- [42] A. M. Stephens, Z. W. E. Evans, S. J. Devitt, A. D. Greentree, A. G. Fowler, W. J. Munro, J. L. O'Brien, K. Nemoto, and L. C. L. Hollenberg. ‘Deterministic optical quantum computer using photonic modules’. *Physical Review A*, 2008. **78** (3) 032318. DOI: 10.1103/PhysRevA.78.032318.
- [43] I. I. Ryabtsev, D. B. Tretyakov, and I. I. Beterov. ‘Stark-switching technique for fast quantum gates in Rydberg atoms’. *Journal of Physics B: Atomic, Molecular and Optical Physics*, 2003. **36** (2) 297. DOI: 10.1088/0953-4075/36/2/310.
- [44] A. Peters, K. Y. Chung, B. Young, J. Hensley, and S. Chu. ‘Precision atom interferometry’. *Philosophical Transactions of the Royal Society of London. Series A: Mathematical, Physical and Engineering Sciences*, 1997. **355** (1733) 2223. DOI: 10.1098/rsta.1997.0121.
- [45] R. Bingham. ‘The Search for Quantum Gravity Using Matter Interferometers’. *Physica Scripta*, 2005. **T116** 132. DOI: 10.1238/Physica.Topical.116a00132.
- [46] M. Arndt and K. Hornberger. ‘Quantum interferometry with complex molecules’, 2009. Preprint: arXiv:0903.1614.
- [47] V. Vedral. ‘Quantifying entanglement in macroscopic systems’. *Nature*, 2008. **453** (7198) 1004. DOI: 10.1038/nature07124.
- [48] S. S. Jang, Y. W. Cheong, J. Kim, and H.-W. Lee. ‘Robustness of multiparty nonlocality to local decoherence’. *Physical Review A*, 2006. **74** (6) 062112. DOI: 10.1103/PhysRevA.74.062112.
- [49] H. Lee, P. Kok, and J. Dowling. ‘A quantum Rosetta stone for interferometry’. *Journal of Modern Optics*, 2002. **49** (14) 2325. DOI: 10.1080/0950034021000011536.
- [50] A. Einstein. ‘Über die von der molekularkinetischen Theorie der Wärme geforderte Bewegung von in ruhenden Flüssigkeiten suspendierten Teilchen’. *Annalen der Physik*, 1905. **322** (8) 549. DOI: 10.1002/andp.19053220806.
- [51] J. J. Cooper, D. W. Hallwood, and J. A. Dunningham. ‘Scheme for implementing atomic multiport devices’. *Journal of Physics B: Atomic, Molecular and Optical Physics*, 2009. **42** (10) 105301. DOI: 10.1088/0953-4075/42/10/105301.
- [52] R. P. Feynman, F. B. Morinigo, W. G. Wagner, and D. Pines. *Feynman Lectures on Gravitation* (Westview Press), 2002. ISBN: 9780813340388.
- [53] W. L. Power and I. C. Percival. ‘Decoherence of quantum wave packets due to interaction with conformal space-time fluctuations’. *Proceedings of the Royal Society of London. Series A: Mathematical, Physical and Engineering Sciences*, 2000. **456** (1996) 955. DOI: 10.1098/rspa.2000.0544.
- [54] C. H. Wang. ‘Conformal geometrodynamics: True degrees of freedom in a truly canonical structure’. *Physical Review D*, 2005. **71** (12) 124026. DOI: 10.1103/PhysRevD.71.124026.
- [55] C. H. Wang, R. Bingham, and T. J. Mendonca. ‘Quantum gravitational decoherence of matter waves’. *Classical and Quantum Gravity*, 2006. **23** (18) L59. DOI: 10.1088/0264-9381/23/18/L01.

BIBLIOGRAPHY

- [56] C. H. T. Wang, P. M. Bonifacio, R. Bingham, and T. J. Mendonca. ‘Nonlinear random gravity. I. Stochastic gravitational waves and spontaneous conformal fluctuations due to the quantum vacuum’, 2008. *Preprint*: arXiv:0806.3042.
- [57] D. M. Greenberger, M. A. Horne, and A. Zeilinger. ‘Going Beyond Bell’s Theorem’, 2007. *Preprint*: arXiv:0712.0921.
- [58] D. Meschede, H. Walther, and G. Müller. ‘One-Atom Maser’. *Physical Review Letters*, 1985. **54** (6) 551. *DOI*: 10.1103/PhysRevLett.54.551.
- [59] T. F. Gallagher. ‘Rydberg atoms’. *Reports on Progress in Physics*, 1988. **51** (2) 143. *DOI*: 10.1088/0034-4885/51/2/001.
- [60] R. G. Hulet and D. Kleppner. ‘Rydberg Atoms in “Circular” States’. *Physical Review Letters*, 1983. **51** (16) 1430. *DOI*: 10.1103/PhysRevLett.51.1430.
- [61] P. Nussenzveig, F. Bernardot, M. Brune, J. Hare, J. M. Raimond, S. Haroche, and W. Gawlik. ‘Preparation of high-principal-quantum-number “circular” states of rubidium’. *Physical Review A*, 1993. **48** (5) 3991. *DOI*: 10.1103/PhysRevA.48.3991.
- [62] B. Sanguinetti, H. O. Majeed, M. L. Jones, and B. T. H. Varcoe. ‘Precision measurements of quantum defects in the $nP_{3/2}$ Rydberg states of ^{85}Rb ’. *Journal of Physics B: Atomic, Molecular and Optical Physics*, 2009. **42** (16) 165004. *DOI*: 10.1088/0953-4075/42/16/165004.
- [63] B. Sanguinetti. *Building a Modern Micromaser: Atoms and Cavities*. Ph.D. thesis, University of Leeds, School of Physics and Astronomy, 2009.
- [64] M. R. Walkiewicz, P. J. Fox, and R. E. Scholten. ‘Candlestick rubidium beam source’. *Review of Scientific Instruments*, 2000. **71** (9) 3342. *DOI*: 10.1063/1.1288261.
- [65] B. Sanguinetti and B. T. H. Varcoe. ‘Use of a piezoelectric SQUIGGLE(R) motor for positioning at 6 K in a cryostat’. *Cryogenics*, 2006. **46** (9) 694. *DOI*: 10.1016/j.cryogenics.2006.02.007.
- [66] G. Goubau. ‘Surface Waves and Their Application to Transmission Lines’. *Journal of Applied Physics*, 1950. **21** (11) 1119. *DOI*: 10.1063/1.1699553.
- [67] G. J. E. Goubau. ‘Surface Wave Transmission Line’. U.S. Patent number 2685068, 1954.
- [68] G. J. E. Goubau. ‘Launching and Receiving of Surface Waves’. U.S. Patent number 2921277, 1960.
- [69] A. Farjadpour, D. Roundy, A. Rodriguez, M. Ibanescu, P. Bermel, J. D. Joannopoulos, S. G. Johnson, and G. W. Burr. ‘Improving accuracy by subpixel smoothing in the finite-difference time domain’. *Opt. Lett.*, 2006. **31** (20) 2972. *DOI*: 10.1364/OL.31.002972.
- [70] N. Klein, G. Muller, H. Piel, and J. Schurr. ‘Superconducting microwave resonators for physics experiments’. *IEEE Transactions on Magnetics*, 1989. **25** (2) 1362. *DOI*: 10.1109/20.92548.

BIBLIOGRAPHY

- [71] T. Weiland, M. Krasilnikov, R. Schuhmann, A. Skarlatos, M. Wilke, J. Le Duff, H. Henke, W. Wuensch, R. Carter, P. Baudrenghien, R. Cooper, A. Schnase, A. Gamp, R. Garoby, A. Schempp, G. Bisoffi, W. Pirkl, U. Ratzinger, E. Pedroni, F. Nolden, F. Caspers, G. Hutter, H. Gräf, and A. Richter. *CAS - CERN Accelerator School: Radio Frequency Engineering*. CERN Accelerator School (CERN), 2000. ISBN: 9789290832492.
- [72] R. N. Clarke and C. B. Rosenberg. ‘Fabry-Perot and open resonators at microwave and millimetre wave frequencies, 2-300 GHz’. *Journal of Physics E: Scientific Instruments*, 1982. **15** (1) 9. DOI: 10.1088/0022-3735/15/1/002.
- [73] M. N. Wilson. *Superconducting Magnets (Monographs on Cryogenics, 2)* (Oxford University Press, USA), 1987. ISBN: 9780198548102.
- [74] G. Berden, R. Peeters, and G. Meijer. ‘Cavity ring-down spectroscopy: Experimental schemes and applications’. *International Reviews in Physical Chemistry*, 2000. **19** (4) 565. DOI: 10.1080/014423500750040627.
- [75] M. L. Jones. *Construction of a new micromaser system*. Ph.D. thesis, University of Sussex, Department of Physics and Astronomy, 2008.
- [76] E. Knill, R. Laflamme, and G. J. Milburn. ‘A scheme for efficient quantum computation with linear optics’. *Nature*, 2001. **409** (6816) 46. DOI: 10.1038/35051009.
- [77] W. Dür, G. Vidal, and J. I. Cirac. ‘Three qubits can be entangled in two inequivalent ways’. *Physical Review A*, 2000. **62** (6) 062314. DOI: 10.1103/PhysRevA.62.062314.
- [78] E. Schrödinger. ‘Are there quantum jumps? Part II’. *The British Journal for the Philosophy of Science*, 1952. **III** (11) 233. DOI: 10.1093/bjps/III.11.233.
- [79] T. M. Roach and D. Henclewood. ‘Novel rubidium atomic beam with an alkali dispenser source’. *Journal of Vacuum Science & Technology A: Vacuum, Surfaces, and Films*, 2004. **22** (6) 2384. DOI: 10.1116/1.1806440.
- [80] W. A. Stein. *Sage Mathematics Software (Version 4.1.1)*. The Sage Development Team, 2009.
- [81] S. Kuhr, W. Alt, D. Schrader, M. Muller, V. Gomer, and D. Meschede. ‘Deterministic Delivery of a Single Atom’. *Science*, 2001. **293** (5528) 278. DOI: 10.1126/science.1062725.
- [82] A. Wallraff, D. I. Schuster, A. Blais, L. Frunzio, R.-S. Huang, J. Majer, S. Kumar, S. M. Girvin, and R. J. Schoelkopf. ‘Strong coupling of a single photon to a superconducting qubit using circuit quantum electrodynamics’. *Nature*, 2004. **431** (7005) 162. DOI: 10.1038/nature02851.
- [83] A. Blais, R.-S. Huang, A. Wallraff, S. M. Girvin, and R. J. Schoelkopf. ‘Cavity quantum electrodynamics for superconducting electrical circuits: An architecture for quantum computation’. *Physical Review A*, 2004. **69** (6) 062320. DOI: 10.1103/PhysRevA.69.062320.
- [84] M. Harvey and A. J. Murray. ‘Cold Atom Trap with Zero Residual Magnetic Field: The ac Magneto-Optical Trap’. *Physical Review Letters*, 2008. **101** (17). DOI: 10.1103/PhysRevLett.101.173201.
- [85] ‘Astrolab Astro-Cobra-Flex’. Internet Address: <http://www.astrolab.com/>.